Wave groups and small scale variability of wave heights observed by altimeters

Marine De Carlo[1], Fabrice Ardhuin[2], Annabelle Ollivier[3], and Adrien Nigou[3]

[1]Univ. Brest, CNRS, Ifremer, IRD, Laboratoire d'Océanographie Physique et Spatiale (LOPS), IUEM
[2]Univ. Brest, CNRS, Ifremer, IRD
[3]Collecte Localisation Satellite (CLS)

February 27, 2023

Abstract

Recent satellite altimeter retracking and filtering methods have considerably reduced the noise level in estimates of the significant wave height (Hs), allowing to study processes with smaller spatial scales. In particular, previous studies have shown that wave-current interactions may explain most of the variability of Hs at scales 20 to 100 km. As the spatial scale of the measurement is reduced, random fluctuations emerge that should be associated to wave groups. Here we quantify the magnitude of this effect, and the contribution of wave groups to the uncertainty in Hs measurements by altimeters, with a particular focus on extreme extra-tropical storms. We take advantage of the low orbit altitude of the China-France Ocean Satellite (CFOSAT), and the low noise level of the nadir beam of the SWIM instrument. Our estimate of wave group effects uses directional wave spectra measured by off-nadir beams on SWIM and signal processing theory that gives statistical properties of the wave envelope, and thus the local wave heights, from the shape of the wave spectrum. We find that the standard deviation of Hs associated to wave groups is a function of satellite altitude, wave height and spectral bandwidth. For CFOSAT these fluctuations generally account for about 25% of the variance measured over a 80 km distance. This fraction is largest in storms and in the presence of long swells. When the estimated effect of wave groups is subtracted from the measured Hs variance, the remaining variability is higher in regions of strong currents.

Wave groups and small scale variability of wave heights observed by altimeters

Marine De Carlo[1], Fabrice Ardhuin[1], Annabelle Ollivier[2], Adrien Nigou[2]

[1]Univ Brest, CNRS, Ifremer, IRD, Laboratoire d'Océanographie Physique et Spatiale (LOPS), IUEM, F29280, Plouzané, France.

[2]Collecte Localisation Satellite (CLS), Ramonville Saint-Agne, France

Key Points:

- Wave groups contribute to small-scale fluctuations in altimeter wave heights, explaining 25% of the variance measured by CFOSAT in 80 km.
- For the same wave height, fluctuations are larger in the presence of long and narrow-banded waves, typical of swell-dominated conditions.
- Altimeters smooth out scales shorter than the square root of half the H_s times the altitude, and distort spatial patterns at that scale.

Corresponding author: Marine De Carlo, mdecarlo@ifremer.fr

Abstract

Recent satellite altimeter retracking and filtering methods have considerably reduced the noise level in estimates of the significant wave height (H_s), allowing to study processes with smaller spatial scales. In particular, previous studies have shown that wave-current interactions may explain most of the variability of H_s at scales 20 to 100 km. As the spatial scale of the measurement is reduced, random fluctuations emerge that should be associated to wave groups. Here we quantify the magnitude of this effect, and the contribution of wave groups to the uncertainty in H_s measurements by altimeters, with a particular focus on extreme extra-tropical storms. We take advantage of the low orbit altitude of the China-France Ocean Satellite (CFOSAT), and the low noise level of the nadir beam of the SWIM instrument. Our estimate of wave group effects uses directional wave spectra measured by off-nadir beams on SWIM and signal processing theory that gives statistical properties of the wave envelope, and thus the local wave heights, from the shape of the wave spectrum. We find that the standard deviation of H_s associated to wave groups is a function of satellite altitude, wave height and spectral bandwidth. For CFOSAT these fluctuations generally account for about 25% of the variance measured over a 80 km distance. This fraction is largest in storms and in the presence of long swells. When the estimated effect of wave groups is subtracted from the measured H_s variance, the remaining variability is higher in regions of strong currents.

Plain Language Summary

Satellite altimeters routinely provide measurements of the height of ocean waves, and improved instruments or processing techniques have led to more precise and detailed measurements. Here we use a combination of simulations and data from the China France Ocean satellite (CFOSAT) to interpret the small scale fluctuations in wave height measurements as the effect of wave "groups" which are fluctuations of the heights of consecutive waves associated to random waves. Due to spatial averaging within the radar footprint, we find that the fluctuations of significant wave heights (H_s) associated to wave group are a function of satellite altitude, wave height and other properties of the ocean waves. For CFOSAT, wave groups give a standard deviation of H_s that is of the order of 3 to 5% of H_s, typically half of the measured standard deviation of H_s.

1 Introduction

Wind-waves impact all activities at sea, air-sea interactions and remote sensing, and there is a general need for obtaining more accurate and higher resolution information about the sea state. Today, satellite radar altimetry is the most extensive source of measurements with a global coverage, providing routine estimates of the significant wave height H_s (Ardhuin et al., 2019). As these data are getting used for a wide range of applications, it is important to understand what can be measured with altimeters, at what scale and with what uncertainty.

The scale of the measurement was particularly discussed by Chelton et al. (1989), who introduced the concept of *oceanographic footprint* which contains the sea surface points that contribute to the measurement of sea level and wave height. This footprint is a disc of radius

$$r_C = \sqrt{\frac{2hH_s + 2\delta_R}{1 + h/R_E}} \tag{1}$$

where h is the satellite altitude, R_E is the Earth radius, H_s is the wave height and the range resolution $\delta_R = c/(2B)$ is defined by the radar bandwidth B and the speed of light c. We note that all Ku-band altimeters have used $B = 320$ MHz giving $\delta_R = 0.47$ m, and $B = 500$ MHz on SARAL-AltiKa gives $\delta_R = 0.32$ m, so that r_C is always larger than 1 km. Because low Earth orbit satellites fly over the ocean at a speed around 7 km/s, averaging altimeter data over 0.05 s corresponds to a spatial average over 350 m and thus does not change much the effective footprint of the measurement.

The apparent noise in such data is generally attributed to the uncertainty of the measurement, and has led users of altimetry data to take longer averages of H_s, typically 1 to 10 s, corresponding to a distance that spans 7 to 70 km. While it effectively reduces noise, such averaging also blurs potentially interesting features, in particular the peaks of storms, coastal gradients (Passaro et al., 2021), and the signature of surface currents (Quilfen & Chapron, 2019). Away from surface current gradients and coastlines, sea states are uniform over scales of the order of 70 km (Tournadre, 1993). Still, within these scales, the random nature of the wave field is another source of expected geophysical variability. Theoretical analysis, in situ time series and airborne remote sensing show that small scale variations in H_s contain a signature of wave groups that can be estimated from the wave spectrum (Arhan & Ezraty, 1978; Tayfun & Lo, 1989), and is the result of the linear superposition of many independent wave trains coming from different di-

rections. Wave groups have typical time scales of a few tens of seconds to a few minutes, that translate to spatial patterns at scales of a few kilometers, hence around the possible resolution limit of altimeters, of the order of r_C. At larger scales, non-linear wave-wave interactions should contribute to fluctuations at scales 10 to 20 minutes, with spatial scales around 10 km, that should be important for wave growth (Lavrenov, 2001) and may contain information on the wave period (Badulin, 2014). Co-location of altimeter, buoy and model data with wave heights from 1 to 8 m, has been used to estimate a typical uncertainty of 1 s averaged altimeter data around 7% for $H_s > 2$ m (Dodet et al., 2022). Understanding what makes up this uncertainty will help extrapolate uncertainties to higher values of H_s, providing a better understanding of the climatology of sea state extremes.

In the present paper we focus our analysis on the fluctuations of H_s associated to wave groups and its contribution to Delay-only altimeters that provide the existing reference time series for wave climate analysis (Young et al., 2011; Dodet et al., 2020). The main question that we wish to answer is: how much wave groups contribute to the variability in H_s measurements? For this we take advantage of the unique opportunity provided by the SWIM instrument onboard the China-France Ocean Satellite (CFOSAT). SWIM provides both directional wave spectra from which we compute the spectrum of the wave envelope that contains wave groups, and along-track nadir altimetry. Our analysis uses SWIM data over the globe for two full years 2020 and 2021.

We start with two illustrative and contrasting examples in section 2, before providing results for the globe in section 3. Discussions and conclusion follow in section 4. A side question that we had to address is: how does an altimeter measure H_s over a realistic surface that contains local perturbations associated with wave groups? For this we used a very simplified simulated altimeter with numerical results shown in section 2 and an analytical derivation in Appendix A. Those results suggest that altimeters report a particular kind of average H_s over an radius that is close to $r_C/2$. When using a least-square fit to radar waveforms, estimated H_s give a spurious amplification of true H_s perturbations located at a distance around $r_C/4$ from nadir, and are blind to perturbations located right at the nadir.

2 One particular storm and a theory of wave groups

As described in Hauser et al. (2017, 2021), the instrument SWIM is a Ku-band wave scatterometer that illuminates successively 6 incidence angles (0°,2°,4°,6°,8° and 10°). The nadir beam (0°) works as all previous Poseidon radar altimeters and provides an estimate of H_s every 0.22 s, using an average over 0.055 s. As a result, the nadir beam data is expected to be similar to data from previous Ku-band altimeters, such as Poseidon-3B on Jason-3, with the specific difference given by a lower data rate (5 Hz instead of 20 Hz for the native estimates of H_s) and a different measurement geometry associated to a rather low orbit. In principle, the low orbit altitude $h = 519$ km of CFOSAT make it possible to resolve smaller scale variations of H_s as r_C is reduced by a factor 1.4 compared to the Jason satellites that orbit at 1340 km altitude. The low noise level of the satellite and specific processing of the SWIM instrument also contribute to its capability to resolve smaller scales (Tourain et al., 2021).

The off-nadir beams use the concept of the wave spectrometer (Jackson et al., 1985) based on a real-aperture radar and the normalized radar cross-section (NRCS) sensitivity to local surface slope at near-nadir incidences, providing estimates of the directional wave spectra (with a 180° ambiguity in direction). The CNES mission center (or CFOSAT Wind and Waves Intrument Center - CWWIC) provides Level 2 products both for the nadir beam and the off-nadir beams 6° to 10°. The off-nadir L2-CWWIC products consist of 2D wave spectra provided in 12 directions from 0 to 180° and in 32 wavenumbers which are constructed from overlapping of antenna scans over 180° (on each side of the track) over boxes of about 70 km by 90 km. In order to allow comparison, the nadir product is resampled by averaging values of Hs over the box size, its variation at this scale is quantified by taking its standard deviation over the same distance, std(H_s). We will particularly investigate this quantity in the present paper. In practice we also used the homogeneously reprocessed L2P product provided by the Copernicus Marine Environment Monitoring System (CMEMS), in particular we used the quality flags specific to that product.

The Ifremer Waves and Wind Operational Center (IWWOC) is in charge of developing and testing different processing and provides an alternative Level 2 products for off-nadir beams. These products are referred to as L2S products and consist of 1D wave modulation spectra, one for each measurement azimuth. Whereas the L2-CWWIC prod-

uct uses the nadir H_s to rescale the spectrum, the L2S product is based on a theoretical modulation transfer function to transform the NRCS spectra into surface elevation spectra (Jackson et al., 1985). Also the L2-CWWIC product uses a very conservative maximum wavelength of 500 m in order to avoid amplifying noise, where the L2S product does not use such a fixed value for the maximum wavelength. As a result, L2S spectra may capture the very long waves produced in the most severe storms. In our work we have recombined the L2S product in the same "boxes" as the L2 product and rescaled the energy in the resulting spectrum to correspond to the average wave height in that box. This rescaling is particularly motivated by our investigation of wave properties along the nadir track, and it corrects a bias of the order or 14% for the total energy of the spectrum. Alternative data processings are discussed in section 4.

2.1 Wave height variability in Storm Dennis

On February 14^{th} 2020, the European windstorm Dennis, which became one of the most intense extratropical cyclones ever recorded, underwent through its explosive intensification in the middle of the North Atlantic. Around 9:10 UTC that same day, Dennis was sampled by CFOSAT, with altimeter recorded H_s values up to 19.7 m for the native (5 Hz) sampling, and 17.9 m for the 1 Hz sampling (averaging over 1 second). Fig. 1.a shows a model snapshot of H_s in the north Atlantic and the corresponding descending track of CFOSAT, while Fig. 1.b shows the altimeter wave height H_s values for the three different samplings : native (4.5 Hz), 1 Hz and box averaged.

On the periphery of the storm, where the average H_s is around 10 m, we were struck by the factor two difference in std(Hs). Because this difference is not localized but spans more than 420 km (1 minute of data), we hypothesize that the spatial variability in winds and currents forcing, that are known to cause variability in H_s (Abdalla & Cavaleri, 2002; Ardhuin et al., 2017) may not play a dominant role in this difference. In particular, regions of high current variability are usually much more localized (Quilfen & Chapron, 2019). Our working hypothesis is that this variability of H_s may be dominated by fluctuations in wave heights associated to wave groups. These fluctuations have different magnitudes and spatial scales which can be estimated from the directional wave spectrum. Hence CFOSAT is a unique instrument for studying this effect as we have both H_s variability along the satellite track and directional wave spectra. In the following, we illustrate the expected signature of wave groups for the two sea state conditions that cor-

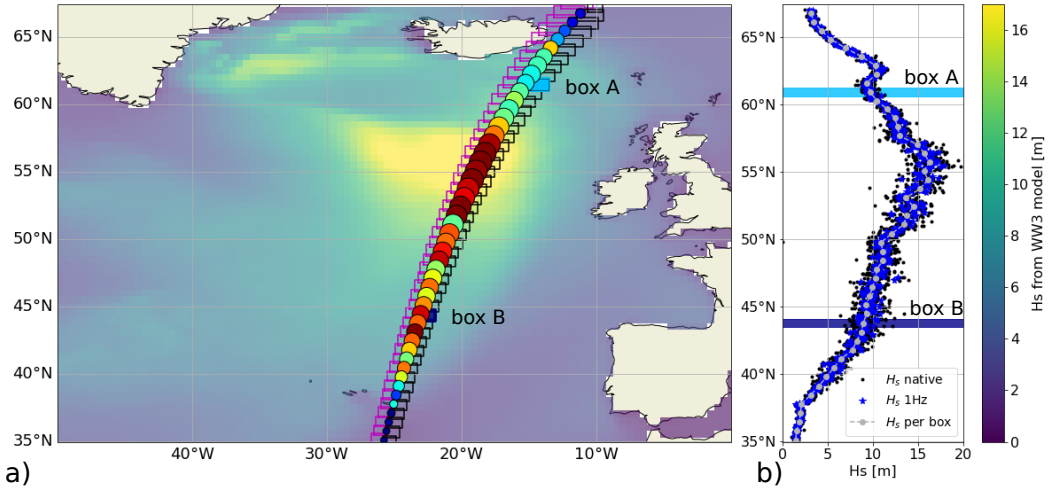

Figure 1. a) Map of wave heights in the North Atlantic at 09:00 on 14 February 2020, as provided by the model hindcast of (Alday et al., 2021), overlaid with circles located at the center of SWIM box estimates for the L2-CWWIC wave spectra. Circles are sized by the L2-CWWIC H_s estimate and color corresponds to std(Hs); b) corresponding measured H_s values as a function of latitude (y-axis) : black small dots represent native measurements at 4.5 Hz, blue stars represent the 1 Hz averaged and grey circles represent the H_s averaged over a box. Two boxes are selected for the case study: box A - highlighted in light blue - is at 62°N, and box B - in dark blue - is at 44°N.

respond to the particular SWIM boxes highlighted in light and dark blue. It is worth noting that in these two examples, the H_s values obtained from the sum of the L2S spectrum prior rescaling are around 7.5 m, which is lower than the 9 m given by the nadir beam and used in the L2 product and in this study to rescale the spectrum energy.

2.2 Variability of H_s and envelope spectrum

The patterns of individual waves vary with the shape of the wave spectrum, as illustrated in Fig. 2. A key difference between the north-side (left column) and south-side (right column) of storm Dennis is that the south-side has a longer peak wavelength around 600 m, and a more narrow spectrum, in particular in directions. The smaller width in directions gives longer wave crests while the smaller width in wavenumber magnitude gives a larger number of waves in the succession of large waves, known as groups.

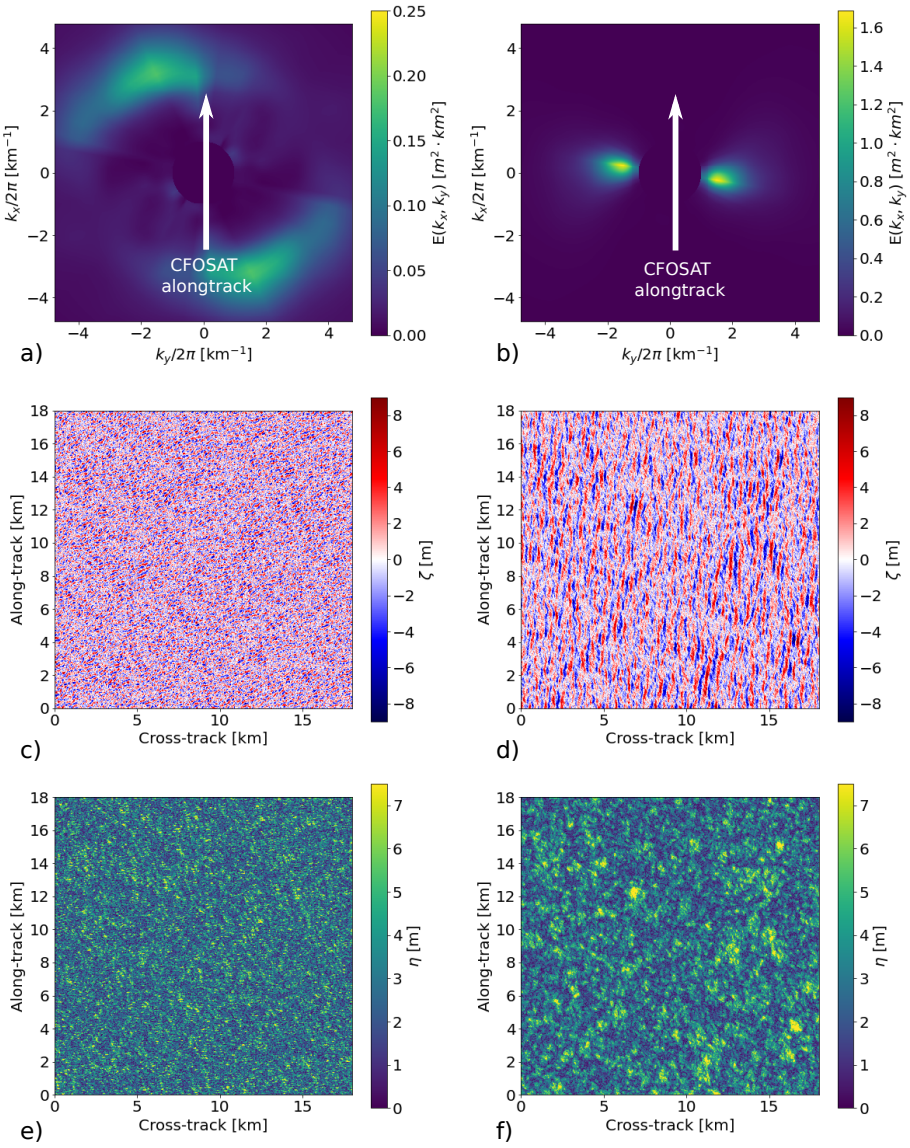

Figure 2. Left column corresponds to our chosen northern CFOSAT box, and right column to the southern box. Top line: L2S wave spectra $E(k, \theta)$ as provided by IWWOC with k the wavenumber. Middle line: simulated surface elevation maps generated from the wave spectra using random phases, bottom line: envelope of the surface elevation.

Using the envelope of the sea surface we can quantify the size of these groups (Arhan & Ezraty, 1978; Longuet-Higgins, 1984; Masson & Chandler, 1993), and their contribution to the spatial variability of H_s at all scales.

Let ζ_a be the complex surface such that $\zeta = \mathrm{Re}(\zeta_a)$ is the free surface. The envelope η of the signal is defined by $\eta = |\zeta_a|$. This defines a local amplitude of the sig-

nal, that does not contain the small scale crest-to-trough (positive to negative) variations of the original surface. Variations of the envelope contain scales much larger than the wavelengths, including scales that are comparable to, or larger than the footprint of a satellite altimeter. Hence wave groups may contribute to the fluctuations of H_s recorded by the nadir beam of SWIM, as indicated on Fig. 1.b. We will now attempt to quantify that contribution.

We thus define a local H_s as 4 times the standard deviation of the sea surface over a distance r_a. Using the Gaussian approximation of the distribution of sea surface elevations leads to an envelope following a Rayleigh distribution of parameter $H_s/4$, thus the mean of the envelope is $H_s\sqrt{\pi}/(4\sqrt{2})$. By extension,$4\sqrt{2/\pi}$ times an average of the envelope over the spatial scale r_a is equal to our local H_s.

Therefore we can write,

$$H_{s,r_a}(x,y) = 4\sqrt{\frac{2}{\pi}}(\eta \otimes g_{r_a})(x,y) \tag{2}$$

where $\otimes$ is the convolution operator and g_{r_a} is a filtering kernel of radius r_a.

In order to understand how much wave groups may contribute to H_s fluctuations in satellite data, we have to address two questions: First, what are the scales affected by wave groups? and second, what are the scales of the H_s variation that are resolved by satellite altimeters?

One simple way to quantify the different scales present in the envelope is to compute its spectrum. The most simple theoretical result comes directly from the theory of Fourier transforms that gives the spectrum of a product of functions as the convolution of the Fourier transforms. In our case, the envelope squared is the product of the elevation by its complex conjugate, and this is true for spectra in one or two dimensions. For waves in one dimension with wavenumber k, the spectrum of the envelope squared $\Psi_2(k)$ is the convolution of the spectrum of the one-sided surface elevation spectrum $E(k)$ by itself,

$$\Psi_2(k) = 8\int_0^\infty E(u)E(u+k)\mathrm{d}u, \tag{3}$$

and we note that $\Psi_2(k)$ is also single-sided.

In practice people have rather studied the variations of H_s and not that of H_s^2. Although the details of the theory are more complex, the important result is that, for low frequencies, the spectrum of the envelope $\Psi(k)$ has the same shape as the spectrum of

the envelope squared $\Psi_2(k)$ (Rice, 1944). More specifically, Tayfun and Lo (1989) have showed that a good approximation for the spectrum of the envelope is given by

$$\Psi(k) = \frac{8-2\pi}{H_s^2}\Psi_2(k) \tag{4}$$

This same result is valid for spectra in two dimensions. We now consider the double-sided wave spectrum $E(k_x, k_y)$, defined for (k_x, k_y) in the entire wavenumber plane and centrally symmetric, the region of the envelope spectrum for $k \ll k_p$ is identical to

$$\Psi_2(k_x, k_y) = 8\int_{-\infty}^{\infty}\int_{-\infty}^{\infty} E(u,v)E(u+k_x, v+k_y)\mathrm{d}u\mathrm{d}v, \tag{5}$$

in which Ψ_2 is also double-sided.

From eq. (2), the spectrum of $H_s^{r_a}$ is

$$\Psi_{H_s,r_a}(k_x, k_y) = 4\sqrt{\frac{2}{\pi}}\cdot\frac{8-2\pi}{H_s^2}\cdot\Psi_2(k_x,k_y)G_{r_a}(k_x,k_y)$$

with G_{r_a} the square of the Fourier transform of the altimeter filtering kernel g_{r_a}.

We can thus estimate the standard deviation of H_{s,r_a} in altimeter measurements along the satellite track for segment of length L_1, by integrating the expected variance for $k_x > k_1$, with $k_1 = 2\pi/L_1$ and the x-axis taken in the along-track direction.

The group-induced variation of H_s is thus equal to

$$\mathrm{var}(H_{s,r_a}, L_1)_{\mathrm{wg}} = 16\sqrt{\frac{2}{\pi}}\frac{4-\pi}{H_s^2}\int_{-\infty}^{\infty}\int_{k_1}^{\infty}\Psi_2(k_x,k_y)\cdot G_{r_a}(k_x,k_y)\mathrm{d}k_x\mathrm{d}k_y. \tag{6}$$

We now need to estimate r_a and G_{r_a} for the comparison with altimeter data.

2.3 Altimeter measurements over varying wave heights

Satellite altimeters transmit radar pulses that are reflected from the sea surface, and they measure the backscattered power as a function of time. This variation of received power as a function of time is known as the waveform, and it is typically averaged over a few hundred pulses spanning about 0.05 s in order to reduce the speckle noise (Quartly et al., 2001). Time can be transformed to distance from the satellite, or range R, and the waveform effectively contains information on the statistical distribution of ranges around the mean satellite altitude h. As shown by Brown (1977), assuming a uniform ocean reflectivity the waveform is a area-weighted histogram of the ranges. Over a flat sea surface, this histogram is a Heaviside function because the part of the ocean

surface with ranges between R and $R+\delta_R$ is an annulus of radius $r = \sqrt{R^2 - h^2}$ centered on the nadir point, with an area $2\pi R\delta_R$ that is almost constant as long as $R \approx h$. In the presence of waves, a negative surface elevation $z = \zeta$ will shift the range to a higher value, sharing the range position of sea surface elements located at $z = 0$ and further away from nadir. Given the very small incidence angles, the change in range is $\Delta_R = -\zeta$. For a Gaussian distribution of ζ with standard deviation $\sigma_H = H_s/4$, the presence of waves gives a smoothing of the histogram. Here we use the most simple theoretical shape of the waveforms that is obtained in the limit of a very broad radar antenna pattern (Brown, 1977),

$$w_B(R, \sigma_H) = \frac{1}{2}\left[1 + \mathrm{erf}\left(\frac{R-h}{\sqrt{2}\sigma_H}\right)\right]. \tag{7}$$

When "retracking" altimeter data, eq. (7) is inverted, and H_s is estimated to be 4 times the σ_H of the theoretical waveform that best fits the data. In practice the theoretical waveform also includes effects of the antenna patterns, possible mispointing, and different fitting methods have been developed to reduce the effect of noise or spurious echoes in the measured waveform (Rodriguez, 1988; Passaro et al., 2014; Tourain et al., 2021). Another important assumption needed to obtain the Brown waveform is that the sea state is homogeneous within the footprint. We thus have to discuss what sets the scale of the footprint, or more precisely where are the points on the sea surface that give the distinctive shape of the waveform and allow the fit to distinguish different wave heights.

Compared to a flat sea surface, the elevation ζ at a distance r from the nadir point will change the range R of the surface point and make it look as if it was located at a different distance $r+\delta_r$, so that points from different locations on the sea surface will map to the same range R. This is the same "range bunching" or "overlay" or "surfboard effect" that is common to all radar systems (Peral et al., 2015). Following Chelton et al. (1989) we can estimate the apparent horizontal displacement. For a satellite altitude h and using $\zeta \ll R$, the calculation for a flat mean sea surface gives

$$\delta_r \simeq \sqrt{r^2 - 2h\zeta} - r. \tag{8}$$

For a spherical Earth of radius R_E, ζ should be replaced by $\zeta/(1 + h/R_E)$.

In the particular case where $\zeta = -H_s$ and $r = 0$, δ_r is the radius r_C of oceanographic footprint as defined by Chelton et al. (1989), and given by eq. (1), when the range resolution δ_R is neglected compared to H_s. For $H_s = 10$ m, and $h = 519$ km, this gives $r_C = 3.3$ km.

We may give the following interpretation of r_C. At points located at r_C from nadir (i. e. at the edge of the "Chelton footprint") there is only a 0.003% probability that $\zeta > H_s$ and that these points contribute to the waveform at ranges $R < h$, i.e. in the first half of the rising part of the waveform. In practice, points outside of the footprint (located at $r > r - C$) do not contribute to the middle part of the waveform that most contributes to the fit of σ_H and the estimation of H_s.

If wave heights vary as a function of distance to nadir, then the waveform does not follow exactly the Brown form, as detailed in Appendix A. As different regions of the waveform contain different regions of the sea surface, one could imagine fitting different parts of the waveform to measure variations in H_s as a function of distance from nadir. The theoretical limit to this capability is the blurring due to range bunching over a distance of the order $r_C/2$. Speckle noise is another limiting factor, and probably the main one in practice for small wave heights.

Based on the analysis in Appendix A we expect that variations of H_s at scales much smaller than $r_C/4$ will be smoothed out in altimeter data, whereas variations at scales much larger than $r_C/2$ have no effect on the waveform that will follow the Brown shape for the local wave height. For our analysis of CFOSAT data we will define an "effective altimeter radius" r_a such that the variance of H_s associated to the random fluctuations of the envelope filtered with a Gaussian filter of standard deviation r_a, is the same as that produced by an altimeter. The actual shape of the "altimeter filter" is discussed in Appendix A and varies in its details with the details of the retracking algorithm.

2.4 Estimation of the equivalent r_a scale for an idealized altimeter

We have simulated the sampling of our simulated sea surface by a highly simplified altimeter. We thus neglect radar noise, speckle and variations in ocean backscatter, and compute simulated waveforms as histograms of the number of discrete pixels as a function of range R discretized with the same resolution $\delta_R = 0.47$ m used in actual SWIM data. The histogram is computed for a finite region of size r_C by r_C centered at the nadir point. The value of H_s for each simulated histogram is taken to be the H_s of the theoretical waveform given by eq. (7) that best fits the simulation for R varying from $h - H_s$ to $h + H_s$, using least square fit. As detailed in Appendix A, even this simplified altimeter makes a much more complex measurement than a simple Gaussian smooth-

ing of the H_s field. We briefly tested that more realistic waveforms and different fitting procedures yield some quantitative differences.

Taking the simulated sea surface from Fig. 2, we compare a map of simulated altimeter data in Fig. 3 with maps of local wave heights, smoothed on different scales.

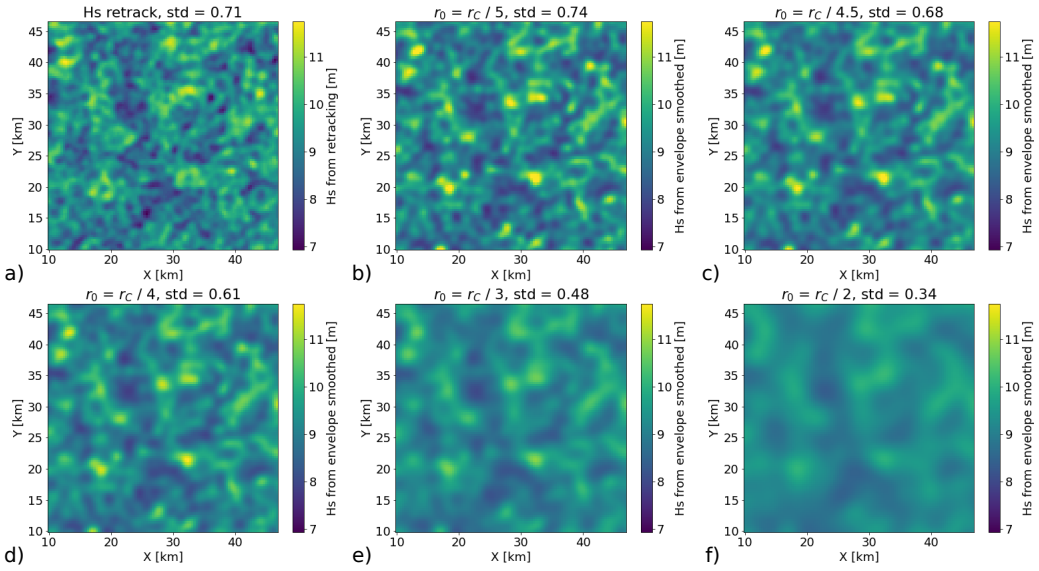

Figure 3. Maps of wave heights obtained by either simulating altimeter processing (top left) or smoothing the envelope with a Gaussian filter of standard deviation r_0 varied from $r_C/5$ to $r_C/2$. In this example, $r_C = 3063$ m thus r_0 values are respectively 613, 681, 766, 1021, and 1531 m. In practice the smoothing is applied in a finite box of size $4r_C$ by $4r_C$.

As expected, the large scales of the envelope, those that persist in the bottom-right panel of Fig. 3, match the large scales of the simulated altimeter data. From a quantitative point of view, the standard deviation of the simulated altimeter data, here 0.63 m, is of the same order as the standard deviation of actual SWIM measurements over the same SWIM box. We also note that this value is very close to that obtained for a filtering of the envelope between a scale $r_a = r_C/5$ and $r_a = r_C/4.5$.

Looking at Fig. 3.a) it is clear that the map of retracked H_s contains much smaller features than the envelope smoothed with $r_a = r_C/4.5$. All of these are spurious amplification of envelope perturbations that happen to be at the right distance from nadir, around $r_C/2$, as explained in Appendix A. As a result, maxima of H_s given by the altimeter are not located at the true H_s maxima but slightly displaced by a distance of

the order of $r_C/2$. A striking example in Fig. 3 is the region of waves higher than 11 m around $x = 32$ km, $y = 22$ km. The altimeter gives a local minimum where the true wave height is maximum, and a round halo of maxima surrounding that point. Conversely a ring-shaped maximum in the envelope, such as around $x = 39$ km, $y = 23$ km, gives a local maximum in the simulated altimeter data. We expect that sensitivity may vary with the actual retracking procedure, and this discussion is beyond the scope of the present paper.

Even though the patterns do not exactly coincide, we will now assume that the sampling of the sea surface by the altimeter is equivalent, in terms of variability of H_s to filtering the envelope with a Gaussian of standard deviation $r_a = r_C/4.5$.

2.5 Generic sea states, envelopes and H_s variability

Based on our analysis, we expect that SWIM measurements of H_s are contaminated by wave group structures at scales of the order of a few kilometers, following the variation of r_C with wave height and satellite altitude. As illustrated by the two examples with different spectral width, we note that for the same wave height, a wider spectrum leads to smaller scales of wave groups, part of which scales are smoothed away by the altimeter footprint and therefore not resolved. For a narrower spectrum, wave groups have larger scales and amplitudes and a larger contribution to the variability of wave heights estimated by an altimeter.

For a simple quantitative analysis we may consider the more simple case of waves propagating in only one direction, with a sea surface ζ distributed with the normal law $\mathcal{N}(0, \sigma_H = H_s/4)$ with a one-sided Gaussian spectrum (defined for $k > 0$)

$$E(k) = \frac{H_s^2}{16\sigma_k\sqrt{2\pi}} \mathrm{e}^{-(k-k_p)^2/(2\sigma_k^2)}. \tag{9}$$

The spectrum of the envelope is also Gaussian and the H_s PSD writes (for a one-sided spectrum),

$$\Psi_{H_s}(k) = \frac{4-\pi}{\pi\sqrt{\pi}\sigma_k} \cdot H_s^2 \mathrm{e}^{-k^2/(4\sigma_k^2)}. \tag{10}$$

Wave groups contain wavelengths larger than π/σ_k, with a constant spectral density near $k = 0$. Around $k = 0$, the value of the Hs spectrum is $0.15H_s^2/\sigma_k$ m^2/(rad/m).

Fig. 4 presents one dimensional wave spectra - in solid lines - of two typical sea states with same $H_s = 3.11$ m and their associated H_s spectra $\Psi_{H_s}(k)$- in dashed lines. The light blue spectrum is a JONSWAP spectrum (Hasselmann et al., 1973) with a peak period of 8 s and a peak enhancement factor $\gamma = 3.3$ that represents a moderate wind-sea. The dark blue spectrum is a narrow Gaussian spectrum with a peak period of 14 s and $\sigma_k = 0.002$ rad/m, typical of swell conditions in the open ocean. The altimeter smoothing function $G_{r_a} = \exp(-k^2 r_a^2)$ allows to define a cut-off wave number $k_a = \sqrt{\pi}/(2r_a)$. As shown in Fig. 4 the wavelengths in altimeter-filtered envelopes, larger than the associated wavelength cut-off $2\pi/k_a$ (in black dash-dotted line), are large compared to the shortest wavelengths contained in the wave groups (of order $\pi\sqrt{2}/\sigma_k$ and represented by the dark and light blue vertical dash-dotted lines).

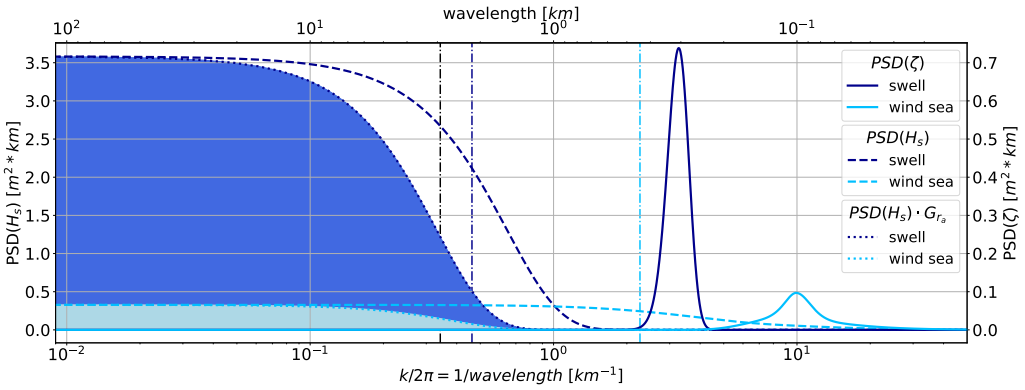

Figure 4. Example of two wave spectra - solid lines - in one dimension and the corresponding spectra of H_s - dashed lines -, for typical swell conditions in the open ocean in dark blue, and typical moderate wind windsea in light blue. Because the fluctuations of H_s are filtered by the altimeter with the function $G_{r_a}(k)$ - dotted lines -, the actual measured variance of H_s is the shaded area, in light blue for the windsea and dark blue for the swell. The vertical black line is the equivalent altimeter cut-off wavenumber at $k = k_a$, whereas the vertical dark and light blue lines represents the width of the H_s spectra.

Applying the one dimension version of eq. (6) gives the variance of altimeter-estimated H_s as the shaded areas in Fig. 4. For a Gaussian spectrum, in cases where the altimeter filter scale is large enough not to be concerned about the shortest scales, this area is approximately k_a times $\Psi_{H_s}(k = 0)$ the H_s PSD level at $k = 0$. This gives a stan-

dard deviation of H_s of the order of $0.39\sqrt{k_a/\sigma_k}H_s$, which is 0.40 H_s for the one-dimensional swell example of Fig. 4.

For a generic one-dimensional wave spectrum $E(k)$, the width σ_k should be replaced by the the bandwidth $B_k/(2\sqrt{\pi})$, with B_k defined like the usual frequency bandwidth (Saulnier et al., 2011),

$$B_k = \frac{H_s^4}{256\int_0^\infty E^2(k)\mathrm{d}k}. \tag{11}$$

For a JONSWAP spectrum, $B_k = 1.3k_p$ and the standard deviation of H_s for the wind sea case above is $0.1H_s$.

For waves in two dimensions, the directional spread of the energy leads to a further reduction of the variability of H_s. Using the spectrum of the envelope at $k = 0$ we may define a two-dimensional spectral bandwidth B_{kk}

$$B_{kk}^2 = \frac{H_s^4}{256\Psi_2(k_x=0,k_y=0)/8} = \frac{H_s^4}{256\int_{-\infty}^{\infty}\int_{-\infty}^{\infty}E^2(k_x,k_y)\mathrm{d}k_x\mathrm{d}k_y}. \tag{12}$$

When r_a is large enough we can consider that Ψ is constant for $k < 1/r_a$, which gives

$$\mathrm{std}(H_s)_{\mathrm{wg}} \simeq \frac{\sqrt{4-\pi}}{B_{kk}}H_s\sqrt{2/r_a^2 - 4k_1/(\sqrt{\pi}r_a)}. \tag{13}$$

2.6 Summary of methodology

In the previous subsections, various considerations have been made. Here, we summarize them to give a flow chart for estimating the part of the variability due to wave groups $\mathrm{std}(H_s)_{\mathrm{wg}}$ from CFOSAT products.

1. Assemble the 1-dimensional IWWOC-L2S spectra for each azimuth to obtain an equivalent CWWIC-L2 spectrum, make it double-sided $E_{2S}(k,\theta)$ and rescale it with H_s from nadir measurement,
2. Interpolate $E_{2S}(k,\theta)$ over a regular (k_x,k_y) grid, with k_x the along track direction, to obtain $E(k_x,k_y)$,
3. Compute the spectrum of the envelope squared $\Psi_2(k_x,k_y)$ from the discrete correlation

$$\Psi_2(k_x,k_y) = 8\cdot\sum_{k'_x}\sum_{k'_y}\left[E(k'_x,k'_y),E(k'_x+k_x,k'_y+k_y)\right]\mathrm{d}k'_x\mathrm{d}k'_y \qquad \text{(Step 3)}$$

4. Transform to a PSD of H_s,

$$\Psi_{H_s}(k_x,k_y) = 4\sqrt{\frac{2}{\pi}}\cdot\frac{8-2\pi}{H_s^2}\cdot\Psi_2(k_x,k_y) \qquad \text{(Step 4)}$$

where H_s is computed as $4 \cdot \sqrt{E}$, with $E = \iint_{\mathbb{R}^2} E(k_x, k_y) \mathrm{d}k_x \mathrm{d}k_y$.

5. Define a G_{r_a} with $r_a = r_C/4.5$ as

$$G_{r_a}(k_x, k_y) = |\mathcal{F}(g_{r_a})|^2 = \mathrm{e}^{-(k_x^2+k_y^2)\cdot r_a^2} \quad \text{(Step 5)}$$

6. Apply the filter to Ψ_{H_s} to obtain the PSD of altimeter H_s estimate,

$$\Psi_{H_s,r_a} = \Psi_{H_s} \cdot G_{r_a} \quad \text{(Step 6)}$$

7. Integrate $\Psi_{H_s,r_a}(k_x, k_y)$ over $\mathbb{R}$ for k_y and $\mathbb{R}_{\setminus[-k_1,k_1]}$ and take the square-root to obtain $\mathrm{std}(H_{s,r_a}, L_1)_{\mathrm{wg}}$.Because we compare our estimate to H_s variations with a SWIM L2 box size that is 80km along-track, L_1 is taken as 2×80 km,

$$\mathrm{std}(H_s)_{\mathrm{wg}} = \mathrm{std}(H_{s,r_a}, L_1)_{\mathrm{wg}} = \int_{k_y \in \mathbb{R}} \int_{k_x \in \mathbb{R}_{\setminus[-k1,k1]}} \Psi_{H_s,r_a}(k_x, k_y) \mathrm{d}k_x \mathrm{d}k_y \quad \text{(Step 7)}$$

Fig. 5 shows the results of steps 3, 6 and 7 for the two selected boxes of our case study. The top line corresponds to the Ψ_2 spectra obtained from correlation, the middle line shows the PSD of our local H_s estimate Ψ_{H_s,r_a} (note the different colour scales between the northern - A - and southern - B - boxes), whereas the bottom line shows the one sided k_x-spectra after integration along k_y, with the plain vertical line showing the integration limit over k_x.

Fig. 6 shows wave height and corresponding standard deviation, both observed and estimated from L2S spectrum, as a function of the sampling time (UTC) over storm Dennis. For the northern part of the storm, where the spectrum is broader, around box A (light blue vertical line), the standard deviation due to wave groups is around half the measured standard deviation (i.e. wave groups represent a quarter of the measured variance). On the other hand, for the southern part, around box B (dark blue), the wave height variability is strongly dominated by wave groups - more than half the observed variance is explained by wave groups.

Alternatively we can approximate the full integral of the convolution by its value at $k = 0$ using the bandwidth B_{kk} , giving a faster estimate of the variability due to wave groups. The first two steps are the same, then

- Instead of the full convolution, compute only B_{kk} defined in eq. (12), which can be re-written as,

$$B_{kk} = \frac{\iint_{\mathbb{R}^2} E(k_x, k_y) \mathrm{d}k_x \mathrm{d}k_y}{\sqrt{\iint_{\mathbb{R}^2} E^2(k_x, k_y) \mathrm{d}k_x \mathrm{d}k_y}} \quad \text{(Step 3bis)}$$

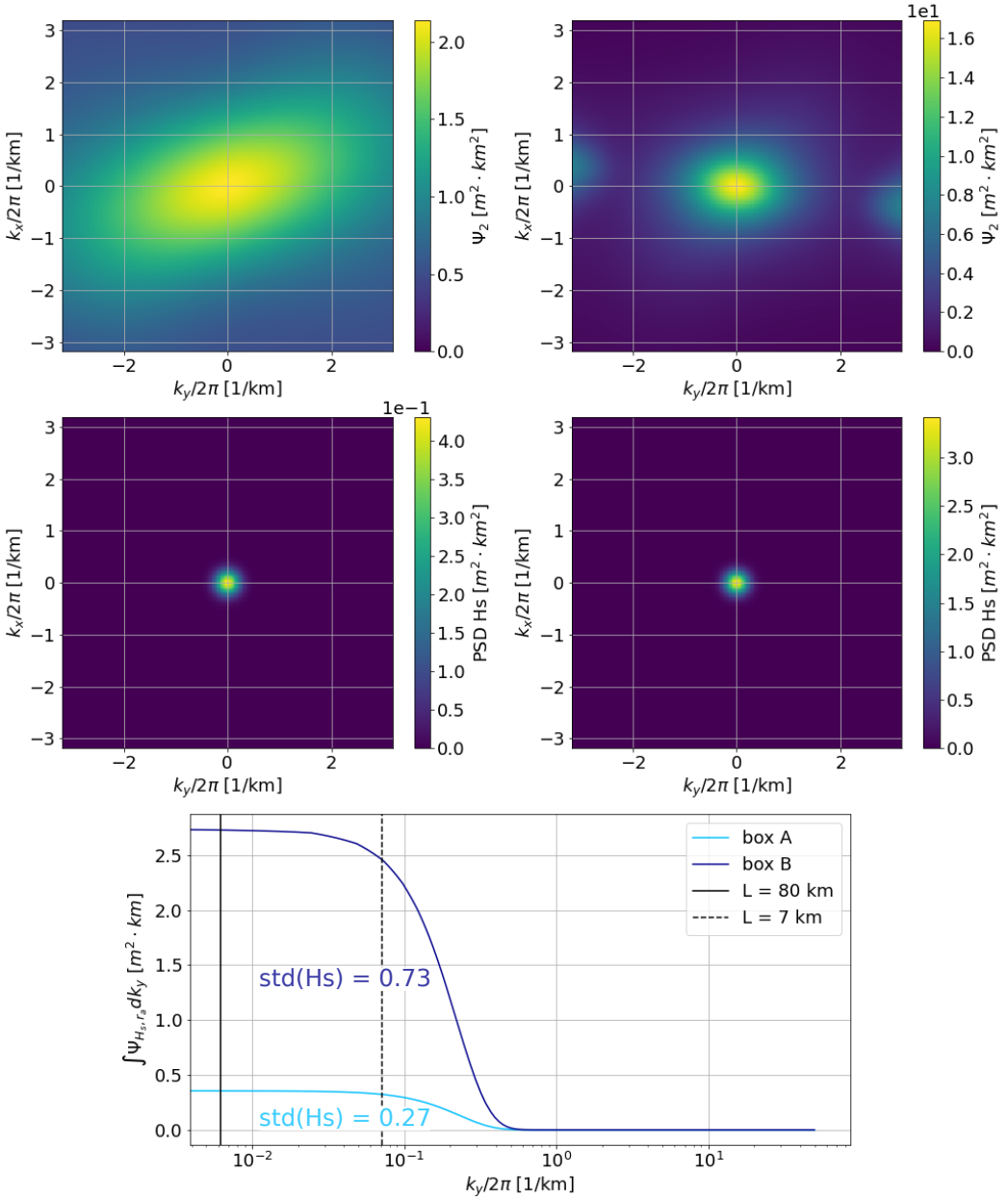

Figure 5. Left column corresponds to our chosen northern CFOSAT box, and right column to the southern box. Top line: cnvelope squared spectrum $\Psi_2(k_x, k_y)$ from convolution. Middle line: spectrum of $H_s^{r_a}$ Ψ_{H_s,r_a} (including the equivalent altimeter filtering). Bottom line: 1D along-track spectrum obtained by integrating over the cross-track axis, in light blue for the northern box and dark blue for the southern box.

- skip steps 4–6 to estimate $\mathrm{std}(H_s)_{\mathrm{wg}}$ directly using eq. (13),

$$\mathrm{std}(H_s)_{\mathrm{wg}} \simeq \frac{\sqrt{4-\pi}}{B_{kk}} H_s \sqrt{2/r_a^2 - 4k_1/(\sqrt{\pi} r_a)}. \qquad \text{(Step 7bis)}$$

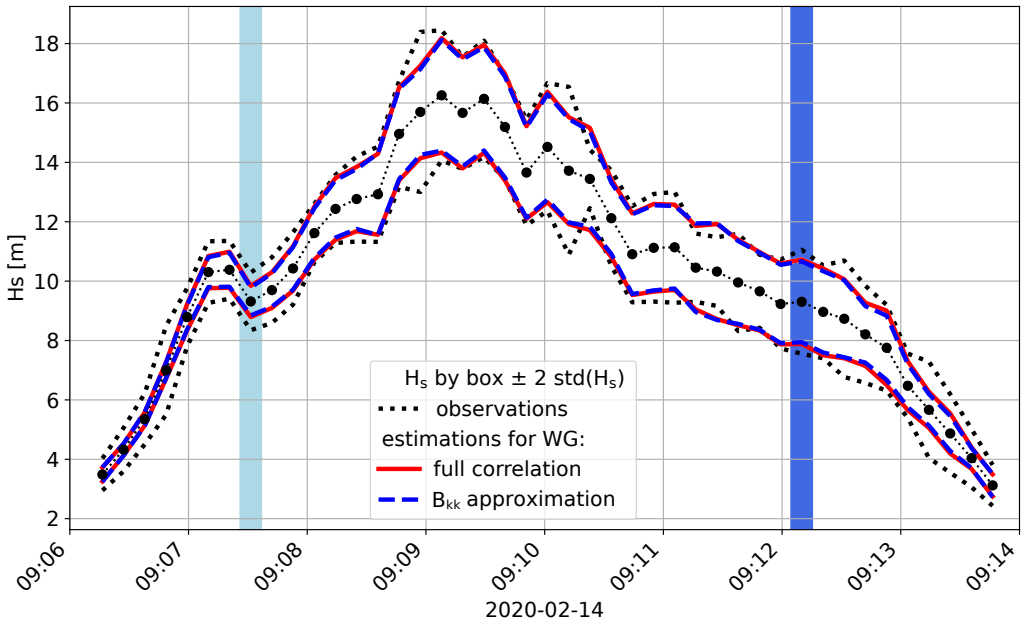

Figure 6. Values of measured H_s, averaged over boxes - black circles - , and corresponding std(Hs) - black dotted lines - ; as provided in the L2-CWWIC as a function of sampling time (UTC), for the CFOSAT track shown in Fig. 1. Estimations of std$(H_s)_{\mathrm{wg}}$ are also represented - in red and blue - using the two methods summarized at the end of section 2.

This std$(H_s)_{\mathrm{wg}}$ estimated through B_{kk} is also shown in Fig. 6. The values are only slightly overestimated compared to the full correlation calculus, therefore, B_{kk} could be a useful parameter when working with wave groups.

3 Results at the global scale

Beyond the particular case of storm Dennis, for which very large wavelength and narrow spectra lead to a dominant effect of wave groups in H_s variability, how important are wave groups in general, and how important can they be compared to other known sources of H_s variability, including winds and currents?

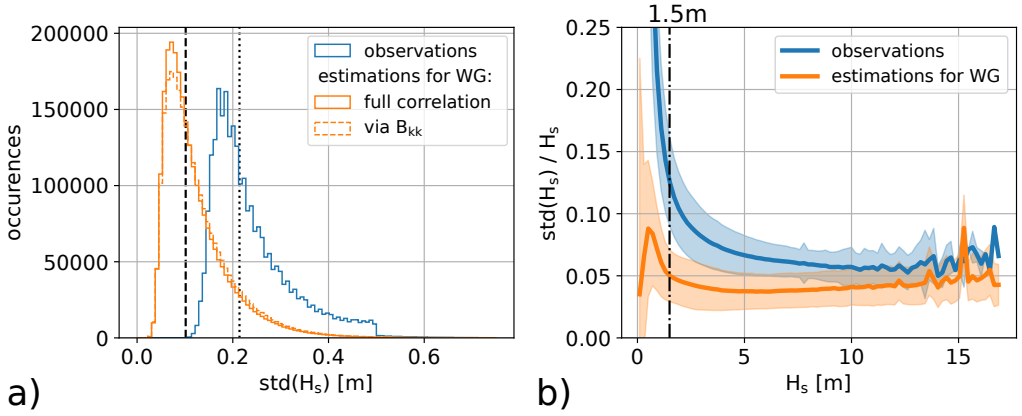

Figure 7. (a) Histograms of std(H_s) measured at nadir in blue and our estimate of wave groups contribution std$(H_s)_{\mathrm{wg}}$ in orange. (b) Mean - solid lines - and standard deviation - shaded areas - of std$(H_s)/H_s$ over H_s bins of 0.2 m, both for std(H_s) measured at nadir in blue and our estimate of wave group effects in orange.

We have thus applied the methodology presented in section 2 for storm Dennis to the full SWIM L2S archive for the years 2020 and 2021, estimating for each of the 2.4 million SWIM L2 box the expected value of std$(H_s)_{\mathrm{wg}}$ associated to wave groups as filtered by the altimeter. The distribution of these values is shown in Fig. 7.a, with a typical value around 7 cm, and maximum values around 60 cm. This variability is typically half of the measured standard deviation of H_s.

We also computed std$(H_s)_{\mathrm{wg}}$ as estimated from the bandwidth B_{kk} for the same time period, giving results that are highly correlated to the full convolution.

In practice the group-induced variability of H_s that is resolved by altimeters is strongly correlated with the mean value of H_s.

In Fig. 7.b we show the statistical distribution (mean and standard deviation) of std(H_s)/mean(H_s) as a function of H_s. For H_s below 1.5 m the altimeter estimates of

H_s are known to have the largest relative errors (Dodet et al., 2022), which is partially due to a stronger effect of speckle noise, as discussed in Appendix A.3. In that range the wave group variability is 3 times smaller than the observed variability.

Above 1.5 m, the relative variability that is expected from wave groups increases with H_s (from 3.5% to 5%), whereas the observed variability decreases from 11% to 5% between $H_s = 1.5$m and $H_s = 10$m. The share of the variability expected from wave groups dominates the observed variability for wave heights above 8 m, and probably explains the increase in observed std(H_s)/mean(H_s) for H_s above 12 m. Although there are very few data in that range, it is well known that dominant wave periods must be higher for higher wave heights (Toba, 1973), corresponding to smaller bandwidths and thus an ever increasing std$(H_s)_{\mathrm{wg}}/H_s$.

We now consider the spatial distribution of std(H_s), and in order to separate the possible effects of different sea states from the general trends associated to local average value of H_s, we have chosen to show a map of the mean value of std(H_s)/H_s. Before computing the local mean we have first removed all cases with $H_s < 1.5$ m. Fig. 8.a shows the distribution of std(H_s)/mean(H_s) and, for comparison, std$(H_s)_{\mathrm{wg}}$/mean(H_s) in Fig. 8.b.

Note that the range of values are different for both panels because the contribution of wave groups is, on average, half of the measured std(H_s). Both figures have some common patterns with a general increase from the west to the east of the ocean basins consistent with a dominance of swells in the east (Chen et al., 2002) with longer wavelengths and narrower spectra.

We may also remove the contribution of wave groups to look at the other sources of variability in H_s. As shown in Fig. 8.c, the standard deviation of H_s corrected for the effects of wave groups contains a background level of 0.1 to 0.2 m, probably associated to speckle noise and small scale wind variability, and stronger localized values up to 0.3 m. These large values are co-located with regions of strong ocean circulation mesoscale variability. These same regions match the location of strong H_s gradient in along-track 1 Hz data from Saral-Altika, Jason-2 and Cryosat-2 that have been denoised using an Empirical Mode Decomposition (EMD), by Quilfen and Chapron (2019). Here, we have applied the same EMD filtering to SWIM 5 Hz data, instead of 1 Hz in the literature, in order to decontaminate the nadir H_s from the wave group effect, giving results shown

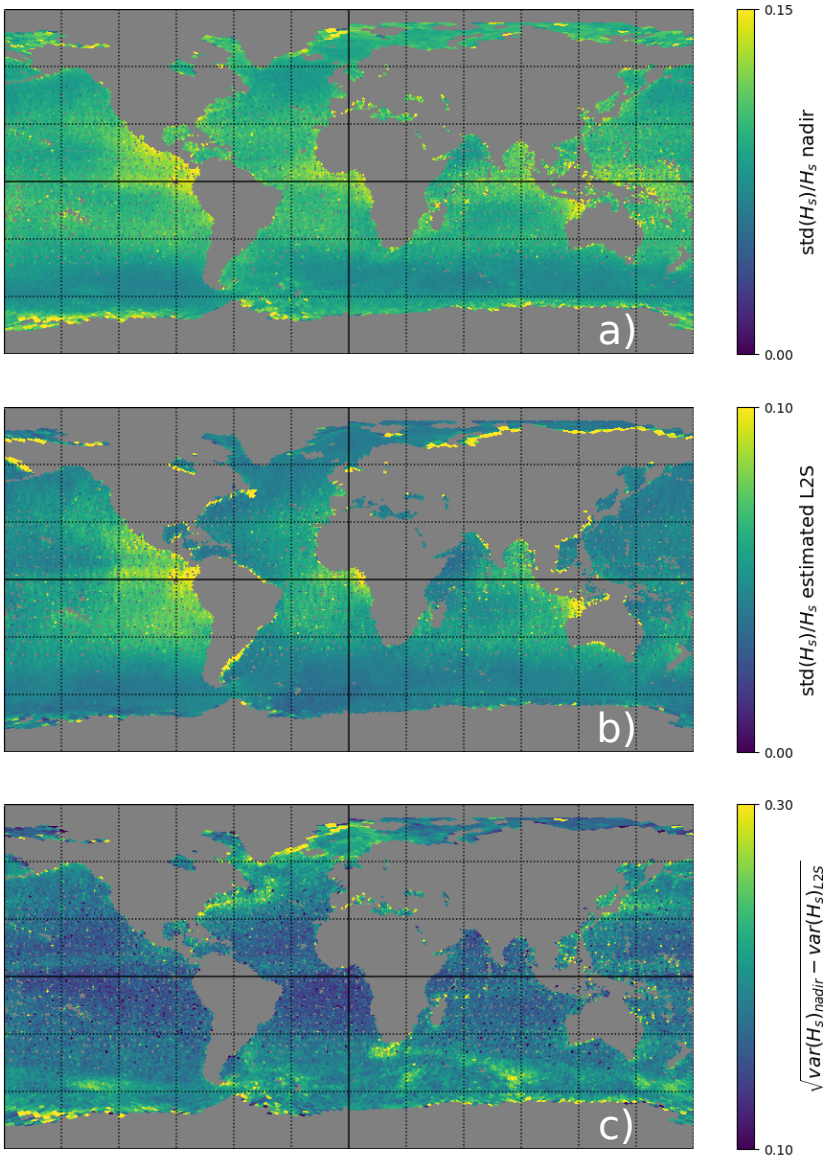

Figure 8. Map of the average of a) std(H_s)/mean(H_s) - upper panel -, b) std$(H_s)_{\mathrm{wg}}$/mean(H_s) -middle panel - and c) residual standard deviation of H_s, in meters, after removing the effect expected from wave groups - lower panel -, for the years 2020 and 2021 for all the SWIM L2-IWWOC boxes with a H_s above 1.5 m. With the wave group contribution std$(H_s)_{\mathrm{wg}}$ estimated from SWIM L2S spectra

in Fig. 9. The EMD filtered part Fig. 9.c is directly comparable to the wave group signature highlighted in Fig. 8. These maps were constructed using SWIM nadir data from SALP/CAWATAC experimental 5 Hz products available on Aviso+ that include both the raw H_s estimate and the denoised values using the EMD method. The magnitude

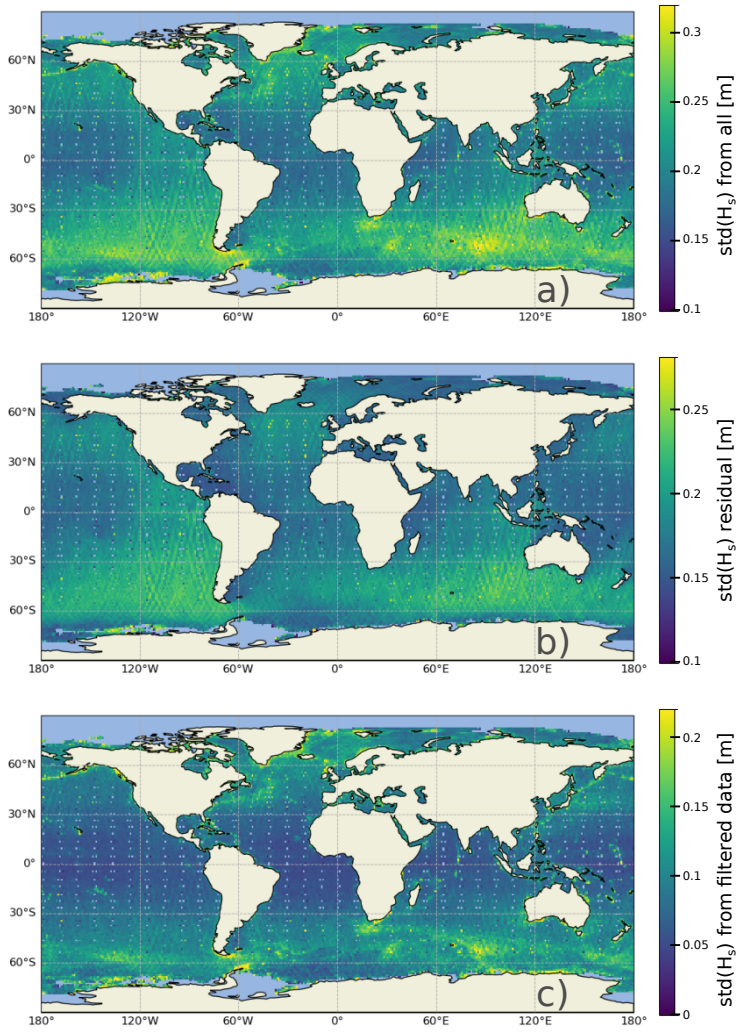

Figure 9. Maps of the average, for the year 2021, of (a) std(H_s) computed on original SWIM nadir native values (5 Hz), (b) standard deviation of the residual of H_s, defined as the difference between the original and the denoised wave height (c) std(H_s) computed on EMD filtered data.

and distribution of the expected effect of wave groups apparently corresponds to the variability that is removed by EMD denoising, without using wave spectrum information. Thus, the uncertainty variable associated to the nadir 5 Hz data in the SALP/CAWATAC products which is derived from the standard deviation of the fluctuations removed by EMD should be related to H_s and B_{kk}. As these products are available for other satellite missions for which no wave spectra are measured, further analysis may provide a more careful quantification of the estimate of wave groups effects removal.

4 Discussion

4.1 Effect of spectral shape

The accurate estimation of wave group contributions critically depends on the accuracy of the spectral shape, in particular the directional width and wavenumber width. Because of the hard wavelength cut-off in the L2 product we had chosen to work with the L2S spectra. Redoing the global analysis with the L2 product generally reduces the expected effect of wave groups.

We note that a validation of spectral width from the L2 product was performed by Le Merle et al. (2021), who found that SWIM L2 generally overestimate spectral width compared to buoy data. No such analysis has been performed for the L2S product. It would be also interesting to know how accurate could be the estimation of $\mathrm{std}(H_s)_{\mathrm{wg}}$ estimated from model spectra, for the application to other satellite mission that do not measure the wave directional spectrum.

It should also be reminded that SWIM L2 spectra combine sparse measurements over a 70 km by 80 km box, as illustrated in Fig. 10. Because the wave field has gradi-

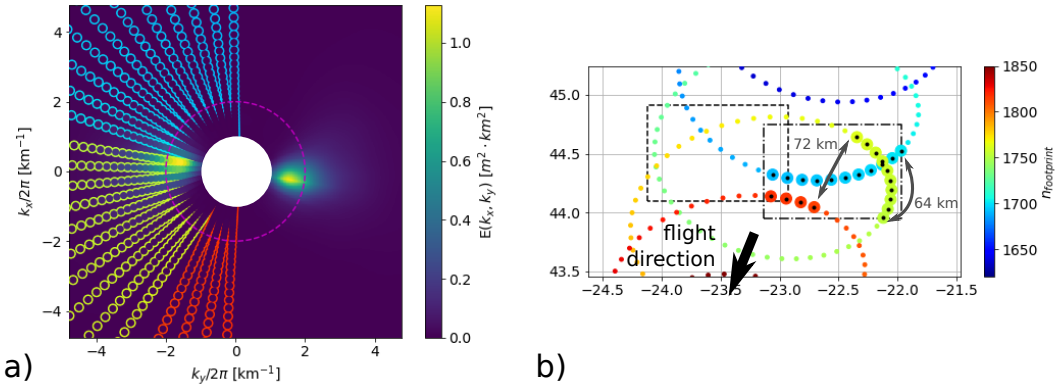

Figure 10. (a) Representation of a two-dimensional spectrum $E(k_x, k_y)$ with values given by the colorbar obtained from assembling L2 1-dimensional spectra $E(k)$ for all azimuths. The color of each circle corresponds to the index of the beam footprint in which the SWIM was making the measurement (b) Geographical layout of boxes - dashed and dash-dotted rectangles - and of centers of the beam footprints on the sea surface. the footprint diameter is about 20 km so that they actually overlap.

ents, this combination generally produces a broader spectrum than the a more local es-

timate of the wave spectrum, and this should produce a low bias in our estimate the effect of wave groups. In the example on Fig. 10 the assembly of the L2 spectrum combines data from two neighboring wave azimuths that are observed in distinct regions of the ocean separated by up to 72 km. We kept this assembly to be able to compare results from L2 and L2S data, but it would be more logical, for the case of L2S data, to assemble a spectrum with a spatial continuity of the footprints that correspond to azimuths around the spectral peaks.

4.2 Effects of satellite altitude

The particularly low orbit of CFOSAT at 519 km gives a rather small oceanic footprint that allows for wave groups to be resolved in SWIM data. If we consider the higher altitudes used by other satellite missions, 891 km for the recently launched SWOT or 1340 km for the Topex-Poseidon / Jason / Sentinel 6 series, the oceanic footprint gets bigger and wave groups are more likely to be more smoothed out. In Fig. 11, we illustrate this effect with different altitudes following the method used for Fig. 3. Namely, for the same simulated ocean surface, the wave height is estimated by a least-square fit to the simplest Brown waveform given by eq. (7). As expected, the higher the satellite the lower the variability of H_s. It is not clear that this effect of satellite altitude is noticeable in real data that are contaminated by speckle noise and that use different waveform fitting algorithms. More realistic simulations will be needed to compare the behaviour or different instruments and processing chains.

4.3 Expected effect on delay doppler altimeters

We have shown that the variability of H_s at small scale contains some geophysical information and not just random noise related to the measurement. However, the noise for Delay-only altimeters is probably dominated by the speckle noise in the waveforms (Sandwell & Smith, 2005; Quartly et al., 2019). Doppler processing of recent altimeter instruments starting with Cryosat-2 and Sentinel-3 can strongly reduce this speckle noise by forming and combining independent looks of the same sea surface (Egido et al., 2021). It will therefore be interesting to study the effect of wave groups in these measurements of wave height and sea level. Waves can also be resolved directly in the sea level estimates when data is processed at very high resolution (Altiparmaki et al., 2022; Villas Bôas et al., 2022). If the Doppler induced by orbital velocities is neglected, the delay-Doppler

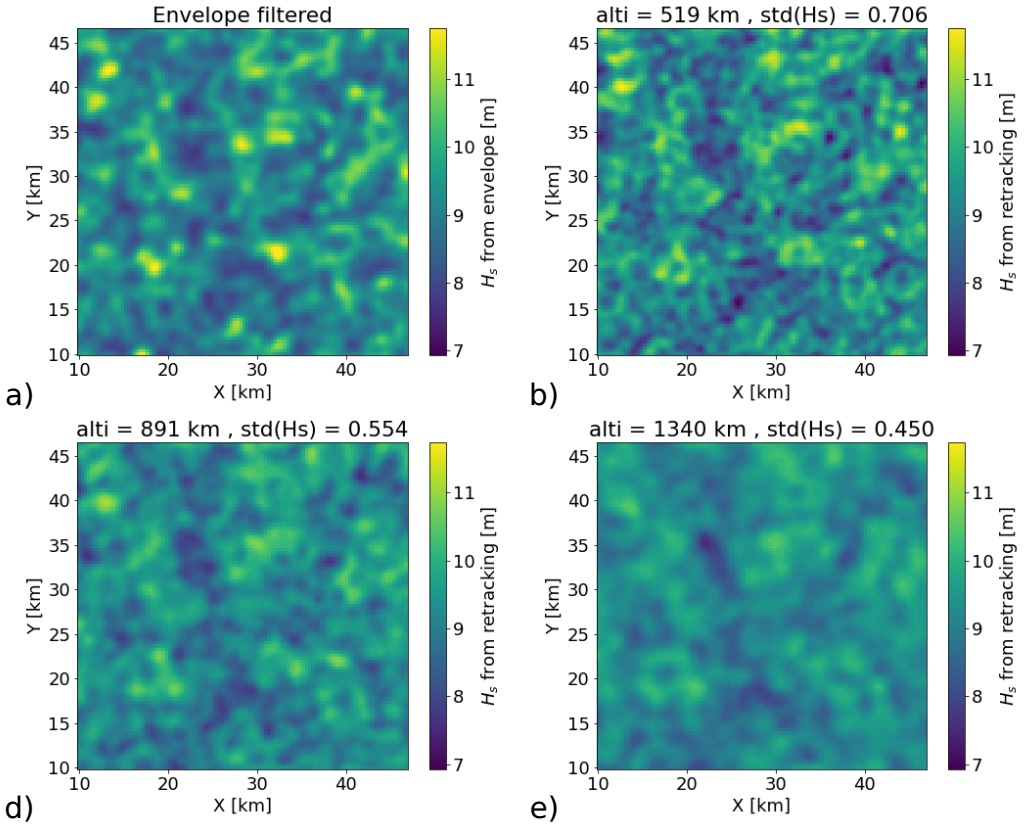

Figure 11. Maps of wave heights obtained a) by smoothing the envelope with Gaussian filter of scale $r_a = 619$ m; or by simulating altimeter waveforms without speckle and using the same least-squares fit (Appendix A), for different altitudes: b) 519 km, c) 891 km, d) 1,340 km, with corresponding r_a of 619 m, 790 m and 940 m.

measurement is similarly based on the convolution of a surface elevation distribution with a flat surface response (Ray et al., 2015). Only the flat surface response is different from the Delay-only processing. We thus expect that wave groups will have similar distortion of the waveforms and contributions to estimates of wave heights and sea level. The blurring effect caused by range bunching will now be confined to the direction perpendicular to the track, with maximum effect of a H_s perturbation located off the satellite track (depending on fitting algorithm), possibly also at a distance of the order of $r_C/2$. Because Delay-Doppler altimeters can actually resolve the along-track variability caused by wave groups instead of averaging it, we expect that H_s fluctuations caused by wave groups are much larger in Delay-Doppler altimetry, together with their spurious effect on sea level estimates. This may explain the relative smaller reduction of std(H_s) at large

H_s which is found when Doppler resolution is enhanced to reduce the speckle effect, and a typical value of std(H_s) for Delay-Doppler Sentinel 3A data which that is around 0.7 m for $H_s = 7$ m (Egido et al., 2021), twice the typical value for SWIM data. This will be the topic of further studies.

4.4 Wave groups and satellite measurements uncertainties

Up to now, the uncertainty of satellite measurements has been determined by the triple-collocation method (Abdalla et al., 2011; Dodet et al., 2022), with the practical result that the uncertainty of altimeter data, either denoised or integrated along-track into super-observations, is of the order of 7% of H_s. However, that error contains representation errors (the co-located in situ data does not sample the same space and time frame), and cannot be extrapolated beyond the range of the co-located dataset, typically wave heights below 8 m. So what can we say about the largest measured wave heights of 20.1 m (Hanafin et al., 2012)? Can we use the measured variability of H_s, for example the 5 Hz or 20 Hz data that is used to make a 1 Hz average, to refine our estimate of the uncertainty of this average? In the present paper we have shown that wave groups are responsible for random fluctuations in H_s estimates, that are generally proportional to H_s but with an effect that depends on the bandwidth of the spectrum, which is generally narrower for larger wave periods. As a result the variability associated to wave groups can be the dominant source of fluctuations in H_s measurements for severe storm conditions. Even though the measurement fluctuations are weakly correlated to the actual wave height variations (as demonstrated in Fig. 3) their magnitudes are strongly correlated. Hence the measured fluctuation std(H_s) contains both uncorrelated speckle noise effect, that can be expected to be reduced by $1/\sqrt{N}$ when averaged from N Hz to 1 Hz, and a true geophysical spatial variability associated to wave groups (and variable fetch, currents, etc.) that will partially average out. We expect that an uncertainty model for averages of H_s measurements may take into account wave groups explicitly. In the case of SWIM, directional wave spectra can be used to separate the actual variability of the 5 Hz data into wave group effects and noise plus other geophysical effects. For other altimeters, one may use empirical correlations between spectral bandwidth, wave height and wind speed. For this information to be useful for a theoretically-based uncertainty estimate, which is much needed for wave heights above 8 m, one may extend the param-

eterization of speckle effects proposed in Appendix A.3, to the actual target waveform and cost function used in the retracking algorithm.

4.5 Considerations on the satellite resolution

The present work should be useful for the exploration of the resolution limits of satellite altimeters and other remote sensing systems that use radar or optical imagery (Kudryavtsev et al., 2017). As processing methods are refined to produce higher resolution near the coast (Passaro et al., 2021) and the ice edge (Collard, 2022), some of the high resolution data will be dominated by wave groups. The associated variance of H_s may provide some constraint on the shape of the directional wave spectrum, but the detailed fluctuations are probably of little value for most applications as groups will travel at speeds of the order of 10 m/s and persist for only a few minutes. The contribution of wave groups to the variability of wave heights measured by altimeters is thus a real effect that contains part of the true variability of wave heights at the scale of the altimeter footprint. Methods developed to remove noise in the data, such as the data-driven Empirical Mode Decomposition (EMD) used by (Quilfen & Chapron, 2019) appear to remove the effect of wave groups. An investigation of the variabilty of wave heights at the smallest scales cannot be based on denoised data alone, because they miss a large part of the true variability.

In locations where H_s varies sharply such as over coral reefs, mud banks or across the sea ice edge, the high resolution wave heights will contain other effects, and these are particularly interesting. Some caution should be used when interpreting these sharp gradients. As we have found out, the maximum wave height will generally be displaced from the location of its true maximum. This displacement is smallest for the SWIM instrument, thanks to the low orbit of CFOSAT, which makes it a particularly interesting instrument for studying small scale wave height variations, in spite of its rather low rate for the nadir beam (5 Hz instead of 20 Hz for Jason), and the absence of Doppler processing.

5 Conclusion

In this paper, we took advantage of the low orbit altitude of CFOSAT, and the low noise level of the nadir beam of the SWIM instrument to study the along-track variabil-

ity of wave height. The directional wave spectra measured by off-nadir beams on SWIM has been complementary to study the relationship between wave spectra and along-track H_s variability. After giving a theoretical estimate of the standard deviation of H_s associated to wave groups as a function of the wave spectrum and satellite altitude, we computed this estimate for 2 years of CFOSAT data using IWWOC-L2S products. We found that the standard deviation of H_s associated to wave groups is generally about half of the standard deviation of H_s measured over a 80 km distance, explaining 25% of measured H_s variance. This ratio of variances increases for storms and in the presence of long swells, it was found to be larger than 75% in 3% of the cases.

The residual variability after substracting the estimated effect of wave groups from the measured Hs variance correlates positively with along-track variance of filtered signals, which brings out regions of strong currents. Studying these features is of major interest and requires some filtering out of the smaller scales. In turn, these smaller scales can be of interest, at least from a statistical point of view, as they are related to wave groups and the generation of infragravity waves and extreme sea level at the coast.

The main novelty of the present work was to represent the non-Gaussian sea level statistics caused by wave groups at the scale of a satellite altimeter footprint. To our knowledge that effect had never been considered, in spite of its strong effect on the radar waveforms (see Fig. A1) much larger than the typical effect of wave nonlinearly introduced by Rodriguez (1988). We have shown that the wave group effect averages out to zero over large scales when waveforms are fitted with a simple least square cost function, but that is not necessarily the case for the more sophisticated methods that are often used. We expect that further work will expand on our approach to consider spurious effects on sea level estimates as well as applications to recent delay-Doppler altimeters.

Appendix A Non-homogeneous H_s and waveform retracking

In this analysis we keep the most simple model of altimeter measurement that is also used in section 2: we neglect antenna pattern, thermal noise and and mispointing effects, and neglect the Earth sphericity. These assumptions are meant to simplify the algebra as much as possible while keeping the essential features of non-homogeneity in wave heights. Likewise we have used the most simple cost function when fitting the waveform, while maximum likelihood methods are generally used with real data (Rodriguez, 1988; Halimi, 2013). We also start by ignoring speckle noise. The analysis performed below is easily extended to consider the third parameter which is usually estimated in retracking wave forms, that is the Normalized Radar Cross Section.

A1 Wave groups and H_s estimate

We consider a small perturbation Δ_H of H_s over an area A, localized around a range $h+R_0$. The original normalized Brown waveform of eq. (7) corresponds to the histogram of the ocean area per unit range, divided by $2\pi h$ so that it varies between 0 and 1, with h the satellite altitude. The perturbation to the waveform is equivalent to removing the original Gaussian distribution of surface elevation with $\sigma_H = H_s/4$ over the area A, and replacing it by a new Gaussian with $\sigma' = (H_s+\Delta_H)/4$, over the same area A, and divide by the normalization factor $2\pi h$. We define the parameter $a = A\Delta_H/(8\pi h)$, which should be small compared to H_s^2. For a small change in H_s, this change in waveform is proportional to the derivative of the Gaussian distribution with respect to σ_H and we find that the waveform is now

$$w(R) = w_B(R,\sigma_H) + a\frac{\mathrm{e}^{-(R-h-R_0)^2/(2\sigma_H^2)}}{\sqrt{2\pi}}\frac{(R-h-R_0)^2-\sigma_H^2}{\sigma_H^4} + O(a^2) \qquad \text{(A1)}$$

We note that a smaller change Δ_H over a larger area A changes the waveform in the same way as a larger change over a smaller area, provided that a is the same. For simplicity we redefine the Chelton footprint diameter as $r'_C = \sqrt{2H_s h}$, and we find that taking an area of radius $\alpha r'_C$ gives $a = \alpha^2\Delta_H H_s/4$.

The shape of these distorted waveforms is illustrated in Fig. A1. With the exaggerated distortion shown here, fitting a Brown waveform would give a wave height of $H_{s,\mathrm{fit}} =$ 12.6 m for $R_0 = 2.5$ m and $H_{s,\mathrm{fit}} = 10$ m for $R_0 = 0$, which is a strange way to average the $H_s = 13$ m over part of the footprint and 10 m in the rest of the footprint.

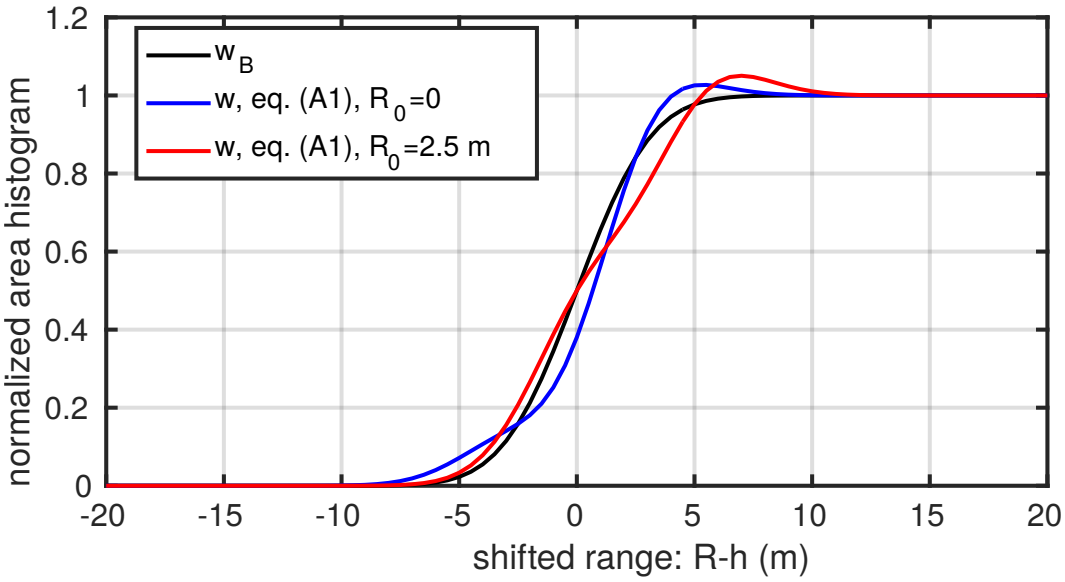

Figure A1. Example waveforms in the presence of a localized change in H_s around the range $h + R_0$, for $H_s = 10$ m. In order to be visible, the perturbation was exaggerated taking $a = 1.875$ m^2, that would correspond to Δ_H=3 m over an area of radius $r'_C/4$, a perturbation that is neither small nor localized.

For smaller values of the perturbation a, the deviation in the fitted H_s can be computed analytically.

For simplicity we will assume that the waveforms are defined for $-\infty < R < \infty$, and the sum of the difference squared between $w(R)$ and $w_B(R, \sigma'_H)$, when integrated from $R = -\infty$ to $R = -\infty$ is the following cost function,

$$\begin{aligned} C &= \int_{-\infty}^{\infty} \{[w_B(R,\sigma_H) - w_B(R,\sigma'_H)] + [w(R) - w_B(R,\sigma_H)]\}^2 \, \mathrm{d}R \\ &\simeq \int_{-\infty}^{\infty} \left\{ (\sigma_H - \sigma'_H) \frac{\partial w_B(R,\sigma_H)}{\partial \sigma_H} + [w(R) - w_B(R,\sigma)] \right\}^2 \mathrm{d}R \\ &= (\sigma'_H - \sigma_H)^2 \frac{1}{4\sqrt{\pi}\sigma_H} + (\sigma'_H - \sigma_H) \frac{aR_0}{8\sqrt{\pi}\sigma_H^5} \mathrm{e}^{-R_0^2/(4\sigma_H^2)} (R_0^2 - 6\sigma_H^2) + \frac{3a^2}{8\sqrt{\pi}\sigma_H^3}. \end{aligned}$$

Fitting σ'_H corresponds to solving $\partial C / \partial(\sigma'_H - \sigma_H) = 0$. We note that that error terms that are either not a function of $(\sigma'_H - \sigma_H)$ or odd functions of R have no impact on the fitted value. For example the a^2 term in eq. (A1) does not contribute any difference to the fit.

We find that the fitted value differs from the background value H_s by a factor proportional to a and function of R_0/H_s ,

$$H_{s,\mathrm{fit}} = H_s + \frac{A}{\pi h}\frac{\Delta_H}{H_s}\underbrace{\left[2\frac{R_0}{H_s}\left(6-\left(\frac{4R_0}{H_s}\right)^2\right)\mathrm{e}^{-4R_0^2/H_s^2}\right]}_{J(R_0/H_s)}, \tag{A2}$$

with the function J in brackets having a maximum close to 2 for $R_0 \simeq H_s/4$, as shown in Fig. A2.

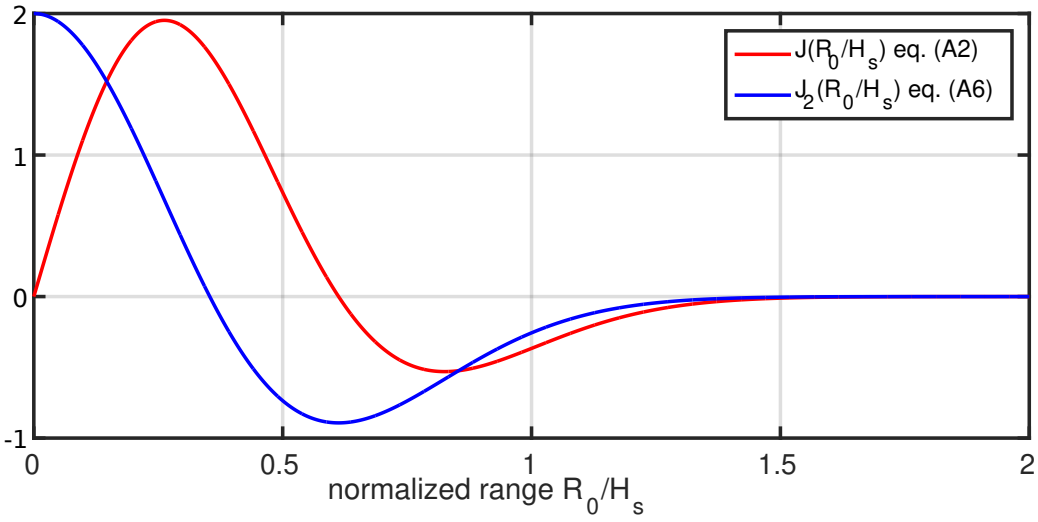

Figure A2. Functions $J(R_0/H_s)$ and $J_2(R_0/H_s)$ corresponding to the term in square brackets in eqs. (A2) and (A8). The maximum of J is at $R_0/H_s = 0.5\sqrt{0.5(3-\sqrt{6})} \simeq 0.26$, where J takes a value close to 1.96. This location corresponds to a distance from nadir approximately $\sqrt{0.26}r'_C \simeq r'_C/2$.

We note that this perturbation is zero for $R_0 = 0$, meaning that a localized change at the center of the footprintdoes not modify the estimated H_s. This lack of impact on $H_{s,\mathrm{fit}}$ comes from the fact that the perturbation of the waveform (the second term in eq. A1) is an odd function of range and thus orthogonal to the even functions that are the Brown waveforms with zero epoch $w_B(R, \sigma_H)$. The maximum perturbation of $H_{s,\mathrm{fit}}$ occurs for H_s perturbations at a range R_0 close to σ_H, i.e. corresponding to a distance from nadir of $r'_C/4$. Eq. (A2) gives results that are fairly robust for finite values of a/H_s^2, and would predict a wave height of 12.9 m in the case $R_0 = 2.5$ m shown in Fig. A1.

We now consider the average effect of the perturbation by computing the average over R_0, taking all values of R_0 from 0 to nH_s, which corresponds to averaging over an

area $B = \pi n {r'_C}^2 = 2n\pi H_s h$. The integral of the function in brackets is

$$I = \int_0^\infty 2\frac{R_0}{H_s}\left(6 - 16\frac{R_0^2}{H_s^2}\right) \mathrm{e}^{-4R_0^2/H_s^2} \mathrm{d}R_0 = 0.5 H_s. \tag{A3}$$

As a result, the average effect of a Δ_H change over an area $A = \pi\alpha^2 {r'_C}^2 = 2\pi\alpha^2 h H_s$ is, when n is large,

$$\delta_{H,\mathrm{alti}} = \frac{1}{nH_s}\int_0^{nH_s} (H_{s,\mathrm{fit}} - H_s)\,\mathrm{d}R_0 = \frac{1}{2n}\frac{A}{\pi h}\frac{\Delta_H}{H_s} = \frac{\alpha^2}{n}\Delta_H. \tag{A4}$$

This average effect of the localized perturbation of H_s is the same as a true area average, which is the perturbation times the ratio of the areas A and B, namely $\delta_H = \Delta_H A/B$. In other words, the perturbation is amplified if located at $0.15 < r/r'_C < 0.34$ from nadir, by a factor J that is up to 2. Otherwise the perturbation is attenuated, so that on average it is equal to the true perturbation. This averaging property and the unbiased estimate of $H_{s,\mathrm{fit}}$, with a perturbation that changes sign when Δ_H changes sign, are specific to the simple least squares used here. For example, fitting the logarithm of the waveform produces a biased estimator and a non-zero response for $R_0 = 0$. Hence the results presented here are specific to the fitting method.

In practice, distributed anomalies of H_s are not only a function of the distance from nadir, so that a local estimate of H_s will combine positive and negative anomalies Δ_H that are located at the same distance from nadir, and will partially cancel. This explain that our best fit for r_0 is $r_C/4.5$, smaller than the $r_C/2$ which is a more typical scale of the footprint. Instead of retracking the simulated altimeter data, we can reproduce the H_s variability by first summing the Δ_H anomalies for a given r, compute the $H_{s,\mathrm{fit}}$ anomaly for that r using eq. (A2) and then sum those anomalies for all r, as demonstrated in Fig. A3. This procedure is equivalent to a spatial filter $\mathcal{J}(r)$ that is built from the J function, converting the range $h + R_0$ to a horizontal distance from nadir $r = \sqrt{2hR_0}$,

$$\mathcal{J}(r) = G_{r_C}(r) + J \otimes (Id - G_{r_C})(r) \tag{A5}$$

where, G_{r_C} is a Gaussian filter with width r_C, and Id is the identity function. The estimated H_s thus comes from

$$H_s(x) = 4\sqrt{\frac{2}{\pi}} \cdot (\mathcal{J} \otimes \eta)(x) \tag{A6}$$

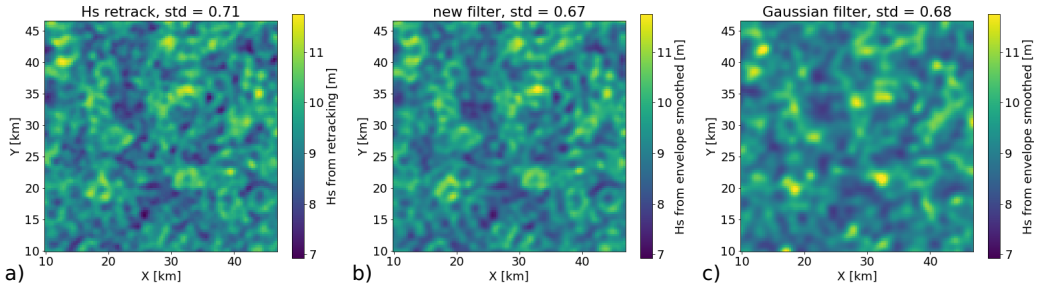

Figure A3. Equivalent to Fig. 3: (a) H_s surface obtained from retracking and H_s surfaces obtained from convoluting the envelope with (b) a spatial filter built from the J function, (c) a gaussian filter with $r_a = r_C/4.5$.

A2 Wave groups and sea level estimate

While perturbations at nadir do not change the H_s estimate, they would change the mean sea level z_e (the epoch is $-z_e$) when using a 2-parameter waveform

$$w_{B2}(R, \sigma_H, z_e) = \frac{1}{2}\left[1 + \mathrm{erf}\left(\frac{(R + z_e) - h}{\sqrt{2}\sigma_H}\right)\right]. \tag{A7}$$

In the case shown in Fig. A1 with $R_0 = 0$ the estimated mean sea level is $z = -37$ cm. We thus expect wave groups to contribute to fluctuations in the estimated sea level at the scale of groups. The estimation of that effect follows the same method used above. Fitting $w_{B2}(R, \sigma'_H, z_e)$ to our waveform $w(R)$ given by eq. (A1) is obtained by minimizing a modified cost function, that is the same as C but with one extra term $z_e \partial w_{B2}/\partial z_e$ inside the curly brackets, giving two extra non-zero terms proportional to z_e^2 and z_e. We note that the cross-term proportional to $z_e(\sigma'_H - \sigma_H)$ is an odd function of R and thus integrates to zero. After integration over R we get the cost function,

$$C_2 = C + \frac{z_e^2}{2\sqrt{\pi}\sigma_H} + \frac{a z_e}{4\sqrt{\pi}\sigma_H^2} \mathrm{e}^{-R_0^2/(4\sigma_H^2)} \left(\frac{R^2}{\sigma_H^2} - 2\right).$$

Taking the derivative of C_2 with respect to z_e gives

$$z_e = -\frac{A\Delta_H}{2\pi h H_s} \underbrace{\left[\left(2 - 16\frac{R_0^2}{H_s^2}\right) \mathrm{e}^{-4R_0^2/H_s^2}\right]}_{J_2(R_0/H_s)}. \tag{A8}$$

The function J_2 is plotted in Fig. A2. Hence z_e has the strongest deviation when the wave height perturbation is centered at nadir, and the sign of the deviation is opposite to Δ_H: i.e. a wave group centered at the nadir would give a spurious lower sea level. On average the z_e deviation has a zero mean when R_0 is varied. As a result of the different shapes of J and J_2, there is no simple correlation of the H_s and z_e perturbations,

contrary to the correlations induced by speckle noise in the waveform measurement (Sandwell & Smith, 2005).

There is some correlation for R_0/H_s between 0.7 and 1.2 which may contribute to anti-correlation of sea level anomalies and wave heights at scales around r_C, and thus may persist in 1 Hz data. We insist that these are spurious sea level variations. In deep water these spurious oscillations are much larger than the fraction of a millimeter associated to true sea level variations with bound infragravity elevation that is anti-correlated with the envelope of kilometer-scale wave groups (Ardhuin et al., 2004). The spurious sea level oscillations described are also probably generally larger in amplitude than the larger scale (20-km wavelength) true sea level variations associated to free infragravity waves that have no phase correlation with the local envelope (Ardhuin et al., 2014). In shallow water, the real sea level fluctuations can be more important.

A3 Speckle noise

Random fluctuations in the electromagnetic power measured by the radar combine an additive thermal noise that can often be neglected and a multiplicative noise that is caused by the Rayleigh fading of the interfering reflections off a random sea surface (Quartly et al., 2001). In fact speckle is to the radar power what wave groups are to the wave energy. A good model for the speckle is a multiplicative random noise, so that the measured waveform for each range is multiplied by a factor $(1+\varepsilon(R))$ with $\varepsilon(R)$ following a χ^2 distribution with $N(R)$ degrees of freedom depending on the number of pulses averaged and the pulse repetition frequency (Quartly et al., 2001).

For the retracking, the effect of this speckle perturbation is one additional term $\varepsilon(R)w(R)$ inside the curly brackets of the cost function. Expanding the square and expressing the integral, it gives two terms, one proportional to $(\sigma'_H - \sigma_H)$ that is relevant to the H_s estimate and the other proportional to z_e fit, so that the cost function is now,

$$C_3 \simeq C_2 - 2(\sigma'_H - \sigma_H)\int_{-\infty}^{\infty}\varepsilon(R)w(R)\frac{\partial w_{B2}}{\partial \sigma_H}\mathrm{d}R - 2z_e\int_{-\infty}^{\infty}\varepsilon(R)w(R)\frac{\partial w_{B2}}{\partial z_e}\mathrm{d}R, \qquad \text{(A9)}$$

with

$$\frac{\partial w_{B2}}{\partial \sigma_H} = -\frac{R-h+z_e}{\sigma_H^2\sqrt{2\pi}}\mathrm{e}^{-(R-h+z_e)^2/(2\sigma_H^2)}, \qquad \text{(A10)}$$

and

$$\frac{\partial w_{B2}}{\partial z_e} = \frac{1}{\sigma_H\sqrt{2\pi}}\mathrm{e}^{-(R-h+z_e)^2/(2\sigma_H^2)}. \qquad \text{(A11)}$$

The estimated wave height that gives $\partial C_3/\partial(\sigma'_H - \sigma_H) = 0$ thus has an extra term induced by speckle noise,

$$H_{s,\mathrm{fit}} = H_s + \frac{A}{\pi h}\frac{\Delta_H}{H_s} J(R_0/H_s) + 16\sqrt{2}H_s \int_{-\infty}^{\infty} \varepsilon(u)\left(1+\mathrm{erf}(2\sqrt{2}u)\right) u\mathrm{e}^{-8u^2}\mathrm{d}u, \quad \text{(A12)}$$

with $u = (R - h + z_e)/H_s$. The speckle-induced perturbation of $H_{s,\mathrm{fit}}$ is a weighted sum of random fluctuations with zero mean. In practice we can consider $\varepsilon(R)$ to be Gaussian, and the variance of the speckle perturbation is the sum of the variances associated to each range R times the weight squared. To get some useful order of magnitude we may take the variance of $\varepsilon(R)$, which is $1/N(R)$, to be constant at $1/N$. For large values of H_s, the discretized waveform is well approximated by the continuous form and the part of the variance of $H_{s,\mathrm{fit}}$ induced by the speckle is approximately 5.0 H_s/N, with a standard deviation $2.24\sqrt{H_s/N}$. Using the value $N = 512$ for the number of pulses of the SWIM nadir beam that we may assume to be independent, and $H_s = 2$ m, this gives a standard deviation of 0.14 m, broadly consistent with the background level in Fig. 8.c. However, we note that the magnitude of the variability of $H_{s,\mathrm{fit}}$ will depend on the method used to fit the waveform. In the case of the SWIM data, the adaptive method that is used is based on a maximum likelihood (Tourain et al., 2021). It is probably more robust to speckle noise perturbations than the least square estimate used here, in particular for this instrument that has a relatively high signal to noise ratio.

Acknowledgments

All CFOSAT data are provided by courtesy of CNSA and CNES. This research was made possible by support from ESA as part of the Sea State CCI project. MDC is currently supported by a postdoctoral grant from the Centre National d'Études Spatiales (CNES). MDC would like to thank JF Piolle from Ifremer for the data management support.

Open Research

The L2 and L2P SWIM data sets used here corresponds to the files reprocessed in version 5.1.2 and made available by CNES on the ftp server of AVISO+ (ftp-access.aviso.altimetry.fr, directories cfosat/swim_l2_op05 and cfosat/swim_l2p_box_nrt/), accessible to anyone after registration.

The L2S SWIM data set was obtained from Ifremer at https://data-cersat.ifremer.fr/projects/iwwoc/swi_l2s

The denoised CFOSAT data used for Fig. 9 is available at https://doi.org/10.24400/527896/a01-2022.013

References

Abdalla, S., & Cavaleri, L. (2002). Effect of wind variability and variable air density on wave modelling. *J. Geophys. Res.*, *107*(C7), 17.

Abdalla, S., Janssen, P., & Bidlot, J.-R. (2011). Altimeter near real time wind and wave products: Random error estimation. *Marine Geodesy*, *34*, 396–406. doi: 10.1080/01490419.2011.585113

Alday, M., Accensi, M., Ardhuin, F., & Dodet, G. (2021). A global wave parameter database for geophysical applications. part 3: Improved forcing and spectral resolution. *Ocean Modelling*, *166*, 101848. doi: 10.1016/j.ocemod.2021.101848

Altiparmaki, O., Kleinherenbrink, M., Naeije, M., Slobbe, C., & Visser, P. (2022). Sar altimetry data as a new source for swell monitoring. *Geophys. Res. Lett.*. doi: 10.1029/2021GL096224

Ardhuin, F., Chapron, B., & Elfouhaily, T. (2004). Waves and the air-sea momentum budget, implications for ocean circulation modelling. *J. Phys. Oceanogr.*, *34*, 1741–1755. doi: 10.1175/1520-0485%282004%29034%3C1741%3AWATAMB%3E2.0.CO%3B2

Ardhuin, F., Rascle, N., Chapron, B., Gula, J., Molemaker, J., Gille, S. T., ... Rocha, C. (2017). Small scale currents have large effects on wind wave heights. *J. Geophys. Res.*, *122*(C6), 4500–4517. doi: 10.1002/2016JC012413

Ardhuin, F., Rawat, A., & Aucan, J. (2014). A numerical model for free infragravity waves: Definition and validation at regional and global scales. *Ocean Modelling*, *77*, 20–32. doi: 10.1016/j.ocemod.2014.02.006

Ardhuin, F., Stopa, J. E., Chapron, B., Collard, F., Husson, R., Jensen, R. E., ... Young, I. (2019). Observing sea states. *Frontiers in Marine Sci.*, *6*, 124. doi: 10.3389/fmars.2019.00124

Arhan, M., & Ezraty, R. (1978). Statistical relations between successive wave heights. *Oceanol. Acta*, *1*, 151–158.

Badulin, S. I. (2014). A physical model of sea wave period from altimeter data. *J. Geophys. Res.*, *119*, 856–869. doi: 10.1002/2013JC009336

Brown, G. S. (1977). The average impulse response of a rough surface and its appli-

cations. *IEEE J. Oceanic Eng.*, *2*(1), 67–63. doi: 10.1109/JOE.1977.1145328

Chelton, D. B., Walsh, E. J., & MacArthur, J. L. (1989). Pulse compression and sea level tracking in satellite altimetry. *J. Atmos. Ocean Technol.*, *6*, 407–438. doi: 10.1175/1520-0426(1989)006⟨0407:pcaslt⟩2.0.co;2

Chen, G., Chapron, B., Ezraty, R., & Vandemark, D. (2002). A global view of swell and wind sea climate in the ocean by satellite altimeter and scatterometer. *J. Atmos. Ocean Technol.*, *19*, 1849–1859.

Collard, L. a. F. a. M. a. E. F. a. F., Fabrice and Marié. (2022). Wind-wave attenuation in arctic sea ice: A discussion of remote sensing capabilities. *J. Geophys. Res.*, *127*, e2022JC018654. doi: 10.1029/2022JC018654

Dodet, G., Abdalla, S., Alday, M., Accensi, M., Bidlot, J., & Ardhuin, F. (2022). Error characterization of significant wave heights in multidecadal satellite altimeter product, model hindcast, and in situ measurements using the triple collocation technique. *J. Atmos. Ocean Technol.*, *39*, 887–901. doi: 10.1175/JTECH-D-21-0179.1

Dodet, G., Piolle, J.-F., Quilfen, Y., Abdalla, S., Accensi, M., Ardhuin, F., ... Donlon, C. (2020). The sea state cci dataset v1: towards a sea state climate data record based on satellite observations. *Earth System Sci. Data*, *12*, 1929–1951. doi: 10.5194/essd-12-1929-2020

Egido, A., Dinardo, S., & Ray, C. (2021). The case for increasing the posting rate in delay/Doppler altimeters. *Adv. Space Res.*, *68*, 930–936. doi: 10.1016/j.asr.2020.03.014

Halimi, A. (2013). *From conventional to delay/doppler altimetry* (Doctoral dissertation, INP Toulouse, Toulouse, France). Retrieved from `https://theses.hal.science/tel-00951973`

Hanafin, J., Quilfen, Y., Ardhuin, F., Sienkiewicz, J., Queffeulou, P., Obrebski, M., ... Stutzmann, E. (2012). Phenomenal sea states and swell radiation: a comprehensive analysis of the 12-16 February 2011 North Atlantic storms. *Bull. Amer. Meterol. Soc.*, *93*, 1825–1832. doi: 10.1175/BAMS-D-11-00128.1

Hasselmann, K., Barnett, T. P., Bouws, E., Carlson, H., Cartwright, D. E., Enke, K., ... Walden, H. (1973). Measurements of wind-wave growth and swell decay during the Joint North Sea Wave Project. *Deut. Hydrogr. Z.*, *8*(12), 1–95. (Suppl. A)

Hauser, D., Tison, C., Amiot, T., Delaye, L., Corcoral, N., & Castillan, P. (2017). SWIM: The first spaceborne wave scatterometer. *IEEE Trans. on Geosci. and Remote Sensing*, *55*(5), 3000–3014.

Hauser, D., Tourain, C., Hermozo, L., Alraddawi, D., Aouf, L., Chapron, B., ... Tran, N. (2021). New observations from the SWIM radar on-board CFOSAT: Instrument validation and ocean wave measurement assessment. *IEEE Trans. on Geosci. and Remote Sensing*, *59*(1), 5–26. doi: 10.1109/tgrs.2020.2994372

Jackson, F. C., Walton, W. T., & Peng, C. Y. (1985). A comparison of in situ and airborne radar observations of ocean wave directionality. *J. Geophys. Res.*, *90*(C1), 1005–1018.

Kudryavtsev, V., Yurovskaya, M., Chapron, B., Collard, F., & Donlon, C. (2017). Sun glitter imagery of surface waves. part 1: Directional spectrum retrieval and validation. *J. Geophys. Res.*, *122*. doi: 10.1002/2016JC012425

Lavrenov, I. V. (2001). Effect of wind wave parameter fluctuation on the nonlinear spectrum evolution. *J. Phys. Oceanogr.*, *31*, 861–873. Retrieved from `http://ams.allenpress.com/archive/1520-0485/31/4/pdf/i1520-0485-31-4-861`

Le Merle, E., Hauser, D., Peureux, C., Aouf, L., Schippers, P., Dufour, C., & Dalphinet, A. (2021). Directional and frequency spread of surface ocean waves from swim measurements. *J. Geophys. Res.*, *126*(7), e2021JC017220. doi: 10.1029/2021JC017220

Longuet-Higgins, M. S. (1984). New integral relations for gravity waves of finite amplitude. *J. Fluid Mech.*, *149*, 205–215. (see also Yu and Wu, J. Fluid Mech., 1987)

Masson, D., & Chandler, P. (1993). Wave groups: a closer look at spectral methods. *Coastal Eng.*, *20*, 249–275.

Passaro, M., Cipollini, P., Vignudelli, S., Quartly, G. D., & Snaith, H. M. (2014). ALES: A multi-mission adaptive subwaveform retracker for coastal and open ocean altimetry. *Remote sensing of Environment*, *145*, 173–189.

Passaro, M., Hemer, M. A., Quartly, G. D., Schwatke, C., Dettmering, D., & Seitz, F. (2021). Global coastal attenuation of wind-waves observed with radar altimetry. *Nature communications*, *12*, 3812. doi: 10.1038/s41467-021-23982-4

Peral, E., Rodriguez, E., & Esteban-Fernandez, D. (2015). Impact of surface waves on SWOT's projected ocean accuracy. *Remote Sensing*, *7*(11), 14509–14529.

889 doi: 10.3390/rs71114509

890 Quartly, G. D., Smith, W. H. F., , & Passaro, M. (2019). Removing intra-1-Hz co-
891 variant error to improve altimetric profiles of σ_0 and sea surface height. *IEEE*
892 *Trans. on Geosci. and Remote Sensing*, *57*(6), 3741–3752. doi: 10.1109/TGRS
893 .2018.2886998

894 Quartly, G. D., Srokosz, M. A., & McMillan, A. C. (2001). Analyzing altimeter arti-
895 facts: Statistical properties of ocean waveforms. *J. Atmos. Ocean Technol.*, *18*,
896 2074–2091. doi: 10.1175/1520-0426(2001)018⟨2074:AAASPO⟩2.0.CO;2

897 Quilfen, Y., & Chapron, B. (2019). Ocean surface wave-current signatures from
898 satellite altimeter measurements. *Geophys. Res. Lett.*, *216*, 253-261. doi: 10
899 .1029/2018GL081029

900 Ray, C., Martin-Puig, C., Clarizia, M. P., Ruffini, G., Dinardo, S., Gommengin-
901 ger, C., & Benveniste, J. (2015). SAR altimeter backscattered waveform
902 model. *IEEE Trans. on Geosci. and Remote Sensing*, *53*, 911–919. doi:
903 10.1109/TGRS.2014.2330423

904 Rice, S. (1944). Mathematical analysis of random noise. In N. Wax (Ed.), *Noise and*
905 *stochastic processes* (pp. 133–294). New York: Dover Publications Inc. (pub-
906 lished 1954).

907 Rodriguez, E. (1988). Altimetry for non-gaussian oceans: Height biases and es-
908 timation of parameters. *J. Geophys. Res.*, *93*, 14107–14120. doi: 10.1029/
909 JC093iC11p14107

910 Sandwell, D. T., & Smith, W. H. F. (2005). Retracking ers-1 altimeter waveforms
911 for optimal gravity field recovery. *Geophys. J. Int.*, *163*, 79–89. doi: 10.1111/
912 j.1365-246X.2005.02724.x

913 Saulnier, J.-B., Clément, A., de O. Falcão, A. F., Pontes, T., Prevosto, M., & Ricci,
914 P. (2011). Wave groupiness and spectral bandwidth as relevant parameters
915 for the performance assessment of wave energy converters. *Ocean Eng.*, *38*(1),
916 130-147.

917 Tayfun, A., & Lo, J.-M. (1989). Wave envelope and related spectra. *J. of Waterway,*
918 *Port Coast. Ocean Eng.*, *115*, 515–533. doi: 10.1061/(ASCE)0733-950X(1989)
919 115:4(515)

920 Toba, Y. (1973). Local balance in the air-sea boundary processes. III on the spec-
921 trum of wind waves. *J. Oceanogr. Soc. Japan*, *29*, 209–220. Retrieved from

http://www.terrapub.co.jp/journals/JO/JOSJ/pdf/2905/29050209.pdf

Tourain, C., Piras, F., Ollivier, A., Hauser, D., Poisson, J. C., Boy, F., ... Tison, C. (2021). Benefits of the adaptive algorithm for retracking altimeter nadir echoes: Results from simulations and CFOSAT/SWIM observations. *IEEE Trans. on Geosci. and Remote Sensing*, *59*, 9927–9940. doi: 10.1109/TGRS.2021.3064236

Tournadre, J. (1993). Time and space scales of significant wave heights. *J. Geophys. Res.*, *98*(C3), 4727–4738.

Villas Bôas, A. B., Lenain, L., Cornuelle, B. D., Gille, S. T., & Mazloff, M. R. (2022). A broadband view of the sea surface height wavenumber spectrum. *Geophys. Res. Lett.*, *49*(e2021GL096699). doi: 10.1029/2021GL096699

Young, I. R., Zieger, S., & Babanin, A. V. (2011). Global trends in wind speed and wave height. *Science*, *332*, 451–455. doi: 10.1126/science.1197219

Wave groups and small scale variability of wave heights observed by altimeters

Marine De Carlo[1], Fabrice Ardhuin[1], Annabelle Ollivier[2], Adrien Nigou[2]

[1]Univ Brest, CNRS, Ifremer, IRD, Laboratoire d'Océanographie Physique et Spatiale (LOPS), IUEM, F29280, Plouzané, France.

[2]Collecte Localisation Satellite (CLS), Ramonville Saint-Agne, France

Key Points:

- Wave groups contribute to small-scale fluctuations in altimeter wave heights, explaining 25% of the variance measured by CFOSAT in 80 km.
- For the same wave height, fluctuations are larger in the presence of long and narrow-banded waves, typical of swell-dominated conditions.
- Altimeters smooth out scales shorter than the square root of half the H_s times the altitude, and distort spatial patterns at that scale.

Corresponding author: Marine De Carlo, mdecarlo@ifremer.fr

Abstract

Recent satellite altimeter retracking and filtering methods have considerably reduced the noise level in estimates of the significant wave height (H_s), allowing to study processes with smaller spatial scales. In particular, previous studies have shown that wave-current interactions may explain most of the variability of H_s at scales 20 to 100 km. As the spatial scale of the measurement is reduced, random fluctuations emerge that should be associated to wave groups. Here we quantify the magnitude of this effect, and the contribution of wave groups to the uncertainty in H_s measurements by altimeters, with a particular focus on extreme extra-tropical storms. We take advantage of the low orbit altitude of the China-France Ocean Satellite (CFOSAT), and the low noise level of the nadir beam of the SWIM instrument. Our estimate of wave group effects uses directional wave spectra measured by off-nadir beams on SWIM and signal processing theory that gives statistical properties of the wave envelope, and thus the local wave heights, from the shape of the wave spectrum. We find that the standard deviation of H_s associated to wave groups is a function of satellite altitude, wave height and spectral bandwidth. For CFOSAT these fluctuations generally account for about 25% of the variance measured over a 80 km distance. This fraction is largest in storms and in the presence of long swells. When the estimated effect of wave groups is subtracted from the measured H_s variance, the remaining variability is higher in regions of strong currents.

Plain Language Summary

Satellite altimeters routinely provide measurements of the height of ocean waves, and improved instruments or processing techniques have led to more precise and detailed measurements. Here we use a combination of simulations and data from the China France Ocean satellite (CFOSAT) to interpret the small scale fluctuations in wave height measurements as the effect of wave "groups" which are fluctuations of the heights of consecutive waves associated to random waves. Due to spatial averaging within the radar footprint, we find that the fluctuations of significant wave heights (H_s) associated to wave group are a function of satellite altitude, wave height and other properties of the ocean waves. For CFOSAT, wave groups give a standard deviation of H_s that is of the order of 3 to 5% of H_s, typically half of the measured standard deviation of H_s.

1 Introduction

Wind-waves impact all activities at sea, air-sea interactions and remote sensing, and there is a general need for obtaining more accurate and higher resolution information about the sea state. Today, satellite radar altimetry is the most extensive source of measurements with a global coverage, providing routine estimates of the significant wave height H_s (Ardhuin et al., 2019). As these data are getting used for a wide range of applications, it is important to understand what can be measured with altimeters, at what scale and with what uncertainty.

The scale of the measurement was particularly discussed by Chelton et al. (1989), who introduced the concept of *oceanographic footprint* which contains the sea surface points that contribute to the measurement of sea level and wave height. This footprint is a disc of radius

$$r_C = \sqrt{\frac{2hH_s + 2\delta_R}{1 + h/R_E}} \tag{1}$$

where h is the satellite altitude, R_E is the Earth radius, H_s is the wave height and the range resolution $\delta_R = c/(2B)$ is defined by the radar bandwidth B and the speed of light c. We note that all Ku-band altimeters have used $B = 320$ MHz giving $\delta_R = 0.47$ m, and $B = 500$ MHz on SARAL-AltiKa gives $\delta_R = 0.32$ m, so that r_C is always larger than 1 km. Because low Earth orbit satellites fly over the ocean at a speed around 7 km/s, averaging altimeter data over 0.05 s corresponds to a spatial average over 350 m and thus does not change much the effective footprint of the measurement.

The apparent noise in such data is generally attributed to the uncertainty of the measurement, and has led users of altimetry data to take longer averages of H_s, typically 1 to 10 s, corresponding to a distance that spans 7 to 70 km. While it effectively reduces noise, such averaging also blurs potentially interesting features, in particular the peaks of storms, coastal gradients (Passaro et al., 2021), and the signature of surface currents (Quilfen & Chapron, 2019). Away from surface current gradients and coastlines, sea states are uniform over scales of the order of 70 km (Tournadre, 1993). Still, within these scales, the random nature of the wave field is another source of expected geophysical variability. Theoretical analysis, in situ time series and airborne remote sensing show that small scale variations in H_s contain a signature of wave groups that can be estimated from the wave spectrum (Arhan & Ezraty, 1978; Tayfun & Lo, 1989), and is the result of the linear superposition of many independent wave trains coming from different di-

rections. Wave groups have typical time scales of a few tens of seconds to a few minutes, that translate to spatial patterns at scales of a few kilometers, hence around the possible resolution limit of altimeters, of the order of r_C. At larger scales, non-linear wave-wave interactions should contribute to fluctuations at scales 10 to 20 minutes, with spatial scales around 10 km, that should be important for wave growth (Lavrenov, 2001) and may contain information on the wave period (Badulin, 2014). Co-location of altimeter, buoy and model data with wave heights from 1 to 8 m, has been used to estimate a typical uncertainty of 1 s averaged altimeter data around 7% for $H_s > 2$ m (Dodet et al., 2022). Understanding what makes up this uncertainty will help extrapolate uncertainties to higher values of H_s, providing a better understanding of the climatology of sea state extremes.

In the present paper we focus our analysis on the fluctuations of H_s associated to wave groups and its contribution to Delay-only altimeters that provide the existing reference time series for wave climate analysis (Young et al., 2011; Dodet et al., 2020). The main question that we wish to answer is: how much wave groups contribute to the variability in H_s measurements? For this we take advantage of the unique opportunity provided by the SWIM instrument onboard the China-France Ocean Satellite (CFOSAT). SWIM provides both directional wave spectra from which we compute the spectrum of the wave envelope that contains wave groups, and along-track nadir altimetry. Our analysis uses SWIM data over the globe for two full years 2020 and 2021.

We start with two illustrative and contrasting examples in section 2, before providing results for the globe in section 3. Discussions and conclusion follow in section 4. A side question that we had to address is: how does an altimeter measure H_s over a realistic surface that contains local perturbations associated with wave groups? For this we used a very simplified simulated altimeter with numerical results shown in section 2 and an analytical derivation in Appendix A. Those results suggest that altimeters report a particular kind of average H_s over an radius that is close to $r_C/2$. When using a least-square fit to radar waveforms, estimated H_s give a spurious amplification of true H_s perturbations located at a distance around $r_C/4$ from nadir, and are blind to perturbations located right at the nadir.

2 One particular storm and a theory of wave groups

As described in Hauser et al. (2017, 2021), the instrument SWIM is a Ku-band wave scatterometer that illuminates successively 6 incidence angles (0°,2°,4°,6°,8° and 10°). The nadir beam (0°) works as all previous Poseidon radar altimeters and provides an estimate of H_s every 0.22 s, using an average over 0.055 s. As a result, the nadir beam data is expected to be similar to data from previous Ku-band altimeters, such as Poseidon-3B on Jason-3, with the specific difference given by a lower data rate (5 Hz instead of 20 Hz for the native estimates of H_s) and a different measurement geometry associated to a rather low orbit. In principle, the low orbit altitude $h = 519$ km of CFOSAT make it possible to resolve smaller scale variations of H_s as r_C is reduced by a factor 1.4 compared to the Jason satellites that orbit at 1340 km altitude. The low noise level of the satellite and specific processing of the SWIM instrument also contribute to its capability to resolve smaller scales (Tourain et al., 2021).

The off-nadir beams use the concept of the wave spectrometer (Jackson et al., 1985) based on a real-aperture radar and the normalized radar cross-section (NRCS) sensitivity to local surface slope at near-nadir incidences, providing estimates of the directional wave spectra (with a 180° ambiguity in direction). The CNES mission center (or CFOSAT Wind and Waves Intrument Center - CWWIC) provides Level 2 products both for the nadir beam and the off-nadir beams 6° to 10°. The off-nadir L2-CWWIC products consist of 2D wave spectra provided in 12 directions from 0 to 180° and in 32 wavenumbers which are constructed from overlapping of antenna scans over 180° (on each side of the track) over boxes of about 70 km by 90 km. In order to allow comparison, the nadir product is resampled by averaging values of Hs over the box size, its variation at this scale is quantified by taking its standard deviation over the same distance, std(H_s). We will particularly investigate this quantity in the present paper. In practice we also used the homogeneously reprocessed L2P product provided by the Copernicus Marine Environment Monitoring System (CMEMS), in particular we used the quality flags specific to that product.

The Ifremer Waves and Wind Operational Center (IWWOC) is in charge of developing and testing different processing and provides an alternative Level 2 products for off-nadir beams. These products are referred to as L2S products and consist of 1D wave modulation spectra, one for each measurement azimuth. Whereas the L2-CWWIC prod-

uct uses the nadir H_s to rescale the spectrum, the L2S product is based on a theoretical modulation transfer function to transform the NRCS spectra into surface elevation spectra (Jackson et al., 1985). Also the L2-CWWIC product uses a very conservative maximum wavelength of 500 m in order to avoid amplifying noise, where the L2S product does not use such a fixed value for the maximum wavelength. As a result, L2S spectra may capture the very long waves produced in the most severe storms. In our work we have recombined the L2S product in the same "boxes" as the L2 product and rescaled the energy in the resulting spectrum to correspond to the average wave height in that box. This rescaling is particularly motivated by our investigation of wave properties along the nadir track, and it corrects a bias of the order or 14% for the total energy of the spectrum. Alternative data processings are discussed in section 4.

2.1 Wave height variability in Storm Dennis

On February 14^{th} 2020, the European windstorm Dennis, which became one of the most intense extratropical cyclones ever recorded, underwent through its explosive intensification in the middle of the North Atlantic. Around 9:10 UTC that same day, Dennis was sampled by CFOSAT, with altimeter recorded H_s values up to 19.7 m for the native (5 Hz) sampling, and 17.9 m for the 1 Hz sampling (averaging over 1 second). Fig. 1.a shows a model snapshot of H_s in the north Atlantic and the corresponding descending track of CFOSAT, while Fig. 1.b shows the altimeter wave height H_s values for the three different samplings : native (4.5 Hz), 1 Hz and box averaged.

On the periphery of the storm, where the average H_s is around 10 m, we were struck by the factor two difference in std(Hs). Because this difference is not localized but spans more than 420 km (1 minute of data), we hypothesize that the spatial variability in winds and currents forcing, that are known to cause variability in H_s (Abdalla & Cavaleri, 2002; Ardhuin et al., 2017) may not play a dominant role in this difference. In particular, regions of high current variability are usually much more localized (Quilfen & Chapron, 2019). Our working hypothesis is that this variability of H_s may be dominated by fluctuations in wave heights associated to wave groups. These fluctuations have different magnitudes and spatial scales which can be estimated from the directional wave spectrum. Hence CFOSAT is a unique instrument for studying this effect as we have both H_s variability along the satellite track and directional wave spectra. In the following, we illustrate the expected signature of wave groups for the two sea state conditions that cor-

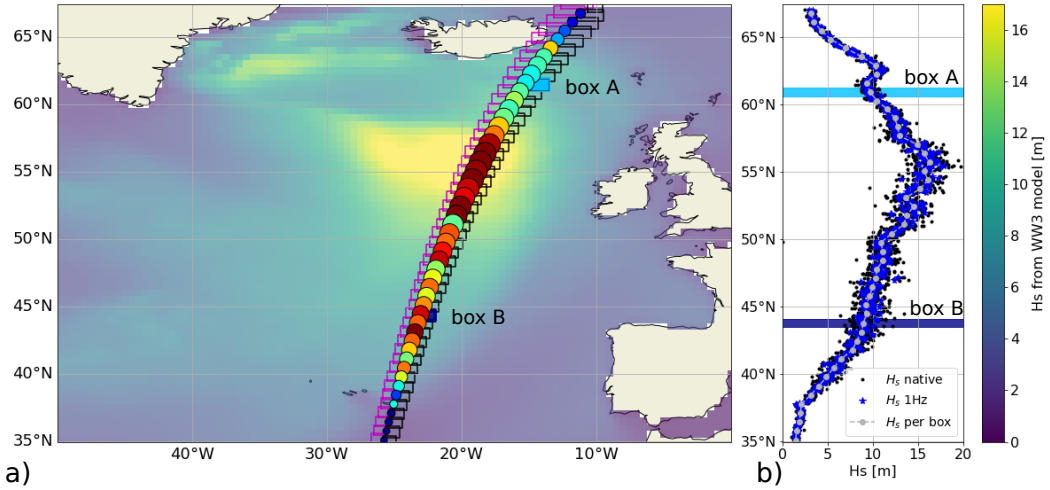

Figure 1. a) Map of wave heights in the North Atlantic at 09:00 on 14 February 2020, as provided by the model hindcast of (Alday et al., 2021), overlaid with circles located at the center of SWIM box estimates for the L2-CWWIC wave spectra. Circles are sized by the L2-CWWIC H_s estimate and color corresponds to std(Hs); b) corresponding measured H_s values as a function of latitude (y-axis) : black small dots represent native measurements at 4.5 Hz, blue stars represent the 1 Hz averaged and grey circles represent the H_s averaged over a box. Two boxes are selected for the case study: box A - highlighted in light blue - is at 62°N, and box B - in dark blue - is at 44°N.

respond to the particular SWIM boxes highlighted in light and dark blue. It is worth noting that in these two examples, the H_s values obtained from the sum of the L2S spectrum prior rescaling are around 7.5 m, which is lower than the 9 m given by the nadir beam and used in the L2 product and in this study to rescale the spectrum energy.

2.2 Variability of H_s and envelope spectrum

The patterns of individual waves vary with the shape of the wave spectrum, as illustrated in Fig. 2. A key difference between the north-side (left column) and south-side (right column) of storm Dennis is that the south-side has a longer peak wavelength around 600 m, and a more narrow spectrum, in particular in directions. The smaller width in directions gives longer wave crests while the smaller width in wavenumber magnitude gives a larger number of waves in the succession of large waves, known as groups.

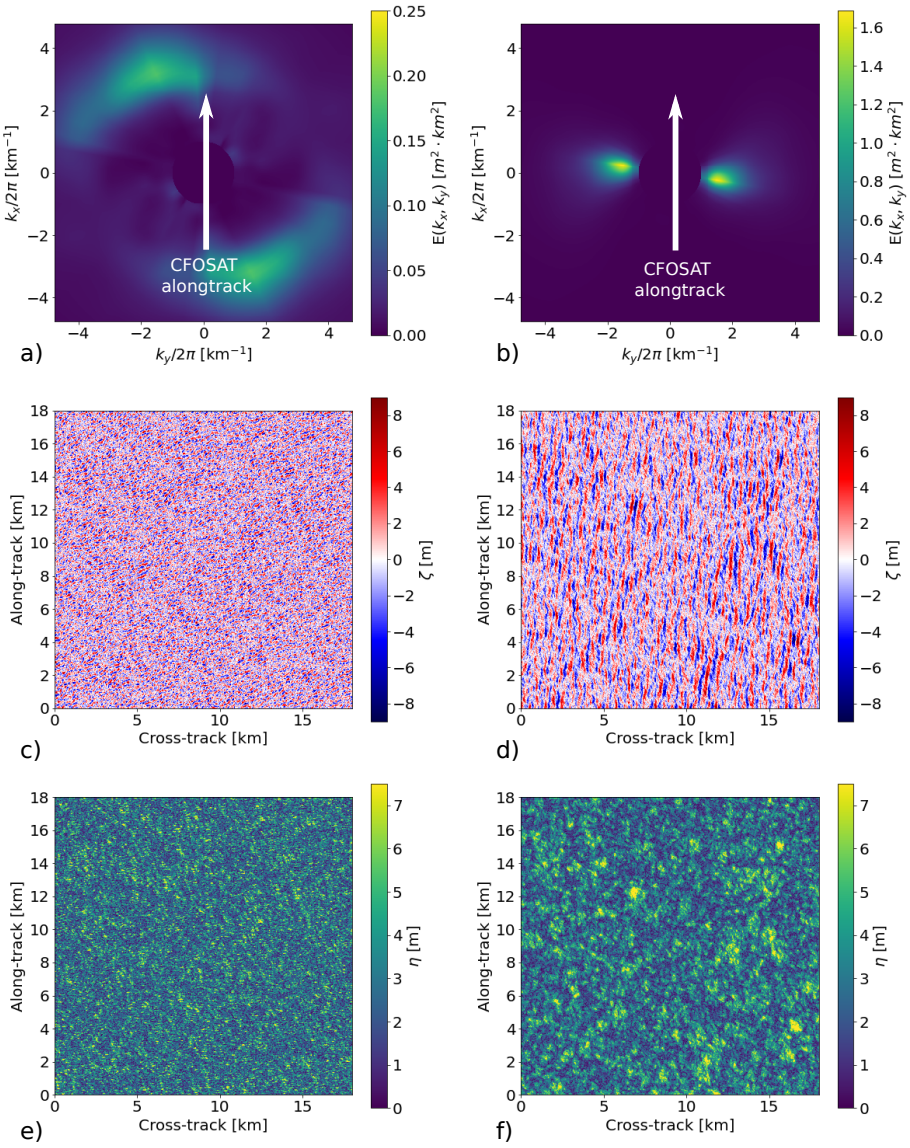

Figure 2. Left column corresponds to our chosen northern CFOSAT box, and right column to the southern box. Top line: L2S wave spectra $E(k, \theta)$ as provided by IWWOC with k the wavenumber. Middle line: simulated surface elevation maps generated from the wave spectra using random phases, bottom line: envelope of the surface elevation.

Using the envelope of the sea surface we can quantify the size of these groups (Arhan & Ezraty, 1978; Longuet-Higgins, 1984; Masson & Chandler, 1993), and their contribution to the spatial variability of H_s at all scales.

Let ζ_a be the complex surface such that $\zeta = \mathrm{Re}(\zeta_a)$ is the free surface. The envelope η of the signal is defined by $\eta = |\zeta_a|$. This defines a local amplitude of the sig-

nal, that does not contain the small scale crest-to-trough (positive to negative) variations of the original surface. Variations of the envelope contain scales much larger than the wavelengths, including scales that are comparable to, or larger than the footprint of a satellite altimeter. Hence wave groups may contribute to the fluctuations of H_s recorded by the nadir beam of SWIM, as indicated on Fig. 1.b. We will now attempt to quantify that contribution.

We thus define a local H_s as 4 times the standard deviation of the sea surface over a distance r_a. Using the Gaussian approximation of the distribution of sea surface elevations leads to an envelope following a Rayleigh distribution of parameter $H_s/4$, thus the mean of the envelope is $H_s\sqrt{\pi}/(4\sqrt{2})$. By extension,$4\sqrt{2/\pi}$ times an average of the envelope over the spatial scale r_a is equal to our local H_s.

Therefore we can write,

$$H_{s,r_a}(x,y) = 4\sqrt{\frac{2}{\pi}}(\eta \otimes g_{r_a})(x,y) \tag{2}$$

where $\otimes$ is the convolution operator and g_{r_a} is a filtering kernel of radius r_a.

In order to understand how much wave groups may contribute to H_s fluctuations in satellite data, we have to address two questions: First, what are the scales affected by wave groups? and second, what are the scales of the H_s variation that are resolved by satellite altimeters?

One simple way to quantify the different scales present in the envelope is to compute its spectrum. The most simple theoretical result comes directly from the theory of Fourier transforms that gives the spectrum of a product of functions as the convolution of the Fourier transforms. In our case, the envelope squared is the product of the elevation by its complex conjugate, and this is true for spectra in one or two dimensions. For waves in one dimension with wavenumber k, the spectrum of the envelope squared $\Psi_2(k)$ is the convolution of the spectrum of the one-sided surface elevation spectrum $E(k)$ by itself,

$$\Psi_2(k) = 8\int_0^\infty E(u)E(u+k)\mathrm{d}u, \tag{3}$$

and we note that $\Psi_2(k)$ is also single-sided.

In practice people have rather studied the variations of H_s and not that of H_s^2. Although the details of the theory are more complex, the important result is that, for low frequencies, the spectrum of the envelope $\Psi(k)$ has the same shape as the spectrum of

the envelope squared $\Psi_2(k)$ (Rice, 1944). More specifically, Tayfun and Lo (1989) have showed that a good approximation for the spectrum of the envelope is given by

$$\Psi(k) = \frac{8-2\pi}{H_s^2}\Psi_2(k) \tag{4}$$

This same result is valid for spectra in two dimensions. We now consider the double-sided wave spectrum $E(k_x, k_y)$, defined for (k_x, k_y) in the entire wavenumber plane and centrally symmetric, the region of the envelope spectrum for $k \ll k_p$ is identical to

$$\Psi_2(k_x, k_y) = 8\int_{-\infty}^{\infty}\int_{-\infty}^{\infty} E(u,v)E(u+k_x, v+k_y)\mathrm{d}u\mathrm{d}v, \tag{5}$$

in which Ψ_2 is also double-sided.

From eq. (2), the spectrum of $H_s^{r_a}$ is

$$\Psi_{H_s,r_a}(k_x, k_y) = 4\sqrt{\frac{2}{\pi}}\cdot\frac{8-2\pi}{H_s^2}\cdot\Psi_2(k_x,k_y)G_{r_a}(k_x,k_y)$$

with G_{r_a} the square of the Fourier transform of the altimeter filtering kernel g_{r_a}.

We can thus estimate the standard deviation of H_{s,r_a} in altimeter measurements along the satellite track for segment of length L_1, by integrating the expected variance for $k_x > k_1$, with $k_1 = 2\pi/L_1$ and the x-axis taken in the along-track direction.

The group-induced variation of H_s is thus equal to

$$\mathrm{var}(H_{s,r_a}, L_1)_{\mathrm{wg}} = 16\sqrt{\frac{2}{\pi}}\frac{4-\pi}{H_s^2}\int_{-\infty}^{\infty}\int_{k_1}^{\infty}\Psi_2(k_x,k_y)\cdot G_{r_a}(k_x,k_y)\mathrm{d}k_x\mathrm{d}k_y. \tag{6}$$

We now need to estimate r_a and G_{r_a} for the comparison with altimeter data.

2.3 Altimeter measurements over varying wave heights

Satellite altimeters transmit radar pulses that are reflected from the sea surface, and they measure the backscattered power as a function of time. This variation of received power as a function of time is known as the waveform, and it is typically averaged over a few hundred pulses spanning about 0.05 s in order to reduce the speckle noise (Quartly et al., 2001). Time can be transformed to distance from the satellite, or range R, and the waveform effectively contains information on the statistical distribution of ranges around the mean satellite altitude h. As shown by Brown (1977), assuming a uniform ocean reflectivity the waveform is a area-weighted histogram of the ranges. Over a flat sea surface, this histogram is a Heaviside function because the part of the ocean

surface with ranges between R and $R+\delta_R$ is an annulus of radius $r = \sqrt{R^2 - h^2}$ centered on the nadir point, with an area $2\pi R\delta_R$ that is almost constant as long as $R \approx h$. In the presence of waves, a negative surface elevation $z = \zeta$ will shift the range to a higher value, sharing the range position of sea surface elements located at $z = 0$ and further away from nadir. Given the very small incidence angles, the change in range is $\Delta_R = -\zeta$. For a Gaussian distribution of ζ with standard deviation $\sigma_H = H_s/4$, the presence of waves gives a smoothing of the histogram. Here we use the most simple theoretical shape of the waveforms that is obtained in the limit of a very broad radar antenna pattern (Brown, 1977),

$$w_B(R, \sigma_H) = \frac{1}{2}\left[1 + \mathrm{erf}\left(\frac{R-h}{\sqrt{2}\sigma_H}\right)\right]. \tag{7}$$

When "retracking" altimeter data, eq. (7) is inverted, and H_s is estimated to be 4 times the σ_H of the theoretical waveform that best fits the data. In practice the theoretical waveform also includes effects of the antenna patterns, possible mispointing, and different fitting methods have been developed to reduce the effect of noise or spurious echoes in the measured waveform (Rodriguez, 1988; Passaro et al., 2014; Tourain et al., 2021). Another important assumption needed to obtain the Brown waveform is that the sea state is homogeneous within the footprint. We thus have to discuss what sets the scale of the footprint, or more precisely where are the points on the sea surface that give the distinctive shape of the waveform and allow the fit to distinguish different wave heights.

Compared to a flat sea surface, the elevation ζ at a distance r from the nadir point will change the range R of the surface point and make it look as if it was located at a different distance $r+\delta_r$, so that points from different locations on the sea surface will map to the same range R. This is the same "range bunching" or "overlay" or "surfboard effect" that is common to all radar systems (Peral et al., 2015). Following Chelton et al. (1989) we can estimate the apparent horizontal displacement. For a satellite altitude h and using $\zeta \ll R$, the calculation for a flat mean sea surface gives

$$\delta_r \simeq \sqrt{r^2 - 2h\zeta} - r. \tag{8}$$

For a spherical Earth of radius R_E, ζ should be replaced by $\zeta/(1 + h/R_E)$.

In the particular case where $\zeta = -H_s$ and $r = 0$, δ_r is the radius r_C of oceanographic footprint as defined by Chelton et al. (1989), and given by eq. (1), when the range resolution δ_R is neglected compared to H_s. For $H_s = 10$ m, and $h = 519$ km, this gives $r_C = 3.3$ km.

We may give the following interpretation of r_C. At points located at r_C from nadir (i. e. at the edge of the "Chelton footprint") there is only a 0.003% probability that $\zeta > H_s$ and that these points contribute to the waveform at ranges $R < h$, i.e. in the first half of the rising part of the waveform. In practice, points outside of the footprint (located at $r > r - C$) do not contribute to the middle part of the waveform that most contributes to the fit of σ_H and the estimation of H_s.

If wave heights vary as a function of distance to nadir, then the waveform does not follow exactly the Brown form, as detailed in Appendix A. As different regions of the waveform contain different regions of the sea surface, one could imagine fitting different parts of the waveform to measure variations in H_s as a function of distance from nadir. The theoretical limit to this capability is the blurring due to range bunching over a distance of the order $r_C/2$. Speckle noise is another limiting factor, and probably the main one in practice for small wave heights.

Based on the analysis in Appendix A we expect that variations of H_s at scales much smaller than $r_C/4$ will be smoothed out in altimeter data, whereas variations at scales much larger than $r_C/2$ have no effect on the waveform that will follow the Brown shape for the local wave height. For our analysis of CFOSAT data we will define an "effective altimeter radius" r_a such that the variance of H_s associated to the random fluctuations of the envelope filtered with a Gaussian filter of standard deviation r_a, is the same as that produced by an altimeter. The actual shape of the "altimeter filter" is discussed in Appendix A and varies in its details with the details of the retracking algorithm.

2.4 Estimation of the equivalent r_a scale for an idealized altimeter

We have simulated the sampling of our simulated sea surface by a highly simplified altimeter. We thus neglect radar noise, speckle and variations in ocean backscatter, and compute simulated waveforms as histograms of the number of discrete pixels as a function of range R discretized with the same resolution $\delta_R = 0.47$ m used in actual SWIM data. The histogram is computed for a finite region of size r_C by r_C centered at the nadir point. The value of H_s for each simulated histogram is taken to be the H_s of the theoretical waveform given by eq. (7) that best fits the simulation for R varying from $h - H_s$ to $h + H_s$, using least square fit. As detailed in Appendix A, even this simplified altimeter makes a much more complex measurement than a simple Gaussian smooth-

ing of the H_s field. We briefly tested that more realistic waveforms and different fitting procedures yield some quantitative differences.

Taking the simulated sea surface from Fig. 2, we compare a map of simulated altimeter data in Fig. 3 with maps of local wave heights, smoothed on different scales.

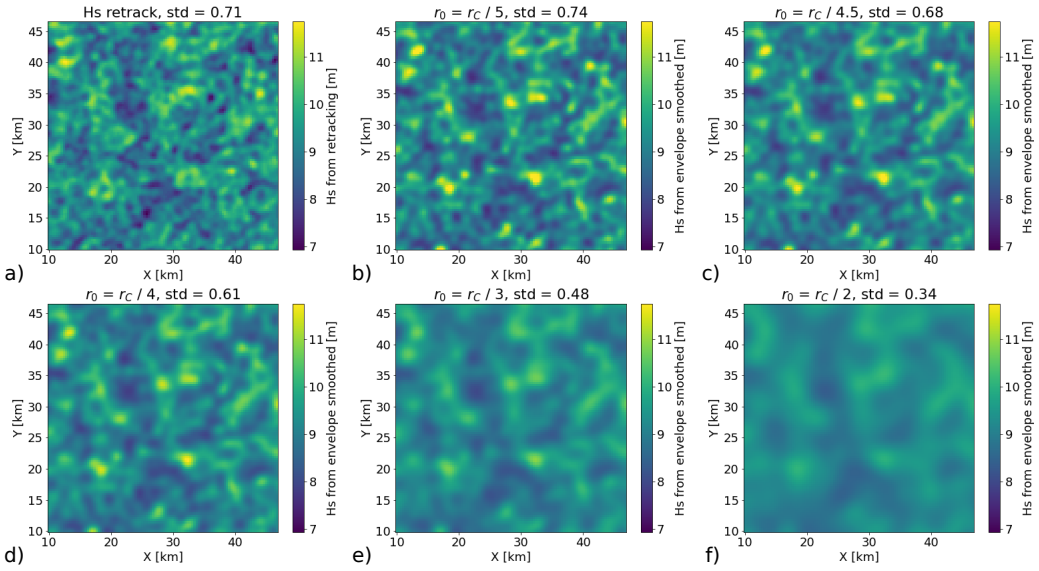

Figure 3. Maps of wave heights obtained by either simulating altimeter processing (top left) or smoothing the envelope with a Gaussian filter of standard deviation r_0 varied from $r_C/5$ to $r_C/2$. In this example, $r_C = 3063$ m thus r_0 values are respectively 613, 681, 766, 1021, and 1531 m. In practice the smoothing is applied in a finite box of size $4r_C$ by $4r_C$.

As expected, the large scales of the envelope, those that persist in the bottom-right panel of Fig. 3, match the large scales of the simulated altimeter data. From a quantitative point of view, the standard deviation of the simulated altimeter data, here 0.63 m, is of the same order as the standard deviation of actual SWIM measurements over the same SWIM box. We also note that this value is very close to that obtained for a filtering of the envelope between a scale $r_a = r_C/5$ and $r_a = r_C/4.5$.

Looking at Fig. 3.a) it is clear that the map of retracked H_s contains much smaller features than the envelope smoothed with $r_a = r_C/4.5$. All of these are spurious amplification of envelope perturbations that happen to be at the right distance from nadir, around $r_C/2$, as explained in Appendix A. As a result, maxima of H_s given by the altimeter are not located at the true H_s maxima but slightly displaced by a distance of

the order of $r_C/2$. A striking example in Fig. 3 is the region of waves higher than 11 m around $x = 32$ km, $y = 22$ km. The altimeter gives a local minimum where the true wave height is maximum, and a round halo of maxima surrounding that point. Conversely a ring-shaped maximum in the envelope, such as around $x = 39$ km, $y = 23$ km, gives a local maximum in the simulated altimeter data. We expect that sensitivity may vary with the actual retracking procedure, and this discussion is beyond the scope of the present paper.

Even though the patterns do not exactly coincide, we will now assume that the sampling of the sea surface by the altimeter is equivalent, in terms of variability of H_s to filtering the envelope with a Gaussian of standard deviation $r_a = r_C/4.5$.

2.5 Generic sea states, envelopes and H_s variability

Based on our analysis, we expect that SWIM measurements of H_s are contaminated by wave group structures at scales of the order of a few kilometers, following the variation of r_C with wave height and satellite altitude. As illustrated by the two examples with different spectral width, we note that for the same wave height, a wider spectrum leads to smaller scales of wave groups, part of which scales are smoothed away by the altimeter footprint and therefore not resolved. For a narrower spectrum, wave groups have larger scales and amplitudes and a larger contribution to the variability of wave heights estimated by an altimeter.

For a simple quantitative analysis we may consider the more simple case of waves propagating in only one direction, with a sea surface ζ distributed with the normal law $\mathcal{N}(0, \sigma_H = H_s/4)$ with a one-sided Gaussian spectrum (defined for $k > 0$)

$$E(k) = \frac{H_s^2}{16\sigma_k\sqrt{2\pi}} \mathrm{e}^{-(k-k_p)^2/(2\sigma_k^2)}. \tag{9}$$

The spectrum of the envelope is also Gaussian and the H_s PSD writes (for a one-sided spectrum),

$$\Psi_{H_s}(k) = \frac{4-\pi}{\pi\sqrt{\pi}\sigma_k} \cdot H_s^2 \mathrm{e}^{-k^2/(4\sigma_k^2)}. \tag{10}$$

Wave groups contain wavelengths larger than π/σ_k, with a constant spectral density near $k = 0$. Around $k = 0$, the value of the Hs spectrum is $0.15H_s^2/\sigma_k$ m^2/(rad/m).

Fig. 4 presents one dimensional wave spectra - in solid lines - of two typical sea states with same $H_s = 3.11$ m and their associated H_s spectra $\Psi_{H_s}(k)$- in dashed lines. The light blue spectrum is a JONSWAP spectrum (Hasselmann et al., 1973) with a peak period of 8 s and a peak enhancement factor $\gamma = 3.3$ that represents a moderate wind-sea. The dark blue spectrum is a narrow Gaussian spectrum with a peak period of 14 s and $\sigma_k = 0.002$ rad/m, typical of swell conditions in the open ocean. The altimeter smoothing function $G_{r_a} = \exp(-k^2 r_a^2)$ allows to define a cut-off wave number $k_a = \sqrt{\pi}/(2r_a)$. As shown in Fig. 4 the wavelengths in altimeter-filtered envelopes, larger than the associated wavelength cut-off $2\pi/k_a$ (in black dash-dotted line), are large compared to the shortest wavelengths contained in the wave groups (of order $\pi\sqrt{2}/\sigma_k$ and represented by the dark and light blue vertical dash-dotted lines).

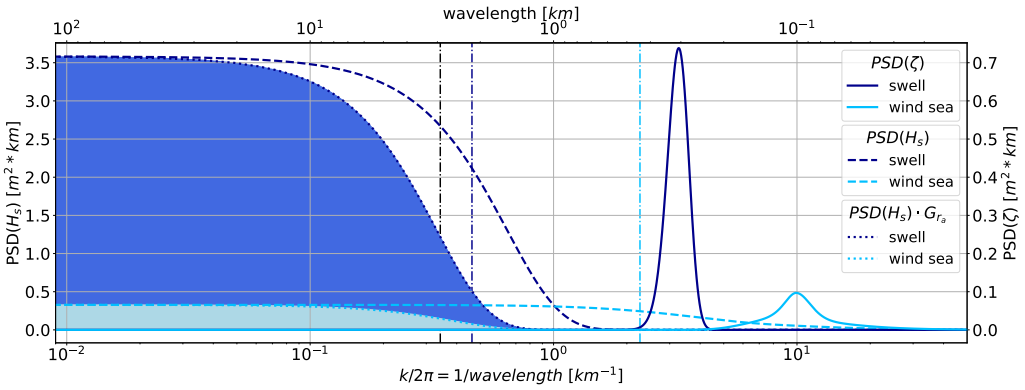

Figure 4. Example of two wave spectra - solid lines - in one dimension and the corresponding spectra of H_s - dashed lines -, for typical swell conditions in the open ocean in dark blue, and typical moderate wind windsea in light blue. Because the fluctuations of H_s are filtered by the altimeter with the function $G_{r_a}(k)$ - dotted lines -, the actual measured variance of H_s is the shaded area, in light blue for the windsea and dark blue for the swell. The vertical black line is the equivalent altimeter cut-off wavenumber at $k = k_a$, whereas the vertical dark and light blue lines represents the width of the H_s spectra.

Applying the one dimension version of eq. (6) gives the variance of altimeter-estimated H_s as the shaded areas in Fig. 4. For a Gaussian spectrum, in cases where the altimeter filter scale is large enough not to be concerned about the shortest scales, this area is approximately k_a times $\Psi_{H_s}(k = 0)$ the H_s PSD level at $k = 0$. This gives a stan-

dard deviation of H_s of the order of $0.39\sqrt{k_a/\sigma_k}H_s$, which is 0.40 H_s for the one-dimensional swell example of Fig. 4.

For a generic one-dimensional wave spectrum $E(k)$, the width σ_k should be replaced by the the bandwidth $B_k/(2\sqrt{\pi})$, with B_k defined like the usual frequency bandwidth (Saulnier et al., 2011),

$$B_k = \frac{H_s^4}{256\int_0^\infty E^2(k)\mathrm{d}k}. \tag{11}$$

For a JONSWAP spectrum, $B_k = 1.3k_p$ and the standard deviation of H_s for the wind sea case above is $0.1H_s$.

For waves in two dimensions, the directional spread of the energy leads to a further reduction of the variability of H_s. Using the spectrum of the envelope at $k = 0$ we may define a two-dimensional spectral bandwidth B_{kk}

$$B_{kk}^2 = \frac{H_s^4}{256\Psi_2(k_x=0,k_y=0)/8} = \frac{H_s^4}{256\int_{-\infty}^{\infty}\int_{-\infty}^{\infty}E^2(k_x,k_y)\mathrm{d}k_x\mathrm{d}k_y}. \tag{12}$$

When r_a is large enough we can consider that Ψ is constant for $k < 1/r_a$, which gives

$$\mathrm{std}(H_s)_{\mathrm{wg}} \simeq \frac{\sqrt{4-\pi}}{B_{kk}}H_s\sqrt{2/r_a^2 - 4k_1/(\sqrt{\pi}r_a)}. \tag{13}$$

2.6 Summary of methodology

In the previous subsections, various considerations have been made. Here, we summarize them to give a flow chart for estimating the part of the variability due to wave groups $\mathrm{std}(H_s)_{\mathrm{wg}}$ from CFOSAT products.

1. Assemble the 1-dimensional IWWOC-L2S spectra for each azimuth to obtain an equivalent CWWIC-L2 spectrum, make it double-sided $E_{2S}(k,\theta)$ and rescale it with H_s from nadir measurement,
2. Interpolate $E_{2S}(k,\theta)$ over a regular (k_x,k_y) grid, with k_x the along track direction, to obtain $E(k_x,k_y)$,
3. Compute the spectrum of the envelope squared $\Psi_2(k_x,k_y)$ from the discrete correlation

$$\Psi_2(k_x,k_y) = 8\cdot\sum_{k'_x}\sum_{k'_y}\left[E(k'_x,k'_y),E(k'_x+k_x,k'_y+k_y)\right]\mathrm{d}k'_x\mathrm{d}k'_y \qquad \text{(Step 3)}$$

4. Transform to a PSD of H_s,

$$\Psi_{H_s}(k_x,k_y) = 4\sqrt{\frac{2}{\pi}}\cdot\frac{8-2\pi}{H_s^2}\cdot\Psi_2(k_x,k_y) \qquad \text{(Step 4)}$$

where H_s is computed as $4 \cdot \sqrt{E}$, with $E = \iint_{\mathbb{R}^2} E(k_x, k_y) \mathrm{d}k_x \mathrm{d}k_y$.

5. Define a G_{r_a} with $r_a = r_C/4.5$ as

$$G_{r_a}(k_x, k_y) = |\mathcal{F}(g_{r_a})|^2 = \mathrm{e}^{-(k_x^2+k_y^2)\cdot r_a^2} \quad \text{(Step 5)}$$

6. Apply the filter to Ψ_{H_s} to obtain the PSD of altimeter H_s estimate,

$$\Psi_{H_s,r_a} = \Psi_{H_s} \cdot G_{r_a} \quad \text{(Step 6)}$$

7. Integrate $\Psi_{H_s,r_a}(k_x, k_y)$ over $\mathbb{R}$ for k_y and $\mathbb{R}_{\setminus[-k_1,k_1]}$ and take the square-root to obtain $\mathrm{std}(H_{s,r_a}, L_1)_{\mathrm{wg}}$.Because we compare our estimate to H_s variations with a SWIM L2 box size that is 80km along-track, L_1 is taken as 2×80 km,

$$\mathrm{std}(H_s)_{\mathrm{wg}} = \mathrm{std}(H_{s,r_a}, L_1)_{\mathrm{wg}} = \int_{k_y \in \mathbb{R}} \int_{k_x \in \mathbb{R}_{\setminus[-k1,k1]}} \Psi_{H_s,r_a}(k_x, k_y) \mathrm{d}k_x \mathrm{d}k_y \quad \text{(Step 7)}$$

Fig. 5 shows the results of steps 3, 6 and 7 for the two selected boxes of our case study. The top line corresponds to the Ψ_2 spectra obtained from correlation, the middle line shows the PSD of our local H_s estimate Ψ_{H_s,r_a} (note the different colour scales between the northern - A - and southern - B - boxes), whereas the bottom line shows the one sided k_x-spectra after integration along k_y, with the plain vertical line showing the integration limit over k_x.

Fig. 6 shows wave height and corresponding standard deviation, both observed and estimated from L2S spectrum, as a function of the sampling time (UTC) over storm Dennis. For the northern part of the storm, where the spectrum is broader, around box A (light blue vertical line), the standard deviation due to wave groups is around half the measured standard deviation (i.e. wave groups represent a quarter of the measured variance). On the other hand, for the southern part, around box B (dark blue), the wave height variability is strongly dominated by wave groups - more than half the observed variance is explained by wave groups.

Alternatively we can approximate the full integral of the convolution by its value at $k = 0$ using the bandwidth B_{kk} , giving a faster estimate of the variability due to wave groups. The first two steps are the same, then

- Instead of the full convolution, compute only B_{kk} defined in eq. (12), which can be re-written as,

$$B_{kk} = \frac{\iint_{\mathbb{R}^2} E(k_x, k_y) \mathrm{d}k_x \mathrm{d}k_y}{\sqrt{\iint_{\mathbb{R}^2} E^2(k_x, k_y) \mathrm{d}k_x \mathrm{d}k_y}} \quad \text{(Step 3bis)}$$

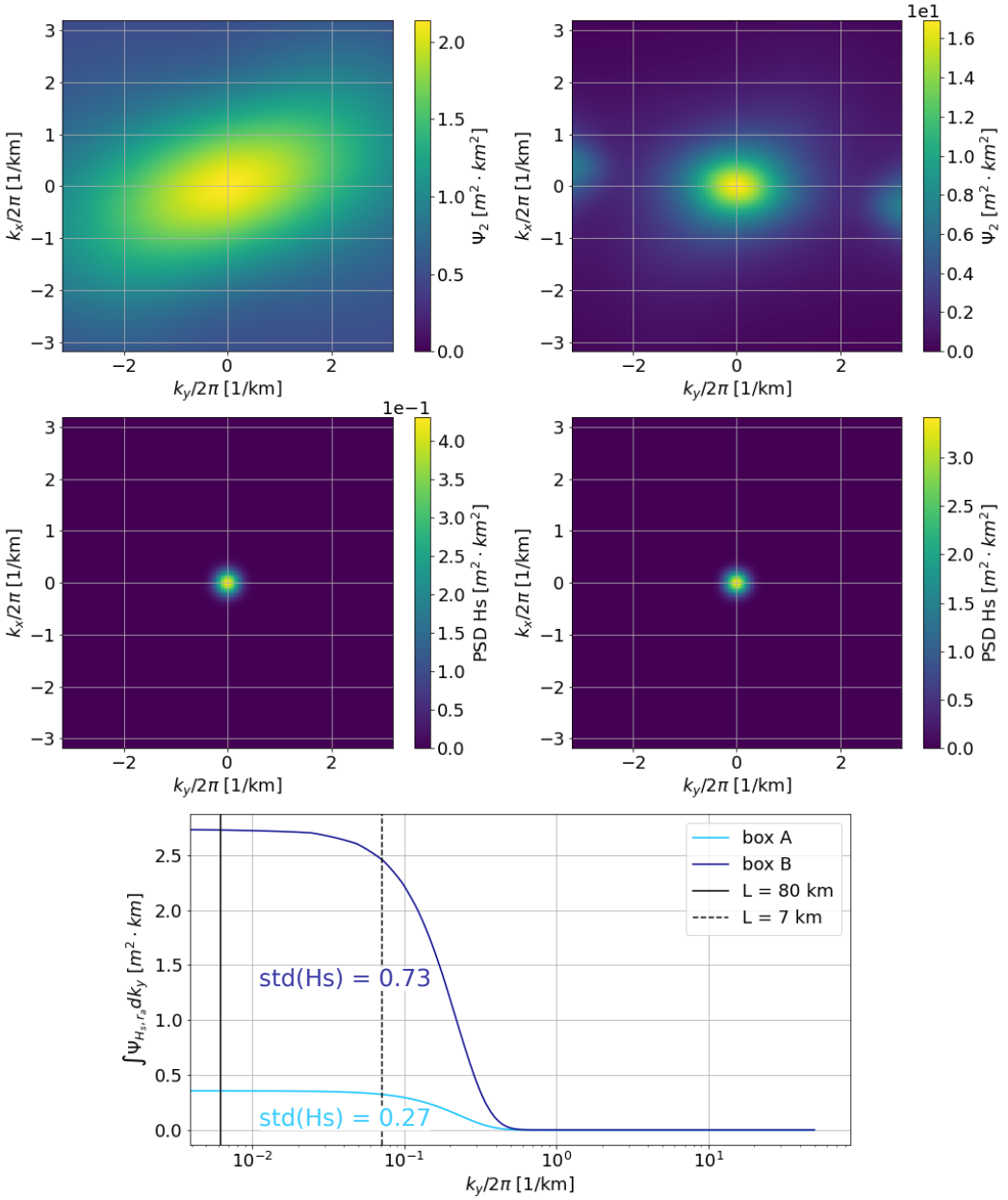

Figure 5. Left column corresponds to our chosen northern CFOSAT box, and right column to the southern box. Top line: cnvelope squared spectrum $\Psi_2(k_x, k_y)$ from convolution. Middle line: spectrum of $H_s^{r_a}$ Ψ_{H_s,r_a} (including the equivalent altimeter filtering). Bottom line: 1D along-track spectrum obtained by integrating over the cross-track axis, in light blue for the northern box and dark blue for the southern box.

- skip steps 4–6 to estimate $\mathrm{std}(H_s)_{\mathrm{wg}}$ directly using eq. (13),

$$\mathrm{std}(H_s)_{\mathrm{wg}} \simeq \frac{\sqrt{4-\pi}}{B_{kk}} H_s \sqrt{2/r_a^2 - 4k_1/(\sqrt{\pi} r_a)}. \qquad \text{(Step 7bis)}$$

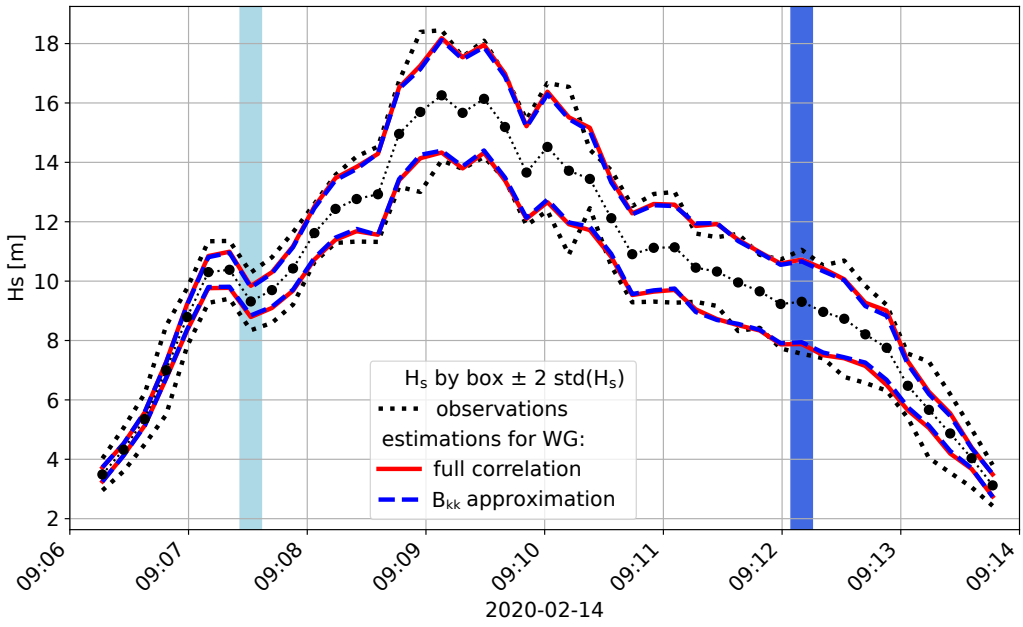

Figure 6. Values of measured H_s, averaged over boxes - black circles - , and corresponding std(Hs) - black dotted lines - ; as provided in the L2-CWWIC as a function of sampling time (UTC), for the CFOSAT track shown in Fig. 1. Estimations of std$(H_s)_{\mathrm{wg}}$ are also represented - in red and blue - using the two methods summarized at the end of section 2.

This std$(H_s)_{\mathrm{wg}}$ estimated through B_{kk} is also shown in Fig. 6. The values are only slightly overestimated compared to the full correlation calculus, therefore, B_{kk} could be a useful parameter when working with wave groups.

3 Results at the global scale

Beyond the particular case of storm Dennis, for which very large wavelength and narrow spectra lead to a dominant effect of wave groups in H_s variability, how important are wave groups in general, and how important can they be compared to other known sources of H_s variability, including winds and currents?

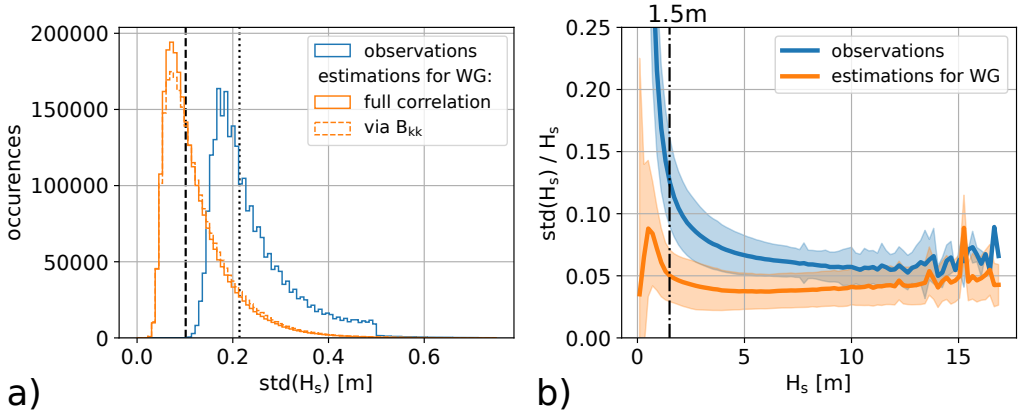

Figure 7. (a) Histograms of std(H_s) measured at nadir in blue and our estimate of wave groups contribution std$(H_s)_{\mathrm{wg}}$ in orange. (b) Mean - solid lines - and standard deviation - shaded areas - of std$(H_s)/H_s$ over H_s bins of 0.2 m, both for std(H_s) measured at nadir in blue and our estimate of wave group effects in orange.

We have thus applied the methodology presented in section 2 for storm Dennis to the full SWIM L2S archive for the years 2020 and 2021, estimating for each of the 2.4 million SWIM L2 box the expected value of std$(H_s)_{\mathrm{wg}}$ associated to wave groups as filtered by the altimeter. The distribution of these values is shown in Fig. 7.a, with a typical value around 7 cm, and maximum values around 60 cm. This variability is typically half of the measured standard deviation of H_s.

We also computed std$(H_s)_{\mathrm{wg}}$ as estimated from the bandwidth B_{kk} for the same time period, giving results that are highly correlated to the full convolution.

In practice the group-induced variability of H_s that is resolved by altimeters is strongly correlated with the mean value of H_s.

In Fig. 7.b we show the statistical distribution (mean and standard deviation) of std(H_s)/mean(H_s) as a function of H_s. For H_s below 1.5 m the altimeter estimates of

H_s are known to have the largest relative errors (Dodet et al., 2022), which is partially due to a stronger effect of speckle noise, as discussed in Appendix A.3. In that range the wave group variability is 3 times smaller than the observed variability.

Above 1.5 m, the relative variability that is expected from wave groups increases with H_s (from 3.5% to 5%), whereas the observed variability decreases from 11% to 5% between $H_s = 1.5$m and $H_s = 10$m. The share of the variability expected from wave groups dominates the observed variability for wave heights above 8 m, and probably explains the increase in observed std(H_s)/mean(H_s) for H_s above 12 m. Although there are very few data in that range, it is well known that dominant wave periods must be higher for higher wave heights (Toba, 1973), corresponding to smaller bandwidths and thus an ever increasing std$(H_s)_{\mathrm{wg}}/H_s$.

We now consider the spatial distribution of std(H_s), and in order to separate the possible effects of different sea states from the general trends associated to local average value of H_s, we have chosen to show a map of the mean value of std(H_s)/H_s. Before computing the local mean we have first removed all cases with $H_s < 1.5$ m. Fig. 8.a shows the distribution of std(H_s)/mean(H_s) and, for comparison, std$(H_s)_{\mathrm{wg}}$/mean(H_s) in Fig. 8.b.

Note that the range of values are different for both panels because the contribution of wave groups is, on average, half of the measured std(H_s). Both figures have some common patterns with a general increase from the west to the east of the ocean basins consistent with a dominance of swells in the east (Chen et al., 2002) with longer wavelengths and narrower spectra.

We may also remove the contribution of wave groups to look at the other sources of variability in H_s. As shown in Fig. 8.c, the standard deviation of H_s corrected for the effects of wave groups contains a background level of 0.1 to 0.2 m, probably associated to speckle noise and small scale wind variability, and stronger localized values up to 0.3 m. These large values are co-located with regions of strong ocean circulation mesoscale variability. These same regions match the location of strong H_s gradient in along-track 1 Hz data from Saral-Altika, Jason-2 and Cryosat-2 that have been denoised using an Empirical Mode Decomposition (EMD), by Quilfen and Chapron (2019). Here, we have applied the same EMD filtering to SWIM 5 Hz data, instead of 1 Hz in the literature, in order to decontaminate the nadir H_s from the wave group effect, giving results shown

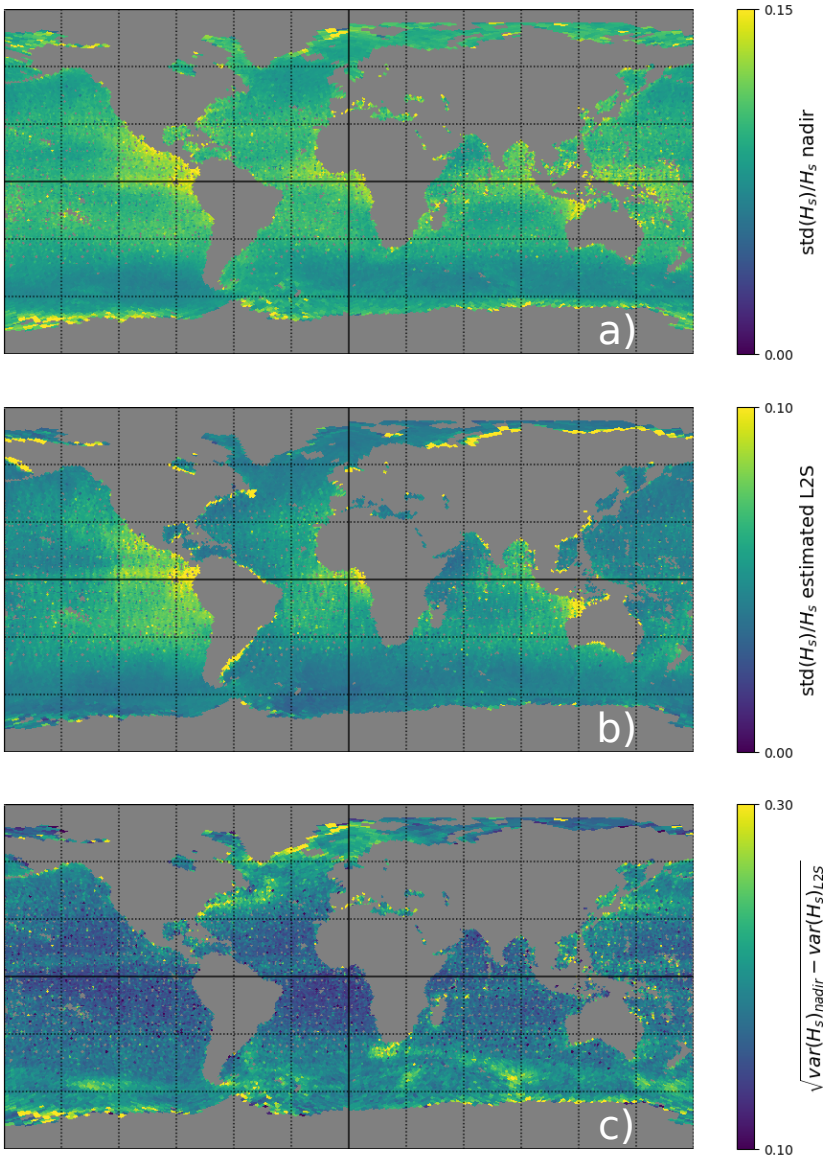

Figure 8. Map of the average of a) std(H_s)/mean(H_s) - upper panel -, b) std$(H_s)_{\mathrm{wg}}$/mean(H_s) -middle panel - and c) residual standard deviation of H_s, in meters, after removing the effect expected from wave groups - lower panel -, for the years 2020 and 2021 for all the SWIM L2-IWWOC boxes with a H_s above 1.5 m. With the wave group contribution std$(H_s)_{\mathrm{wg}}$ estimated from SWIM L2S spectra

in Fig. 9. The EMD filtered part Fig. 9.c is directly comparable to the wave group signature highlighted in Fig. 8. These maps were constructed using SWIM nadir data from SALP/CAWATAC experimental 5 Hz products available on Aviso+ that include both the raw H_s estimate and the denoised values using the EMD method. The magnitude

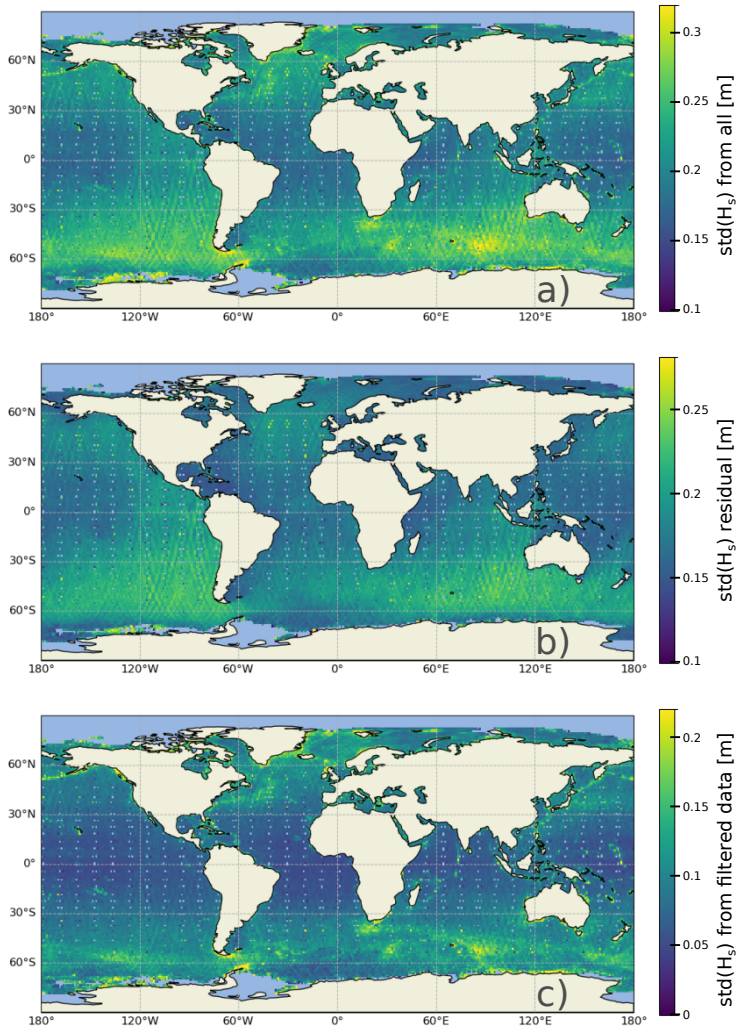

Figure 9. Maps of the average, for the year 2021, of (a) std(H_s) computed on original SWIM nadir native values (5 Hz), (b) standard deviation of the residual of H_s, defined as the difference between the original and the denoised wave height (c) std(H_s) computed on EMD filtered data.

and distribution of the expected effect of wave groups apparently corresponds to the variability that is removed by EMD denoising, without using wave spectrum information. Thus, the uncertainty variable associated to the nadir 5 Hz data in the SALP/CAWATAC products which is derived from the standard deviation of the fluctuations removed by EMD should be related to H_s and B_{kk}. As these products are available for other satellite missions for which no wave spectra are measured, further analysis may provide a more careful quantification of the estimate of wave groups effects removal.

4 Discussion

4.1 Effect of spectral shape

The accurate estimation of wave group contributions critically depends on the accuracy of the spectral shape, in particular the directional width and wavenumber width. Because of the hard wavelength cut-off in the L2 product we had chosen to work with the L2S spectra. Redoing the global analysis with the L2 product generally reduces the expected effect of wave groups.

We note that a validation of spectral width from the L2 product was performed by Le Merle et al. (2021), who found that SWIM L2 generally overestimate spectral width compared to buoy data. No such analysis has been performed for the L2S product. It would be also interesting to know how accurate could be the estimation of $\mathrm{std}(H_s)_{\mathrm{wg}}$ estimated from model spectra, for the application to other satellite mission that do not measure the wave directional spectrum.

It should also be reminded that SWIM L2 spectra combine sparse measurements over a 70 km by 80 km box, as illustrated in Fig. 10. Because the wave field has gradi-

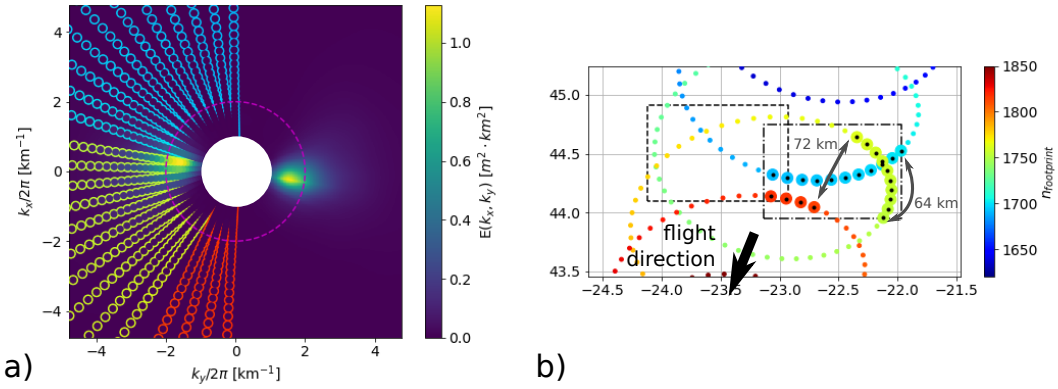

Figure 10. (a) Representation of a two-dimensional spectrum $E(k_x, k_y)$ with values given by the colorbar obtained from assembling L2 1-dimensional spectra $E(k)$ for all azimuths. The color of each circle corresponds to the index of the beam footprint in which the SWIM was making the measurement (b) Geographical layout of boxes - dashed and dash-dotted rectangles - and of centers of the beam footprints on the sea surface. the footprint diameter is about 20 km so that they actually overlap.

ents, this combination generally produces a broader spectrum than the a more local es-

timate of the wave spectrum, and this should produce a low bias in our estimate the effect of wave groups. In the example on Fig. 10 the assembly of the L2 spectrum combines data from two neighboring wave azimuths that are observed in distinct regions of the ocean separated by up to 72 km. We kept this assembly to be able to compare results from L2 and L2S data, but it would be more logical, for the case of L2S data, to assemble a spectrum with a spatial continuity of the footprints that correspond to azimuths around the spectral peaks.

4.2 Effects of satellite altitude

The particularly low orbit of CFOSAT at 519 km gives a rather small oceanic footprint that allows for wave groups to be resolved in SWIM data. If we consider the higher altitudes used by other satellite missions, 891 km for the recently launched SWOT or 1340 km for the Topex-Poseidon / Jason / Sentinel 6 series, the oceanic footprint gets bigger and wave groups are more likely to be more smoothed out. In Fig. 11, we illustrate this effect with different altitudes following the method used for Fig. 3. Namely, for the same simulated ocean surface, the wave height is estimated by a least-square fit to the simplest Brown waveform given by eq. (7). As expected, the higher the satellite the lower the variability of H_s. It is not clear that this effect of satellite altitude is noticeable in real data that are contaminated by speckle noise and that use different waveform fitting algorithms. More realistic simulations will be needed to compare the behaviour or different instruments and processing chains.

4.3 Expected effect on delay doppler altimeters

We have shown that the variability of H_s at small scale contains some geophysical information and not just random noise related to the measurement. However, the noise for Delay-only altimeters is probably dominated by the speckle noise in the waveforms (Sandwell & Smith, 2005; Quartly et al., 2019). Doppler processing of recent altimeter instruments starting with Cryosat-2 and Sentinel-3 can strongly reduce this speckle noise by forming and combining independent looks of the same sea surface (Egido et al., 2021). It will therefore be interesting to study the effect of wave groups in these measurements of wave height and sea level. Waves can also be resolved directly in the sea level estimates when data is processed at very high resolution (Altiparmaki et al., 2022; Villas Bôas et al., 2022). If the Doppler induced by orbital velocities is neglected, the delay-Doppler

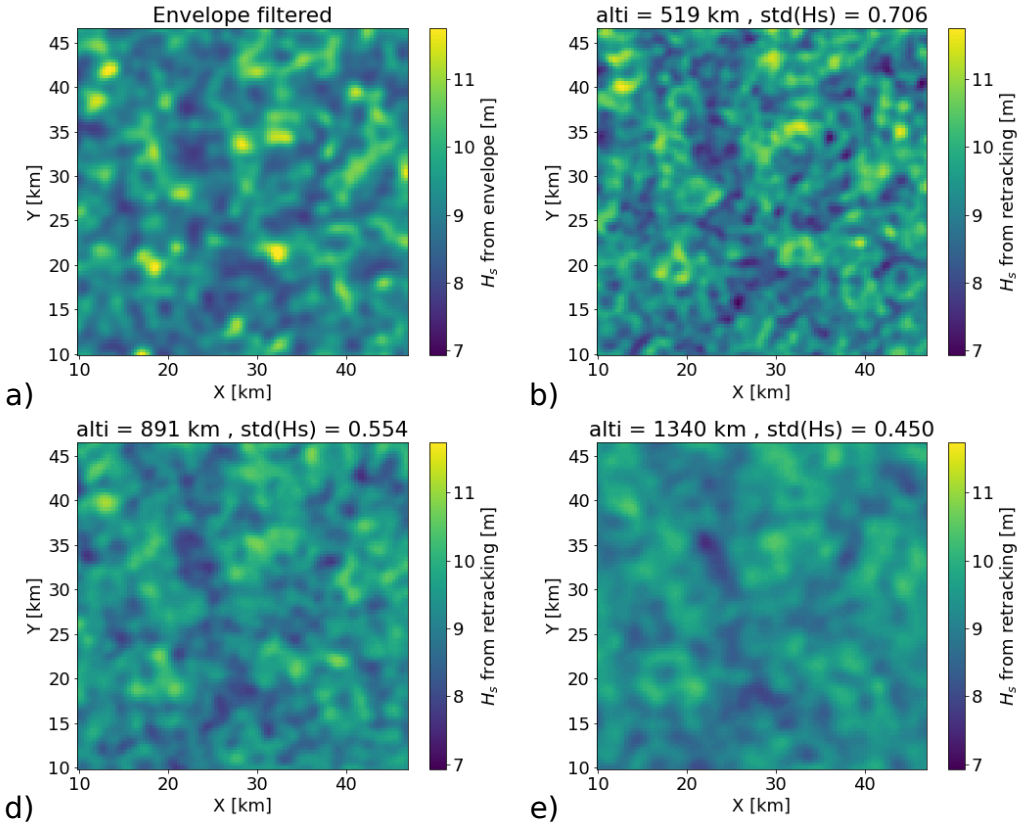

Figure 11. Maps of wave heights obtained a) by smoothing the envelope with Gaussian filter of scale $r_a = 619$ m; or by simulating altimeter waveforms without speckle and using the same least-squares fit (Appendix A), for different altitudes: b) 519 km, c) 891 km, d) 1,340 km, with corresponding r_a of 619 m, 790 m and 940 m.

measurement is similarly based on the convolution of a surface elevation distribution with a flat surface response (Ray et al., 2015). Only the flat surface response is different from the Delay-only processing. We thus expect that wave groups will have similar distortion of the waveforms and contributions to estimates of wave heights and sea level. The blurring effect caused by range bunching will now be confined to the direction perpendicular to the track, with maximum effect of a H_s perturbation located off the satellite track (depending on fitting algorithm), possibly also at a distance of the order of $r_C/2$. Because Delay-Doppler altimeters can actually resolve the along-track variability caused by wave groups instead of averaging it, we expect that H_s fluctuations caused by wave groups are much larger in Delay-Doppler altimetry, together with their spurious effect on sea level estimates. This may explain the relative smaller reduction of std(H_s) at large

H_s which is found when Doppler resolution is enhanced to reduce the speckle effect, and a typical value of std(H_s) for Delay-Doppler Sentinel 3A data which that is around 0.7 m for $H_s = 7$ m (Egido et al., 2021), twice the typical value for SWIM data. This will be the topic of further studies.

4.4 Wave groups and satellite measurements uncertainties

Up to now, the uncertainty of satellite measurements has been determined by the triple-collocation method (Abdalla et al., 2011; Dodet et al., 2022), with the practical result that the uncertainty of altimeter data, either denoised or integrated along-track into super-observations, is of the order of 7% of H_s. However, that error contains representation errors (the co-located in situ data does not sample the same space and time frame), and cannot be extrapolated beyond the range of the co-located dataset, typically wave heights below 8 m. So what can we say about the largest measured wave heights of 20.1 m (Hanafin et al., 2012)? Can we use the measured variability of H_s, for example the 5 Hz or 20 Hz data that is used to make a 1 Hz average, to refine our estimate of the uncertainty of this average? In the present paper we have shown that wave groups are responsible for random fluctuations in H_s estimates, that are generally proportional to H_s but with an effect that depends on the bandwidth of the spectrum, which is generally narrower for larger wave periods. As a result the variability associated to wave groups can be the dominant source of fluctuations in H_s measurements for severe storm conditions. Even though the measurement fluctuations are weakly correlated to the actual wave height variations (as demonstrated in Fig. 3) their magnitudes are strongly correlated. Hence the measured fluctuation std(H_s) contains both uncorrelated speckle noise effect, that can be expected to be reduced by $1/\sqrt{N}$ when averaged from N Hz to 1 Hz, and a true geophysical spatial variability associated to wave groups (and variable fetch, currents, etc.) that will partially average out. We expect that an uncertainty model for averages of H_s measurements may take into account wave groups explicitly. In the case of SWIM, directional wave spectra can be used to separate the actual variability of the 5 Hz data into wave group effects and noise plus other geophysical effects. For other altimeters, one may use empirical correlations between spectral bandwidth, wave height and wind speed. For this information to be useful for a theoretically-based uncertainty estimate, which is much needed for wave heights above 8 m, one may extend the param-

eterization of speckle effects proposed in Appendix A.3, to the actual target waveform and cost function used in the retracking algorithm.

4.5 Considerations on the satellite resolution

The present work should be useful for the exploration of the resolution limits of satellite altimeters and other remote sensing systems that use radar or optical imagery (Kudryavtsev et al., 2017). As processing methods are refined to produce higher resolution near the coast (Passaro et al., 2021) and the ice edge (Collard, 2022), some of the high resolution data will be dominated by wave groups. The associated variance of H_s may provide some constraint on the shape of the directional wave spectrum, but the detailed fluctuations are probably of little value for most applications as groups will travel at speeds of the order of 10 m/s and persist for only a few minutes. The contribution of wave groups to the variability of wave heights measured by altimeters is thus a real effect that contains part of the true variability of wave heights at the scale of the altimeter footprint. Methods developed to remove noise in the data, such as the data-driven Empirical Mode Decomposition (EMD) used by (Quilfen & Chapron, 2019) appear to remove the effect of wave groups. An investigation of the variabilty of wave heights at the smallest scales cannot be based on denoised data alone, because they miss a large part of the true variability.

In locations where H_s varies sharply such as over coral reefs, mud banks or across the sea ice edge, the high resolution wave heights will contain other effects, and these are particularly interesting. Some caution should be used when interpreting these sharp gradients. As we have found out, the maximum wave height will generally be displaced from the location of its true maximum. This displacement is smallest for the SWIM instrument, thanks to the low orbit of CFOSAT, which makes it a particularly interesting instrument for studying small scale wave height variations, in spite of its rather low rate for the nadir beam (5 Hz instead of 20 Hz for Jason), and the absence of Doppler processing.

5 Conclusion

In this paper, we took advantage of the low orbit altitude of CFOSAT, and the low noise level of the nadir beam of the SWIM instrument to study the along-track variabil-

ity of wave height. The directional wave spectra measured by off-nadir beams on SWIM has been complementary to study the relationship between wave spectra and along-track H_s variability. After giving a theoretical estimate of the standard deviation of H_s associated to wave groups as a function of the wave spectrum and satellite altitude, we computed this estimate for 2 years of CFOSAT data using IWWOC-L2S products. We found that the standard deviation of H_s associated to wave groups is generally about half of the standard deviation of H_s measured over a 80 km distance, explaining 25% of measured H_s variance. This ratio of variances increases for storms and in the presence of long swells, it was found to be larger than 75% in 3% of the cases.

The residual variability after substracting the estimated effect of wave groups from the measured Hs variance correlates positively with along-track variance of filtered signals, which brings out regions of strong currents. Studying these features is of major interest and requires some filtering out of the smaller scales. In turn, these smaller scales can be of interest, at least from a statistical point of view, as they are related to wave groups and the generation of infragravity waves and extreme sea level at the coast.

The main novelty of the present work was to represent the non-Gaussian sea level statistics caused by wave groups at the scale of a satellite altimeter footprint. To our knowledge that effect had never been considered, in spite of its strong effect on the radar waveforms (see Fig. A1) much larger than the typical effect of wave nonlinearly introduced by Rodriguez (1988). We have shown that the wave group effect averages out to zero over large scales when waveforms are fitted with a simple least square cost function, but that is not necessarily the case for the more sophisticated methods that are often used. We expect that further work will expand on our approach to consider spurious effects on sea level estimates as well as applications to recent delay-Doppler altimeters.

Appendix A Non-homogeneous H_s and waveform retracking

In this analysis we keep the most simple model of altimeter measurement that is also used in section 2: we neglect antenna pattern, thermal noise and and mispointing effects, and neglect the Earth sphericity. These assumptions are meant to simplify the algebra as much as possible while keeping the essential features of non-homogeneity in wave heights. Likewise we have used the most simple cost function when fitting the waveform, while maximum likelihood methods are generally used with real data (Rodriguez, 1988; Halimi, 2013). We also start by ignoring speckle noise. The analysis performed below is easily extended to consider the third parameter which is usually estimated in retracking wave forms, that is the Normalized Radar Cross Section.

A1 Wave groups and H_s estimate

We consider a small perturbation Δ_H of H_s over an area A, localized around a range $h+R_0$. The original normalized Brown waveform of eq. (7) corresponds to the histogram of the ocean area per unit range, divided by $2\pi h$ so that it varies between 0 and 1, with h the satellite altitude. The perturbation to the waveform is equivalent to removing the original Gaussian distribution of surface elevation with $\sigma_H = H_s/4$ over the area A, and replacing it by a new Gaussian with $\sigma' = (H_s+\Delta_H)/4$, over the same area A, and divide by the normalization factor $2\pi h$. We define the parameter $a = A\Delta_H/(8\pi h)$, which should be small compared to H_s^2. For a small change in H_s, this change in waveform is proportional to the derivative of the Gaussian distribution with respect to σ_H and we find that the waveform is now

$$w(R) = w_B(R,\sigma_H) + a\frac{\mathrm{e}^{-(R-h-R_0)^2/(2\sigma_H^2)}}{\sqrt{2\pi}}\frac{(R-h-R_0)^2-\sigma_H^2}{\sigma_H^4} + O(a^2) \qquad \text{(A1)}$$

We note that a smaller change Δ_H over a larger area A changes the waveform in the same way as a larger change over a smaller area, provided that a is the same. For simplicity we redefine the Chelton footprint diameter as $r'_C = \sqrt{2H_s h}$, and we find that taking an area of radius $\alpha r'_C$ gives $a = \alpha^2\Delta_H H_s/4$.

The shape of these distorted waveforms is illustrated in Fig. A1. With the exaggerated distortion shown here, fitting a Brown waveform would give a wave height of $H_{s,\mathrm{fit}} =$ 12.6 m for $R_0 = 2.5$ m and $H_{s,\mathrm{fit}} = 10$ m for $R_0 = 0$, which is a strange way to average the $H_s = 13$ m over part of the footprint and 10 m in the rest of the footprint.

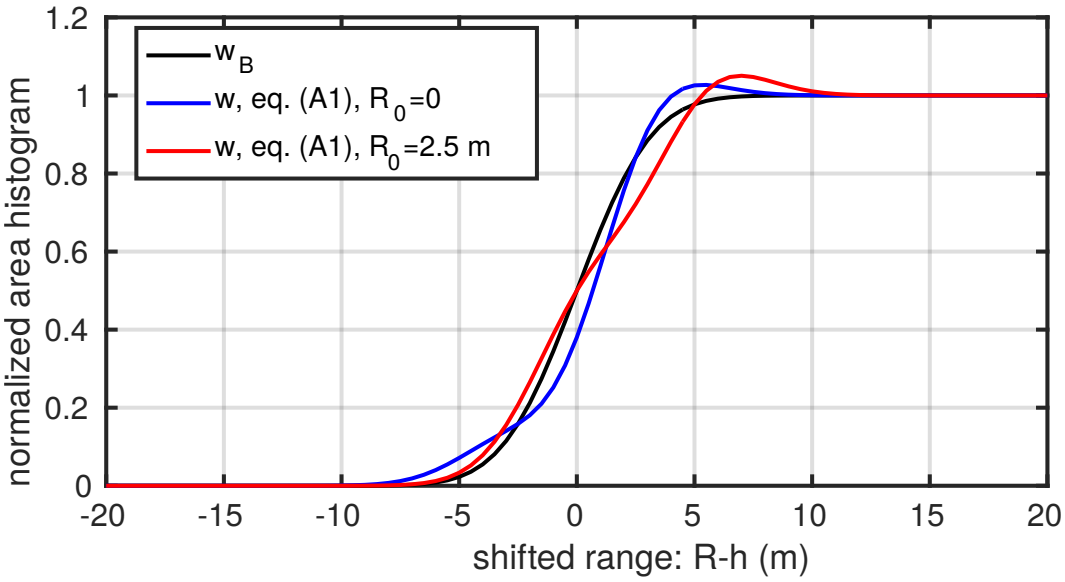

Figure A1. Example waveforms in the presence of a localized change in H_s around the range $h + R_0$, for $H_s = 10$ m. In order to be visible, the perturbation was exaggerated taking $a = 1.875$ m^2, that would correspond to Δ_H=3 m over an area of radius $r'_C/4$, a perturbation that is neither small nor localized.

For smaller values of the perturbation a, the deviation in the fitted H_s can be computed analytically.

For simplicity we will assume that the waveforms are defined for $-\infty < R < \infty$, and the sum of the difference squared between $w(R)$ and $w_B(R, \sigma'_H)$, when integrated from $R = -\infty$ to $R = -\infty$ is the following cost function,

$$\begin{aligned} C &= \int_{-\infty}^{\infty} \{[w_B(R,\sigma_H) - w_B(R,\sigma'_H)] + [w(R) - w_B(R,\sigma_H)]\}^2 \, \mathrm{d}R \\ &\simeq \int_{-\infty}^{\infty} \left\{ (\sigma_H - \sigma'_H) \frac{\partial w_B(R,\sigma_H)}{\partial \sigma_H} + [w(R) - w_B(R,\sigma)] \right\}^2 \mathrm{d}R \\ &= (\sigma'_H - \sigma_H)^2 \frac{1}{4\sqrt{\pi}\sigma_H} + (\sigma'_H - \sigma_H) \frac{aR_0}{8\sqrt{\pi}\sigma_H^5} \mathrm{e}^{-R_0^2/(4\sigma_H^2)} (R_0^2 - 6\sigma_H^2) + \frac{3a^2}{8\sqrt{\pi}\sigma_H^3}. \end{aligned}$$

Fitting σ'_H corresponds to solving $\partial C / \partial(\sigma'_H - \sigma_H) = 0$. We note that that error terms that are either not a function of $(\sigma'_H - \sigma_H)$ or odd functions of R have no impact on the fitted value. For example the a^2 term in eq. (A1) does not contribute any difference to the fit.

We find that the fitted value differs from the background value H_s by a factor proportional to a and function of R_0/H_s ,

$$H_{s,\mathrm{fit}} = H_s + \frac{A}{\pi h}\frac{\Delta_H}{H_s}\underbrace{\left[2\frac{R_0}{H_s}\left(6-\left(\frac{4R_0}{H_s}\right)^2\right)\mathrm{e}^{-4R_0^2/H_s^2}\right]}_{J(R_0/H_s)}, \tag{A2}$$

with the function J in brackets having a maximum close to 2 for $R_0 \simeq H_s/4$, as shown in Fig. A2.

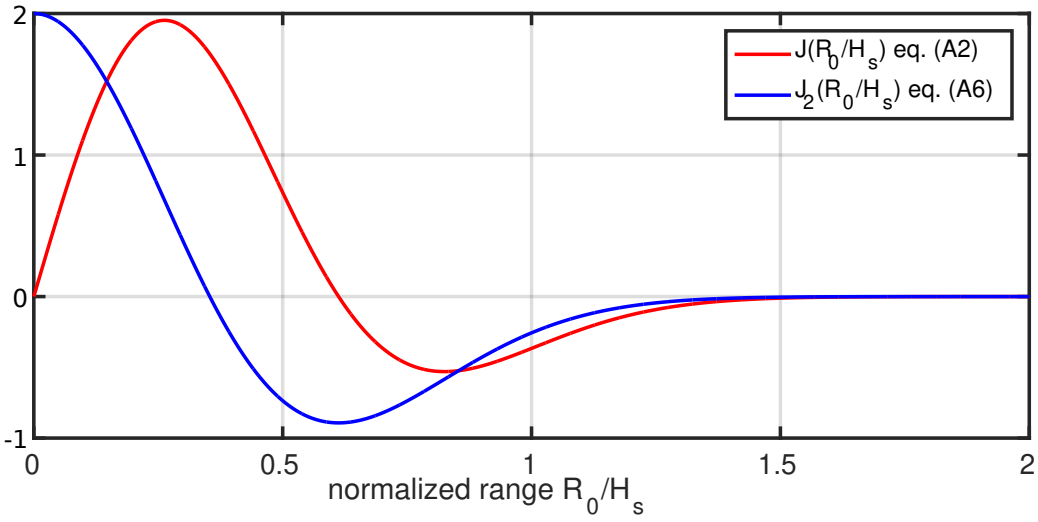

Figure A2. Functions $J(R_0/H_s)$ and $J_2(R_0/H_s)$ corresponding to the term in square brackets in eqs. (A2) and (A8). The maximum of J is at $R_0/H_s = 0.5\sqrt{0.5(3-\sqrt{6})} \simeq 0.26$, where J takes a value close to 1.96. This location corresponds to a distance from nadir approximately $\sqrt{0.26}r'_C \simeq r'_C/2$.

We note that this perturbation is zero for $R_0 = 0$, meaning that a localized change at the center of the footprintdoes not modify the estimated H_s. This lack of impact on $H_{s,\mathrm{fit}}$ comes from the fact that the perturbation of the waveform (the second term in eq. A1) is an odd function of range and thus orthogonal to the even functions that are the Brown waveforms with zero epoch $w_B(R, \sigma_H)$. The maximum perturbation of $H_{s,\mathrm{fit}}$ occurs for H_s perturbations at a range R_0 close to σ_H, i.e. corresponding to a distance from nadir of $r'_C/4$. Eq. (A2) gives results that are fairly robust for finite values of a/H_s^2, and would predict a wave height of 12.9 m in the case $R_0 = 2.5$ m shown in Fig. A1.

We now consider the average effect of the perturbation by computing the average over R_0, taking all values of R_0 from 0 to nH_s, which corresponds to averaging over an

area $B = \pi n {r'_C}^2 = 2n\pi H_s h$. The integral of the function in brackets is

$$I = \int_0^\infty 2\frac{R_0}{H_s}\left(6 - 16\frac{R_0^2}{H_s^2}\right) \mathrm{e}^{-4R_0^2/H_s^2} \mathrm{d}R_0 = 0.5 H_s. \tag{A3}$$

As a result, the average effect of a Δ_H change over an area $A = \pi\alpha^2 {r'_C}^2 = 2\pi\alpha^2 h H_s$ is, when n is large,

$$\delta_{H,\mathrm{alti}} = \frac{1}{nH_s}\int_0^{nH_s} (H_{s,\mathrm{fit}} - H_s)\,\mathrm{d}R_0 = \frac{1}{2n}\frac{A}{\pi h}\frac{\Delta_H}{H_s} = \frac{\alpha^2}{n}\Delta_H. \tag{A4}$$

This average effect of the localized perturbation of H_s is the same as a true area average, which is the perturbation times the ratio of the areas A and B, namely $\delta_H = \Delta_H A/B$. In other words, the perturbation is amplified if located at $0.15 < r/r'_C < 0.34$ from nadir, by a factor J that is up to 2. Otherwise the perturbation is attenuated, so that on average it is equal to the true perturbation. This averaging property and the unbiased estimate of $H_{s,\mathrm{fit}}$, with a perturbation that changes sign when Δ_H changes sign, are specific to the simple least squares used here. For example, fitting the logarithm of the waveform produces a biased estimator and a non-zero response for $R_0 = 0$. Hence the results presented here are specific to the fitting method.

In practice, distributed anomalies of H_s are not only a function of the distance from nadir, so that a local estimate of H_s will combine positive and negative anomalies Δ_H that are located at the same distance from nadir, and will partially cancel. This explain that our best fit for r_0 is $r_C/4.5$, smaller than the $r_C/2$ which is a more typical scale of the footprint. Instead of retracking the simulated altimeter data, we can reproduce the H_s variability by first summing the Δ_H anomalies for a given r, compute the $H_{s,\mathrm{fit}}$ anomaly for that r using eq. (A2) and then sum those anomalies for all r, as demonstrated in Fig. A3. This procedure is equivalent to a spatial filter $\mathcal{J}(r)$ that is built from the J function, converting the range $h + R_0$ to a horizontal distance from nadir $r = \sqrt{2hR_0}$,

$$\mathcal{J}(r) = G_{r_C}(r) + J \otimes (Id - G_{r_C})(r) \tag{A5}$$

where, G_{r_C} is a Gaussian filter with width r_C, and Id is the identity function. The estimated H_s thus comes from

$$H_s(x) = 4\sqrt{\frac{2}{\pi}} \cdot (\mathcal{J} \otimes \eta)(x) \tag{A6}$$

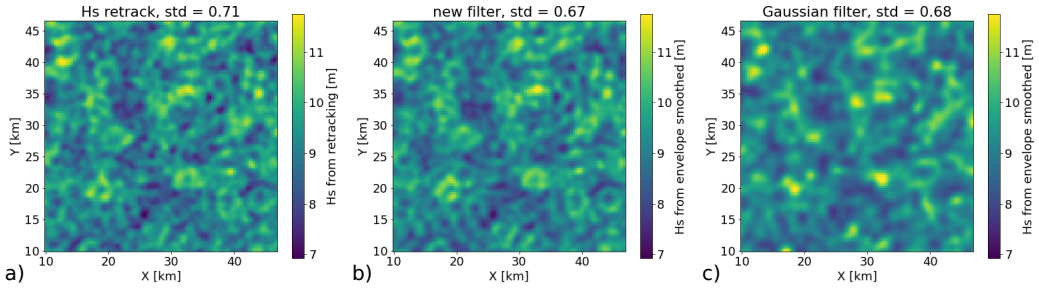

Figure A3. Equivalent to Fig. 3: (a) H_s surface obtained from retracking and H_s surfaces obtained from convoluting the envelope with (b) a spatial filter built from the J function, (c) a gaussian filter with $r_a = r_C/4.5$.

A2 Wave groups and sea level estimate

While perturbations at nadir do not change the H_s estimate, they would change the mean sea level z_e (the epoch is $-z_e$) when using a 2-parameter waveform

$$w_{B2}(R, \sigma_H, z_e) = \frac{1}{2}\left[1 + \mathrm{erf}\left(\frac{(R + z_e) - h}{\sqrt{2}\sigma_H}\right)\right]. \tag{A7}$$

In the case shown in Fig. A1 with $R_0 = 0$ the estimated mean sea level is $z = -37$ cm. We thus expect wave groups to contribute to fluctuations in the estimated sea level at the scale of groups. The estimation of that effect follows the same method used above. Fitting $w_{B2}(R, \sigma'_H, z_e)$ to our waveform $w(R)$ given by eq. (A1) is obtained by minimizing a modified cost function, that is the same as C but with one extra term $z_e \partial w_{B2}/\partial z_e$ inside the curly brackets, giving two extra non-zero terms proportional to z_e^2 and z_e. We note that the cross-term proportional to $z_e(\sigma'_H - \sigma_H)$ is an odd function of R and thus integrates to zero. After integration over R we get the cost function,

$$C_2 = C + \frac{z_e^2}{2\sqrt{\pi}\sigma_H} + \frac{a z_e}{4\sqrt{\pi}\sigma_H^2} \mathrm{e}^{-R_0^2/(4\sigma_H^2)} \left(\frac{R^2}{\sigma_H^2} - 2\right).$$

Taking the derivative of C_2 with respect to z_e gives

$$z_e = -\frac{A\Delta_H}{2\pi h H_s} \underbrace{\left[\left(2 - 16\frac{R_0^2}{H_s^2}\right) \mathrm{e}^{-4R_0^2/H_s^2}\right]}_{J_2(R_0/H_s)}. \tag{A8}$$

The function J_2 is plotted in Fig. A2. Hence z_e has the strongest deviation when the wave height perturbation is centered at nadir, and the sign of the deviation is opposite to Δ_H: i.e. a wave group centered at the nadir would give a spurious lower sea level. On average the z_e deviation has a zero mean when R_0 is varied. As a result of the different shapes of J and J_2, there is no simple correlation of the H_s and z_e perturbations,

contrary to the correlations induced by speckle noise in the waveform measurement (Sandwell & Smith, 2005).

There is some correlation for R_0/H_s between 0.7 and 1.2 which may contribute to anti-correlation of sea level anomalies and wave heights at scales around r_C, and thus may persist in 1 Hz data. We insist that these are spurious sea level variations. In deep water these spurious oscillations are much larger than the fraction of a millimeter associated to true sea level variations with bound infragravity elevation that is anti-correlated with the envelope of kilometer-scale wave groups (Ardhuin et al., 2004). The spurious sea level oscillations described are also probably generally larger in amplitude than the larger scale (20-km wavelength) true sea level variations associated to free infragravity waves that have no phase correlation with the local envelope (Ardhuin et al., 2014). In shallow water, the real sea level fluctuations can be more important.

A3 Speckle noise

Random fluctuations in the electromagnetic power measured by the radar combine an additive thermal noise that can often be neglected and a multiplicative noise that is caused by the Rayleigh fading of the interfering reflections off a random sea surface (Quartly et al., 2001). In fact speckle is to the radar power what wave groups are to the wave energy. A good model for the speckle is a multiplicative random noise, so that the measured waveform for each range is multiplied by a factor $(1+\varepsilon(R))$ with $\varepsilon(R)$ following a χ^2 distribution with $N(R)$ degrees of freedom depending on the number of pulses averaged and the pulse repetition frequency (Quartly et al., 2001).

For the retracking, the effect of this speckle perturbation is one additional term $\varepsilon(R)w(R)$ inside the curly brackets of the cost function. Expanding the square and expressing the integral, it gives two terms, one proportional to $(\sigma'_H - \sigma_H)$ that is relevant to the H_s estimate and the other proportional to z_e fit, so that the cost function is now,

$$C_3 \simeq C_2 - 2(\sigma'_H - \sigma_H)\int_{-\infty}^{\infty}\varepsilon(R)w(R)\frac{\partial w_{B2}}{\partial \sigma_H}\mathrm{d}R - 2z_e\int_{-\infty}^{\infty}\varepsilon(R)w(R)\frac{\partial w_{B2}}{\partial z_e}\mathrm{d}R, \qquad \text{(A9)}$$

with

$$\frac{\partial w_{B2}}{\partial \sigma_H} = -\frac{R-h+z_e}{\sigma_H^2\sqrt{2\pi}}\mathrm{e}^{-(R-h+z_e)^2/(2\sigma_H^2)}, \qquad \text{(A10)}$$

and

$$\frac{\partial w_{B2}}{\partial z_e} = \frac{1}{\sigma_H\sqrt{2\pi}}\mathrm{e}^{-(R-h+z_e)^2/(2\sigma_H^2)}. \qquad \text{(A11)}$$

The estimated wave height that gives $\partial C_3/\partial(\sigma'_H - \sigma_H) = 0$ thus has an extra term induced by speckle noise,

$$H_{s,\mathrm{fit}} = H_s + \frac{A}{\pi h}\frac{\Delta_H}{H_s} J(R_0/H_s) + 16\sqrt{2}H_s \int_{-\infty}^{\infty} \varepsilon(u)\left(1+\mathrm{erf}(2\sqrt{2}u)\right) u\mathrm{e}^{-8u^2}\mathrm{d}u, \quad \text{(A12)}$$

with $u = (R - h + z_e)/H_s$. The speckle-induced perturbation of $H_{s,\mathrm{fit}}$ is a weighted sum of random fluctuations with zero mean. In practice we can consider $\varepsilon(R)$ to be Gaussian, and the variance of the speckle perturbation is the sum of the variances associated to each range R times the weight squared. To get some useful order of magnitude we may take the variance of $\varepsilon(R)$, which is $1/N(R)$, to be constant at $1/N$. For large values of H_s, the discretized waveform is well approximated by the continuous form and the part of the variance of $H_{s,\mathrm{fit}}$ induced by the speckle is approximately 5.0 H_s/N, with a standard deviation $2.24\sqrt{H_s/N}$. Using the value $N = 512$ for the number of pulses of the SWIM nadir beam that we may assume to be independent, and $H_s = 2$ m, this gives a standard deviation of 0.14 m, broadly consistent with the background level in Fig. 8.c. However, we note that the magnitude of the variability of $H_{s,\mathrm{fit}}$ will depend on the method used to fit the waveform. In the case of the SWIM data, the adaptive method that is used is based on a maximum likelihood (Tourain et al., 2021). It is probably more robust to speckle noise perturbations than the least square estimate used here, in particular for this instrument that has a relatively high signal to noise ratio.

Acknowledgments

All CFOSAT data are provided by courtesy of CNSA and CNES. This research was made possible by support from ESA as part of the Sea State CCI project. MDC is currently supported by a postdoctoral grant from the Centre National d'Études Spatiales (CNES). MDC would like to thank JF Piolle from Ifremer for the data management support.

Open Research

The L2 and L2P SWIM data sets used here corresponds to the files reprocessed in version 5.1.2 and made available by CNES on the ftp server of AVISO+ (ftp-access.aviso.altimetry.fr, directories cfosat/swim_l2_op05 and cfosat/swim_l2p_box_nrt/), accessible to anyone after registration.

The L2S SWIM data set was obtained from Ifremer at https://data-cersat.ifremer.fr/projects/iwwoc/swi_l2s

The denoised CFOSAT data used for Fig. 9 is available at https://doi.org/10.24400/527896/a01-2022.013

References

Abdalla, S., & Cavaleri, L. (2002). Effect of wind variability and variable air density on wave modelling. *J. Geophys. Res.*, *107*(C7), 17.

Abdalla, S., Janssen, P., & Bidlot, J.-R. (2011). Altimeter near real time wind and wave products: Random error estimation. *Marine Geodesy*, *34*, 396–406. doi: 10.1080/01490419.2011.585113

Alday, M., Accensi, M., Ardhuin, F., & Dodet, G. (2021). A global wave parameter database for geophysical applications. part 3: Improved forcing and spectral resolution. *Ocean Modelling*, *166*, 101848. doi: 10.1016/j.ocemod.2021.101848

Altiparmaki, O., Kleinherenbrink, M., Naeije, M., Slobbe, C., & Visser, P. (2022). Sar altimetry data as a new source for swell monitoring. *Geophys. Res. Lett.*. doi: 10.1029/2021GL096224

Ardhuin, F., Chapron, B., & Elfouhaily, T. (2004). Waves and the air-sea momentum budget, implications for ocean circulation modelling. *J. Phys. Oceanogr.*, *34*, 1741–1755. doi: 10.1175/1520-0485%282004%29034%3C1741%3AWATAMB%3E2.0.CO%3B2

Ardhuin, F., Rascle, N., Chapron, B., Gula, J., Molemaker, J., Gille, S. T., ... Rocha, C. (2017). Small scale currents have large effects on wind wave heights. *J. Geophys. Res.*, *122*(C6), 4500–4517. doi: 10.1002/2016JC012413

Ardhuin, F., Rawat, A., & Aucan, J. (2014). A numerical model for free infragravity waves: Definition and validation at regional and global scales. *Ocean Modelling*, *77*, 20–32. doi: 10.1016/j.ocemod.2014.02.006

Ardhuin, F., Stopa, J. E., Chapron, B., Collard, F., Husson, R., Jensen, R. E., ... Young, I. (2019). Observing sea states. *Frontiers in Marine Sci.*, *6*, 124. doi: 10.3389/fmars.2019.00124

Arhan, M., & Ezraty, R. (1978). Statistical relations between successive wave heights. *Oceanol. Acta*, *1*, 151–158.

Badulin, S. I. (2014). A physical model of sea wave period from altimeter data. *J. Geophys. Res.*, *119*, 856–869. doi: 10.1002/2013JC009336

Brown, G. S. (1977). The average impulse response of a rough surface and its appli-

cations. *IEEE J. Oceanic Eng.*, *2*(1), 67–63. doi: 10.1109/JOE.1977.1145328

Chelton, D. B., Walsh, E. J., & MacArthur, J. L. (1989). Pulse compression and sea level tracking in satellite altimetry. *J. Atmos. Ocean Technol.*, *6*, 407–438. doi: 10.1175/1520-0426(1989)006⟨0407:pcaslt⟩2.0.co;2

Chen, G., Chapron, B., Ezraty, R., & Vandemark, D. (2002). A global view of swell and wind sea climate in the ocean by satellite altimeter and scatterometer. *J. Atmos. Ocean Technol.*, *19*, 1849–1859.

Collard, L. a. F. a. M. a. E. F. a. F., Fabrice and Marié. (2022). Wind-wave attenuation in arctic sea ice: A discussion of remote sensing capabilities. *J. Geophys. Res.*, *127*, e2022JC018654. doi: 10.1029/2022JC018654

Dodet, G., Abdalla, S., Alday, M., Accensi, M., Bidlot, J., & Ardhuin, F. (2022). Error characterization of significant wave heights in multidecadal satellite altimeter product, model hindcast, and in situ measurements using the triple collocation technique. *J. Atmos. Ocean Technol.*, *39*, 887–901. doi: 10.1175/JTECH-D-21-0179.1

Dodet, G., Piolle, J.-F., Quilfen, Y., Abdalla, S., Accensi, M., Ardhuin, F., ... Donlon, C. (2020). The sea state cci dataset v1: towards a sea state climate data record based on satellite observations. *Earth System Sci. Data*, *12*, 1929–1951. doi: 10.5194/essd-12-1929-2020

Egido, A., Dinardo, S., & Ray, C. (2021). The case for increasing the posting rate in delay/Doppler altimeters. *Adv. Space Res.*, *68*, 930–936. doi: 10.1016/j.asr.2020.03.014

Halimi, A. (2013). *From conventional to delay/doppler altimetry* (Doctoral dissertation, INP Toulouse, Toulouse, France). Retrieved from `https://theses.hal.science/tel-00951973`

Hanafin, J., Quilfen, Y., Ardhuin, F., Sienkiewicz, J., Queffeulou, P., Obrebski, M., ... Stutzmann, E. (2012). Phenomenal sea states and swell radiation: a comprehensive analysis of the 12-16 February 2011 North Atlantic storms. *Bull. Amer. Meterol. Soc.*, *93*, 1825–1832. doi: 10.1175/BAMS-D-11-00128.1

Hasselmann, K., Barnett, T. P., Bouws, E., Carlson, H., Cartwright, D. E., Enke, K., ... Walden, H. (1973). Measurements of wind-wave growth and swell decay during the Joint North Sea Wave Project. *Deut. Hydrogr. Z.*, *8*(12), 1–95. (Suppl. A)

Hauser, D., Tison, C., Amiot, T., Delaye, L., Corcoral, N., & Castillan, P. (2017). SWIM: The first spaceborne wave scatterometer. *IEEE Trans. on Geosci. and Remote Sensing*, *55*(5), 3000–3014.

Hauser, D., Tourain, C., Hermozo, L., Alraddawi, D., Aouf, L., Chapron, B., ... Tran, N. (2021). New observations from the SWIM radar on-board CFOSAT: Instrument validation and ocean wave measurement assessment. *IEEE Trans. on Geosci. and Remote Sensing*, *59*(1), 5–26. doi: 10.1109/tgrs.2020.2994372

Jackson, F. C., Walton, W. T., & Peng, C. Y. (1985). A comparison of in situ and airborne radar observations of ocean wave directionality. *J. Geophys. Res.*, *90*(C1), 1005–1018.

Kudryavtsev, V., Yurovskaya, M., Chapron, B., Collard, F., & Donlon, C. (2017). Sun glitter imagery of surface waves. part 1: Directional spectrum retrieval and validation. *J. Geophys. Res.*, *122*. doi: 10.1002/2016JC012425

Lavrenov, I. V. (2001). Effect of wind wave parameter fluctuation on the nonlinear spectrum evolution. *J. Phys. Oceanogr.*, *31*, 861–873. Retrieved from `http://ams.allenpress.com/archive/1520-0485/31/4/pdf/i1520-0485-31-4-861`

Le Merle, E., Hauser, D., Peureux, C., Aouf, L., Schippers, P., Dufour, C., & Dalphinet, A. (2021). Directional and frequency spread of surface ocean waves from swim measurements. *J. Geophys. Res.*, *126*(7), e2021JC017220. doi: 10.1029/2021JC017220

Longuet-Higgins, M. S. (1984). New integral relations for gravity waves of finite amplitude. *J. Fluid Mech.*, *149*, 205–215. (see also Yu and Wu, J. Fluid Mech., 1987)

Masson, D., & Chandler, P. (1993). Wave groups: a closer look at spectral methods. *Coastal Eng.*, *20*, 249–275.

Passaro, M., Cipollini, P., Vignudelli, S., Quartly, G. D., & Snaith, H. M. (2014). ALES: A multi-mission adaptive subwaveform retracker for coastal and open ocean altimetry. *Remote sensing of Environment*, *145*, 173–189.

Passaro, M., Hemer, M. A., Quartly, G. D., Schwatke, C., Dettmering, D., & Seitz, F. (2021). Global coastal attenuation of wind-waves observed with radar altimetry. *Nature communications*, *12*, 3812. doi: 10.1038/s41467-021-23982-4

Peral, E., Rodriguez, E., & Esteban-Fernandez, D. (2015). Impact of surface waves on SWOT's projected ocean accuracy. *Remote Sensing*, *7*(11), 14509–14529.

889 doi: 10.3390/rs71114509

890 Quartly, G. D., Smith, W. H. F., , & Passaro, M. (2019). Removing intra-1-Hz co-
891 variant error to improve altimetric profiles of σ_0 and sea surface height. *IEEE*
892 *Trans. on Geosci. and Remote Sensing*, *57*(6), 3741–3752. doi: 10.1109/TGRS
893 .2018.2886998

894 Quartly, G. D., Srokosz, M. A., & McMillan, A. C. (2001). Analyzing altimeter arti-
895 facts: Statistical properties of ocean waveforms. *J. Atmos. Ocean Technol.*, *18*,
896 2074–2091. doi: 10.1175/1520-0426(2001)018⟨2074:AAASPO⟩2.0.CO;2

897 Quilfen, Y., & Chapron, B. (2019). Ocean surface wave-current signatures from
898 satellite altimeter measurements. *Geophys. Res. Lett.*, *216*, 253-261. doi: 10
899 .1029/2018GL081029

900 Ray, C., Martin-Puig, C., Clarizia, M. P., Ruffini, G., Dinardo, S., Gommengin-
901 ger, C., & Benveniste, J. (2015). SAR altimeter backscattered waveform
902 model. *IEEE Trans. on Geosci. and Remote Sensing*, *53*, 911–919. doi:
903 10.1109/TGRS.2014.2330423

904 Rice, S. (1944). Mathematical analysis of random noise. In N. Wax (Ed.), *Noise and*
905 *stochastic processes* (pp. 133–294). New York: Dover Publications Inc. (pub-
906 lished 1954).

907 Rodriguez, E. (1988). Altimetry for non-gaussian oceans: Height biases and es-
908 timation of parameters. *J. Geophys. Res.*, *93*, 14107–14120. doi: 10.1029/
909 JC093iC11p14107

910 Sandwell, D. T., & Smith, W. H. F. (2005). Retracking ers-1 altimeter waveforms
911 for optimal gravity field recovery. *Geophys. J. Int.*, *163*, 79–89. doi: 10.1111/
912 j.1365-246X.2005.02724.x

913 Saulnier, J.-B., Clément, A., de O. Falcão, A. F., Pontes, T., Prevosto, M., & Ricci,
914 P. (2011). Wave groupiness and spectral bandwidth as relevant parameters
915 for the performance assessment of wave energy converters. *Ocean Eng.*, *38*(1),
916 130-147.

917 Tayfun, A., & Lo, J.-M. (1989). Wave envelope and related spectra. *J. of Waterway,*
918 *Port Coast. Ocean Eng.*, *115*, 515–533. doi: 10.1061/(ASCE)0733-950X(1989)
919 115:4(515)

920 Toba, Y. (1973). Local balance in the air-sea boundary processes. III on the spec-
921 trum of wind waves. *J. Oceanogr. Soc. Japan*, *29*, 209–220. Retrieved from

http://www.terrapub.co.jp/journals/JO/JOSJ/pdf/2905/29050209.pdf

Tourain, C., Piras, F., Ollivier, A., Hauser, D., Poisson, J. C., Boy, F., ... Tison, C. (2021). Benefits of the adaptive algorithm for retracking altimeter nadir echoes: Results from simulations and CFOSAT/SWIM observations. *IEEE Trans. on Geosci. and Remote Sensing*, *59*, 9927–9940. doi: 10.1109/TGRS.2021.3064236

Tournadre, J. (1993). Time and space scales of significant wave heights. *J. Geophys. Res.*, *98*(C3), 4727–4738.

Villas Bôas, A. B., Lenain, L., Cornuelle, B. D., Gille, S. T., & Mazloff, M. R. (2022). A broadband view of the sea surface height wavenumber spectrum. *Geophys. Res. Lett.*, *49*(e2021GL096699). doi: 10.1029/2021GL096699

Young, I. R., Zieger, S., & Babanin, A. V. (2011). Global trends in wind speed and wave height. *Science*, *332*, 451–455. doi: 10.1126/science.1197219